Spectral Functions of the Holstein Polaron: Exact and Approximate Solutions

Petar Mitrić, Veljko Janković, Nenad Vukmirović, and Darko Tanasković

Institute of Physics Belgrade, University of Belgrade, Pregrevica 118, 11080 Belgrade, Serbia

It is generally accepted that the dynamical mean field theory gives a good solution of the Holstein model, but only in dimensions greater than two. Here, we show that this theory, which becomes exact in the weak coupling and in the atomic limit, provides an excellent, numerically cheap, approximate solution for the spectral function of the Holstein model in the whole range of parameters, even in one dimension. To establish this, we make a detailed comparison with the spectral functions that we obtain using the newly developed momentum-space numerically exact hierarchical equations of motion method, which yields electronic correlation functions directly in real time. We crosscheck these conclusions with our path integral quantum Monte Carlo and exact diagonalization results, as well as with the available numerically exact results from the literature.

The Holstein model is the simplest model that describes an electron that propagates through the crystal and interacts with localized optical phonons [1]. On the example of this model, numerous many-body methods were developed and tested [2]. The Holstein molecular crystal model is also very important in order to understand the role of polarons (quasiparticles formed by an electron dressed by lattice vibrations) in real materials [3]. This is still a very active field of research fueled by new directions in theoretical studies [4–12] and advances in experimental techniques [13].

The Holstein model can be solved analytically only in the limits of weak and strong electron-phonon coupling [14–16]. Reliable numerical results for the ground state energy and quasiparticle effective mass were obtained in the late 1990s using the density matrix renormalization group (DMRG) [17,18] and path integral quantum Monte Carlo (QMC) methods [19], and also within variational approaches [20–22]. At the time, numerically exact spectral functions for one-dimensional (1D) systems were obtained only within the DMRG method [17,18]. The main drawback of the QMC method is that it gives correlation functions in imaginary time and obtaining spectral functions and dynamical response functions is often impossible since the analytical continuation to the real frequency is a numerically ill-defined procedure. Interestingly, at finite temperature the spectral functions were obtained only very recently using finite-T Lanczos (FTLM) [23] and finite-T DMRG [24] methods. All these methods have their strengths and weaknesses depending on the parameter regime and temperature. As usually happens in a strongly interacting many-body problem, a complete physical picture emerges only by taking into account the solutions obtained with different methods.

The hierarchical equations of motion (HEOM) method is a numerically exact technique that has recently gained popularity in the chemical physics community [25–28]. It has been used to explore the dynamics of an electron (or exciton) linearly coupled to a Gaussian bosonic bath. Within HEOM, we calculate the correlation functions directly on the real time (real frequency) axis [29]. Nevertheless, the applications of the HEOM method to the Holstein model [30–34] have been, so far, scarce because of the numerical instabilities stemming from the discreteness of the phonon bath on a finite lattice.

Along with numerically exact methods, a number of approximate techniques have been developed and applied to the Holstein model [35–38]. The dynamical mean field theory (DMFT) is a simple nonperturbative technique that has emerged as a method of choice for the studies of the Mott physics within the Hubbard model [39,40]. It can also be applied to the Holstein model giving numerically cheap results directly on the real frequency axis [41]. This method fully takes into account local quantum fluctuations and it becomes exact in the limit of infinite coordination number when the correlations become completely local. It was soon recognized [42,43] that the DMFT gives qualitatively correct spectral functions and conductivity for the Holstein model in three dimensions. In low-dimensional systems the solution is approximate as it neglects the nonlocal correlations and one might expect that the DMFT solution would not be accurate, particularly in one dimension. Surprisingly, to our knowledge, only the DMFT solution for the Bethe lattice was used in comparisons with the numerically exact results for the ground state properties in one dimension [20,44]. The quantitative agreement was rather poor, suggesting that the DMFT cannot provide a realistic description of the low-dimensional Holstein model due to the importance of nonlocal correlations [16,20,44].

In this Letter, we present a comprehensive solution of the 1D Holstein model: (i) We solve the DMFT equations in all

parameter regimes. At zero temperature we find a remarkable agreement of the DMFT ground state energy and effective mass with the available results from the literature in one, two, and three dimensions. (ii) For intermediate electron-phonon coupling, we obtain numerically exact spectral functions using the recently developed momentum-space HEOM approach [45]. For strong coupling we calculate the spectral functions using exact diagonalization (ED). We find a very good agreement with DMFT results and therefore demonstrate that the DMFT is rather accurate, in sharp contrast to current belief in the literature. (iii) We crosscheck the results with our QMC calculations in imaginary time. Overall, we demonstrate that the DMFT emerges as a unique method that gives close to exact spectral functions in the whole parameter space of the Holstein model, both at zero and at finite temperature.

Model and methods.—We study the 1D Holstein model given by the Hamiltonian

$$H = -t_0 \sum_i (c_i^\dagger c_{i+1} + \text{H.c.})$$
$$- g \sum_i n_i(a_i^\dagger + a_i) + \omega_0 \sum_i a_i^\dagger a_i. \quad (1)$$

Here, $c_i^\dagger$ ($a_i^\dagger$) are the electron (phonon) creation operators, t_0 is the hopping parameter, and $n_i = c_i^\dagger c_i$. We consider dispersionless optical phonons of frequency ω_0, and g denotes the electron-phonon coupling parameter. t_0, $\hbar$, k_B, and lattice constant are set to 1. We consider the dynamics of a single electron in the band. It is common to define several dimensionless parameters: adiabatic parameter $\gamma = \omega_0/2t_0$, electron-phonon coupling $\lambda = g^2/2t_0\omega_0$, and $\alpha = g/\omega_0$. These parameters correspond to different physical regimes of the Holstein model shown schematically in Fig. 1(a).

In order to obtain reliable solutions in the whole parameter space, we use two approximate methods and three methods that are numerically exact. In the Holstein model, the DMFT reduces to solving the polaron impurity problem in the conduction electron band supplemented by the self-consistency condition [41]. The impurity problem can be solved in terms of the continued fraction expansion, giving the local Green's function on the real frequency axis (see Ref. [41] and Supplemental Material (SM) [46], Sec. I, for details). A crucial advantage of the DMFT for the Holstein model is that it becomes exact in both the weak coupling and in the atomic limit, and that it can be easily applied in the whole parameter space both at zero and at finite temperature. The DMFT equations can be solved on a personal computer in just a few seconds to a few minutes depending on the parameters. On general grounds, the DMFT is expected to work particularly well at high temperatures when the correlations become more local due to the thermal fluctuations [47,48]. We will compare the DMFT with the well-known self-consistent Migdal
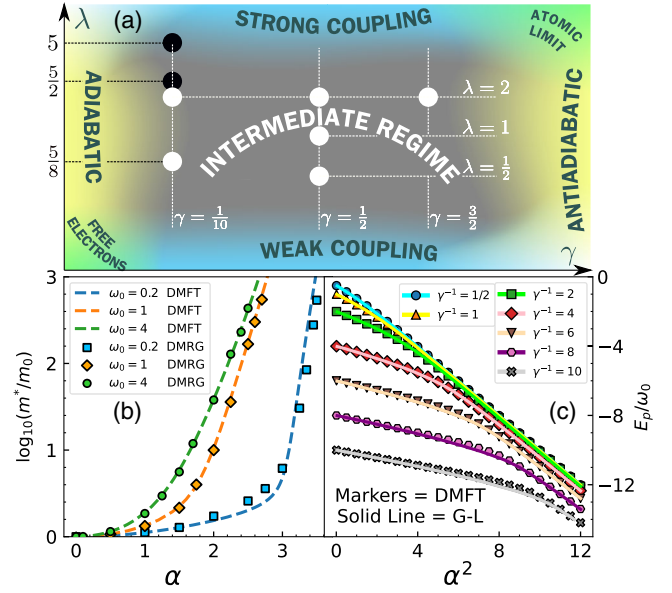

FIG. 1. (a) Schematic plot of different regimes in the (γ, λ) parameter space. The white (black) circles correspond to parameters for which both HEOM and QMC (just QMC) calculations were performed. The DMFT results are obtained in practically whole space of parameters. (b) Comparison of the DMFT and DMRG (taken from Refs. [17,20]) renormalized electron mass at $T = 0$. (c) Comparison of the ground state energy from the DMFT and the global-local variational approach (taken from Ref. [20]) at $T = 0$.

approximation (SCMA) [49], which becomes exact only in the weak coupling limit; see Sec. II of SM [46].

We have recently developed the momentum-space HEOM method [45] that overcomes the numerical instabilities originating from the discrete bosonic bath. Within this method we calculate the time-dependent greater Green's function $G^>(k, t)$, which presents the root of the hierarchy of the auxiliary Green's functions. The hierarchy is, in principle, infinite, and one actually solves the model by truncating the hierarchy at certain depth D. The HEOM are propagated independently for each allowed value of k up to long times ($\omega_0 t_{\max} \sim 500$). The propagation takes 5 to 10 hours on 16 cores per momentum k. The discrete Fourier transform is then used to obtain spectral functions without introducing any artificial broadening. Numerical error in the HEOM solution can originate from the finite-size effects since the method is applied on the lattice with N sites, and also from the finite depth D. We always use N and D, as given in SM [46], which correctly represent the thermodynamic limit. Generally, for larger g we need smaller N and larger D. This is why the ED method with a small number of sites could be a better option in the strong coupling regime. The ED method can be used more efficiently after the initial Hamiltonian is transformed by applying the Lang-Firsov transformation; see SM [46], Sec. III.

In the QMC method, we calculate the correlation function $C_k(\tau) = \langle c_k(\tau)c_k^\dagger \rangle_{T,0}$ in imaginary time. The thermal

expectation value is performed over the states with zero electrons and $c_k(\tau) = e^{\tau H} c_k e^{-\tau H}$. We use the path integral representation, the discretization of imaginary time, and analytical calculation of integrals over the phonon coordinates. We then evaluate a multidimensional sum over the electronic coordinates by a Monte Carlo method. This method is a natural extension of early works where such approach was applied just to thermodynamic quantities [50–52]. Details of the method are presented in Ref. [45].

Results at zero temperature.—In Fig. 1(b), we show the DMFT results for the electron effective mass at the bottom of the band, $m^*/m_0 = 1 - d\mathrm{Re}\Sigma(\omega)/d\omega|_{E_p}$ (where $\Sigma(\omega)$ is the self-energy), over a broad range of parameters covering practically the whole parameter space in the (γ, λ) plane. We see that the mass renormalization is in striking agreement with the DMRG result [17,20] that presents the best available result from the literature. Small discrepancies are visible only for stronger interaction with small ω_0. A similar level of agreement can be seen in the comparison of the ground state (polaron) energy E_p in Fig. 1(c). Here, the results obtained with variational global-local method [20,21] are taken as a reference. While the agreement in the weak coupling and in the atomic limit could be anticipated since the DMFT becomes exact in these limits, we find the quantitative agreement in the crossover regime between these two limits rather surprising, having in mind that the DMFT completely neglects nonlocal correlations. It is also interesting that this was not observed earlier. The only difference from the standard reference of Ciuchi *et al.* [41] is that we applied the DMFT to the 1D case, as opposed to the Bethe lattice. This is, however, a key difference. Otherwise the DMFT provides only a qualitative description of the Holstein model [3,16,20,44,53]. From the technical side, the only difference as compared to the case of the Bethe lattice is in the self-consistency equation. For obtaining a numerically stable and precise solution, it was crucial to use an analytical expression for the self-consistency relation (see Sec. IB in SM [46]). We have also calculated the effective mass for two- and three-dimensional lattices (see Sec. IC in SM [46]) and the agreement with the QMC calculation from Ref. [19] is excellent. This was now expected since the importance of nonlocal correlations decreases in higher dimensions. A comparison with the Bethe lattice effective mass is illustrated in SM [46], Sec. ID.

The next step is to check if the agreement with the numerically exact solution extends also to spectral functions. Typical results at $k = 0$ are illustrated in Fig. 2. We note that at $T = 0$ the DMFT quasiparticle peak is a delta function (broadened in Fig. 2), while satellite peaks are incoherent having intrinsic nonzero width. In HEOM, the peak broadening due to the finite lattice size N and finite propagation time $t_{\max}$ is generally much smaller than the Lorentzian broadening used in the insets of Figs. 2(a)–2(d). The weights of the DMFT and HEOM quasiparticle peaks
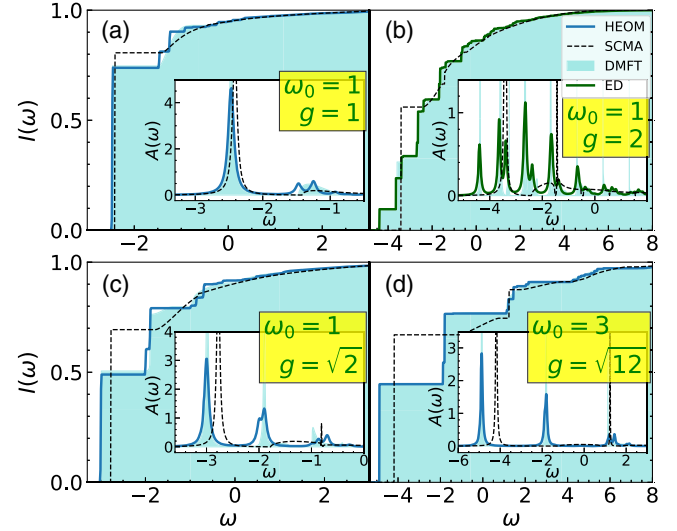

FIG. 2. (a)–(d) Integrated HEOM, DMFT, SCMA, and ED spectral weight, $I(\omega) = \int_{-\infty}^{\omega} d\nu A_k(\nu)$, for $k = 0$ and $T = 0$. The insets show comparisons of the spectral functions. $I(\omega)$ is obtained without broadening, whereas $A(\omega)$ is broadened by Lorentzians of half-width $\eta = 0.05$.

correspond to the m_0/m^* ratio. The satellite peaks are also very well captured by the DMFT solution in all parameter regimes. For $g = 1$ we can see two small peaks in the first satellite structure of the HEOM solution. We find very similar peaks also in the DMFT solution when applied on a lattice of the same size, which is here equal to 10 (see SM [46], Sec. IV). Hence, we conclude that these peaks are an artefact of the finite lattice size. In the strong coupling regime $\omega_0 = 1$, $g = 2$, the DMFT is compared with ED since the thermodynamic limit is practically reached for $N = 4$; see SM [46], Sec. IV. Here, we notice a pronounced excited quasiparticle peak [22,23] whose energy is below $E_p + \omega_0$. This peak, which consists of a polaron and a bound phonon, is also very well resolved within the DMFT solution. For parameters in Fig. 2(d) the lattice sites are nearly decoupled, approaching the atomic limit ($t_0 \ll g, \omega_0$), when the DMFT becomes exact (see Sec. V in SM [46]). For a comparison, we show also the SCMA spectral functions. As the interaction increases, the SCMA solution misses the position and the weight of the quasiparticle peak and the satellite peaks are not properly resolved. Further comparisons of zero temperature spectral functions are shown in Sec. VI of SM [46].

Results at finite temperature.—Reliable finite-T results for the spectral functions of the Holstein model have been obtained only very recently using the FTLM [23] and finite-T DMRG methods [24]. Here, we calculate the spectral functions using HEOM or ED and compare them extensively with the DMFT. The results are crosschecked using the QMC results in imaginary time.

Typical results for the spectral functions are shown in Fig. 3, while additional results for other momenta and other
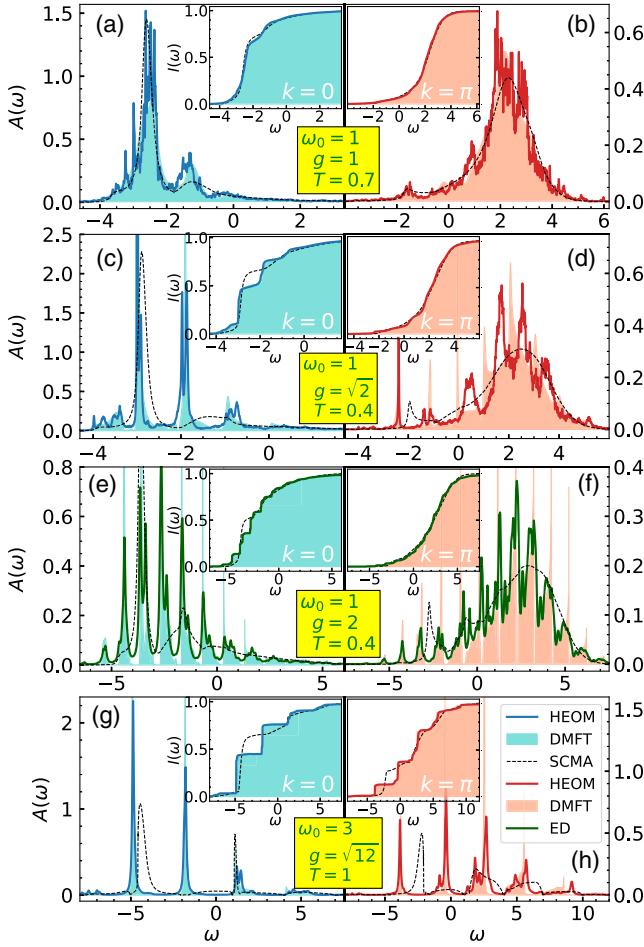
FIG. 3. (a)–(h) Spectral functions at $T > 0$ for $k = 0$ and $k = \pi$. In panels (e)–(f) only the ED results are broadened by Lorentzians of half-width $\eta = 0.05$, while all the curves are broadened in (g)–(h) with the same η. All insets are shown without broadening.

FIG. 4. (a), (b) Comparison of DMFT, HEOM, and finite-T DMRG and FTLM (taken from Ref. [24]) spectral functions at $T = 0.4$. All the lines are here broadened by Lorentzians of half-width $\eta = 0.05$. (c), (d) DMFT, QMC, HEOM, and SCMA imaginary time correlation functions at $T = 0.4$ ($T = 1$ in the insets). Here, $g = \sqrt{2}$, $\omega_0 = 1$.

parameters are shown in Sec. VII of SM [46]. We see that for $T > 0$ the satellite peaks appear also below the quasiparticle peak. The agreement between the DMFT and the HEOM (ED) spectral functions is very good. The agreement remains excellent even for $g = 2$ where the electrons are strongly renormalized $m^*/m_0 \approx 10$, which is far away from both the atomic and weak coupling limits, where the DMFT is exact. A part of the difference between the DMFT and the HEOM (ED) results can be ascribed to the small finite-size effects in the HEOM and ED solutions, as detailed in SM [46], Sec. IV. In accordance with the presented results, it is not surprising that the self-energies are nearly k independent, as shown in SM [46], Sec. VIII. It is also instructive to examine the difference between the SCMA and DMFT (HEOM) solutions. For moderate interaction [Figs. 3(a) and 3(b)], the weight of the SCMA quasiparticle peak is nearly equal to the DMFT (HEOM) quasiparticle weight, and the overall agreement of spectral functions is rather good. This is not the case for stronger
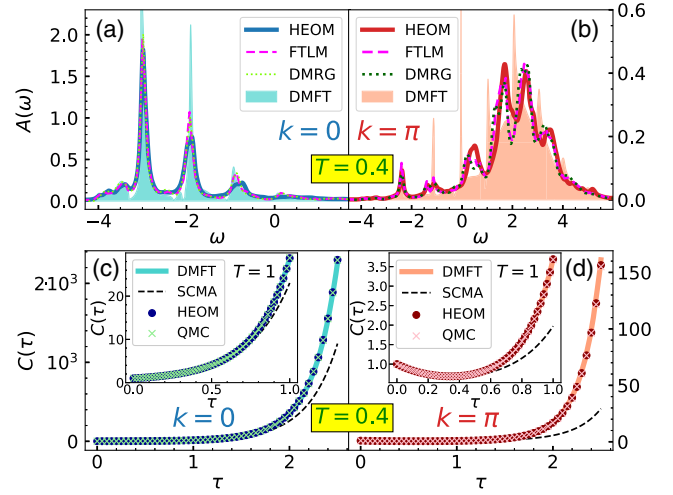
electron-phonon coupling [Figs. 3(c)–3(h)] where the SCMA poorly approximates the true spectrum.

We observe that for $g = \sqrt{2}$ and $k = \pi$ the DMFT and HEOM satellite peaks are somewhat shifted with respect to one another; see Figs. 3(c) and 3(d). This is the most challenging regime for the DMFT, representing a crossover ($\lambda = 1$) between the small and large polaron. Nevertheless, the agreement remains very good near the quasiparticle peak for $k = 0$, which will be the most important for transport in weakly doped systems. In order to gain further confidence into the details of the HEOM spectral functions for $g = \sqrt{2}$, we compare them with the available results obtained within the finite-T DMRG and Lanczos methods. We find an excellent agreement, as shown in Figs. 4(a) and 4(b).

The DMFT and HEOM results are crosschecked with the path integral QMC calculations. The quantity that we obtain in QMC is the single electron correlation function in imaginary time, which can be expressed through the spectral function as $C_k(\tau) = \int_{-\infty}^{\infty} d\omega\, e^{-\omega\tau} A_k(\omega)$. Typical results are illustrated in Figs. 4(c) and 4(d), while extensive comparisons are presented in Sec. IX of SM [46]. At $T = 0.4$ we can see a small difference in $C_\pi(\tau)$ between the DMFT and QMC (HEOM) results. At $T = 1$, both for $k = 0$ and $k = \pi$, the difference in $C_k(\tau)$ is minuscule, well below the QMC error bar, which is smaller than the symbol size. This confirms that nonlocal correlations are weak. Similarly, as for the spectral functions, the SCMA correlation functions show clear deviation from other solutions. We, however, note that great care is needed when drawing conclusions from the imaginary axis data since a very small difference in the imaginary axis correlation functions can correspond to substantial differences in spectral functions.

Conclusions.—In summary, we have presented a comprehensive solution of the 1D Holstein polaron covering all parameter regimes. We showed that the DMFT is a remarkably good approximation in the whole parameter space. This approximation is simple, numerically efficient, and can also be easily applied in two and three dimensions. We successfully used momentum-space HEOM and ED methods for comparisons with the DMFT spectral functions both at zero and at finite temperature. The comparisons showed an excellent agreement between the spectral functions in most of the parameter space. For parameters that are most challenging for the DMFT, a very good agreement was found around $k = 0$ and a reasonably good agreement was obtained at larger values of k. All of the results are crosschecked with the imaginary axis QMC calculations and with the available results from the literature. Both the DMFT and HEOM methods are implemented directly in real frequency, without artificial broadening of the spectral functions. This will be crucial in order to calculate dynamical quantities and determine a potential role of the vertex corrections to conductivity by avoiding possible pitfalls of the analytical continuation, which we leave as a challenge for future work.

[1] T. Holstein, Ann. Phys. (N.Y.) **8**, 325 (1959).

[2] A. S. Alexandrov, *Polarons in Advanced Materials* (Springer, New York, 2007).

[3] C. Franchini, M. Reticcioli, M. Setvin, and U. Diebold, Nat. Rev. Mater. **6**, 560 (2021).

[4] L. Vidmar, J. Bonča, M. Mierzejewski, P. Prelovšek, and S. A. Trugman, Phys. Rev. B **83**, 134301 (2011).

[5] B. Kloss, D. R. Reichman, and R. Tempelaar, Phys. Rev. Lett. **123**, 126601 (2019).

[6] C. Brockt and E. Jeckelmann, Phys. Rev. B **95**, 064309 (2017).

[7] N. Prodanović and N. Vukmirović, Phys. Rev. B **99**, 104304 (2019).

[8] J. Stolpp, J. Herbrych, F. Dorfner, E. Dagotto, and F. Heidrich-Meisner, Phys. Rev. B **101**, 035134 (2020).

[9] Y. Murakami, P. Werner, N. Tsuji, and H. Aoki, Phys. Rev. B **91**, 045128 (2015).

[10] D. Jansen, J. Stolpp, L. Vidmar, and F. Heidrich-Meisner, Phys. Rev. B **99**, 155130 (2019).

[11] J. H. Fetherolf, D. Golež, and T. C. Berkelbach, Phys. Rev. X **10**, 021062 (2020).

[12] A. S. Mishchenko, N. Nagaosa, and N. Prokof'ev, Phys. Rev. Lett. **113**, 166402 (2014).

[13] M. Kang, S. W. Jung, W. J. Shin, Y. Sohn, S. H. Ryu, T. K. Kim, M. Hoesch, and K. S. Kim, Nat. Mater. **17**, 676 (2018).

[14] G. Mahan, *Many-Particle Physics* (Kluwer Academic, New York, 2000).

[15] I. Lang and Y. A. Firsov, Zh. Eksp. Teor. Fiz. **43**, 1843 (1962) [Sov. Phys. JETP **16**, 1301 (1963)].

[16] A. S. Alexandrov and J. T. Devreese, *Advances in Polaron Physics* (Springer, New York, 2010).

[17] E. Jeckelmann and S. R. White, Phys. Rev. B **57**, 6376 (1998).

[18] C. Zhang, E. Jeckelmann, and S. R. White, Phys. Rev. B **60**, 14092 (1999).

[19] P. E. Kornilovitch, Phys. Rev. Lett. **81**, 5382 (1998).

[20] A. H. Romero, D. W. Brown, and K. Lindenberg, J. Chem. Phys. **109**, 6540 (1998).

[21] A. H. Romero, D. W. Brown, and K. Lindenberg, Phys. Rev. B **59**, 13728 (1999).

[22] J. Bonča, S. A. Trugman, and I. Batistić, Phys. Rev. B **60**, 1633 (1999).

[23] J. Bonča, S. A. Trugman, and M. Berciu, Phys. Rev. B **100**, 094307 (2019).

[24] D. Jansen, J. Bonča, and F. Heidrich-Meisner, Phys. Rev. B **102**, 165155 (2020).

[25] Y. Tanimura, J. Chem. Phys. **153**, 020901 (2020).

[26] R.-X. Xu and Y. J. Yan, Phys. Rev. E **75**, 031107 (2007).

[27] J. Jin, X. Zheng, and Y. J. Yan, J. Chem. Phys. **128**, 234703 (2008).

[28] D. Hou, R. Wang, X. Zheng, N. H. Tong, J. H. Wei, and Y. J. Yan, Phys. Rev. B **90**, 045141 (2014).

[29] Z. H. Li, N. H. Tong, X. Zheng, D. Hou, J. H. Wei, J. Hu, and Y. J. Yan, Phys. Rev. Lett. **109**, 266403 (2012).

[30] L. Chen, Y. Zhao, and Y. Tanimura, J. Phys. Chem. Lett. **6**, 3110 (2015).

[31] L. Song and Q. Shi, J. Chem. Phys. **142**, 174103 (2015).

[32] L. Song and Q. Shi, J. Chem. Phys. **143**, 194106 (2015).

[33] I. S. Dunn, R. Tempelaar, and D. R. Reichman, J. Chem. Phys. **150**, 184109 (2019).

[34] Y. Yan, T. Xing, and Q. Shi, J. Chem. Phys. **153**, 204109 (2020).

[35] M. Hohenadler, M. Aichhorn, and W. von der Linden, Phys. Rev. B **68**, 184304 (2003).

[36] G. De Filippis, V. Cataudella, V. Marigliano Ramaglia, and C. A. Perroni, Phys. Rev. B **72**, 014307 (2005).

[37] M. Berciu, Phys. Rev. Lett. **97**, 036402 (2006).

[38] G. L. Goodvin, M. Berciu, and G. A. Sawatzky, Phys. Rev. B **74**, 245104 (2006).

[39] A. Georges, G. Kotliar, W. Krauth, and M. J. Rozenberg, Rev. Mod. Phys. **68**, 13 (1996).

[40] R. M. Martin, L. Reining, and D. M. Ceperley, *Interacting Electrons: Theory and Computational Approaches* (Cambridge University Press, Cambridge, England, 2016).

[41] S. Ciuchi, F. de Pasquale, S. Fratini, and D. Feinberg, Phys. Rev. B **56**, 4494 (1997).

[42] S. Fratini, F. de Pasquale, and S. Ciuchi, Phys. Rev. B **63**, 153101 (2001).

[43] S. Fratini and S. Ciuchi, Phys. Rev. Lett. **91**, 256403 (2003).

[44] L.-C. Ku, S. A. Trugman, and J. Bonča, Phys. Rev. B **65**, 174306 (2002).

[45] V. Janković and N. Vukmirović, Phys. Rev. B **105**, 054311 (2022).

[46] See Supplemental Material at http://link.aps.org/supplemental/10.1103/PhysRevLett.129.096401 for detailed analysis and supporting data.

[47] J. Vučičević, J. Kokalj, R. Žitko, N. Wentzell, D. Tanasković, and J. Mravlje, Phys. Rev. Lett. **123**, 036601 (2019).

[48] A. Vranić, J. Vučičević, J. Kokalj, J. Skolimowski, R. Žitko, J. Mravlje, and D. Tanasković, Phys. Rev. B **102**, 115142 (2020).

[49] A. Migdal, Zh. Eksp. Teor. Fiz. **34**, 1438 (1958) [Sov. Phys. JETP **7**, 996 (1958)].

[50] H. De Raedt and A. Lagendijk, Phys. Rev. Lett. **49**, 1522 (1982).

[51] H. De Raedt and A. Lagendijk, Phys. Rev. B **27**, 6097 (1983).

[52] H. De Raedt and A. Lagendijk, Phys. Rev. B **30**, 1671 (1984).

[53] O. S. Barišić, Phys. Rev. B **76**, 193106 (2007).

Supplemental Material: Spectral functions of the Holstein polaron: exact and approximate solutions

Petar Mitrić,[1] Veljko Janković,[1] Nenad Vukmirović,[1] and Darko Tanasković[1]

[1]*Institute of Physics Belgrade, University of Belgrade, Pregrevica 118, 11080 Belgrade, Serbia*

Here we present numerical results that complement the main text and we also show some technical details of the calculations. The Supplemental Material is organized as follows. The DMFT for the Holstein polaron is briefly reviewed in Sec. I. Numerical implementation of the DMFT self-consistency loop is presented in detail and it is used to calculate the mass renormalization in one, two and three dimensions and for the Bethe lattice as well. In Sec. II the self-consistent Migdal approximation is briefly reviewed and used as a benchmark for the DMFT in the weak-coupling limit. Sec. III presents the ED method. In Sec. IV we investigate how the results depend on the chain length N and on hierarchy depth D. Sec. V examines the DMFT solution close to the atomic limit. Additional DMFT, SCMA, ED and HEOM results for the spectral functions at $T = 0$ and $T > 0$ for various parameter values and for different momenta k are shown in Secs. VI and VII, respectively. The k-dependence of the self-energies is shown in Sec. VIII. A detailed comparison of the DMFT, HEOM and QMC correlation functions is presented in Sec. IX. Sec. X presents a numerical procedure that was used for the calculation of the integrated spectral weight. In Sec. XI we show that the different definitions of spectral functions used by various methods are all in agreement.

FIG. S1. DMFT self-consistency loop.

I. DMFT FOR THE HOLSTEIN POLARON

The DMFT solution for the Holstein polaron on the infinitely-connected Bethe lattice was presented by Ciuchi *et al.* in 1997 [S1]. Interestingly, to our knowledge, this method has not been so far implemented on a finite-dimensional lattice. Details of the implementation in 1d and in arbitrary number of dimensions are the main content of this Section.

A. Physical content of the DMFT approximation

The DMFT was developed in the early 1990's in the context of the Hubbard model [S2] and has since significantly contributed to our understanding of the systems with strong electronic correlations [S3]. The DMFT is a non-perturbative method that fully takes into acc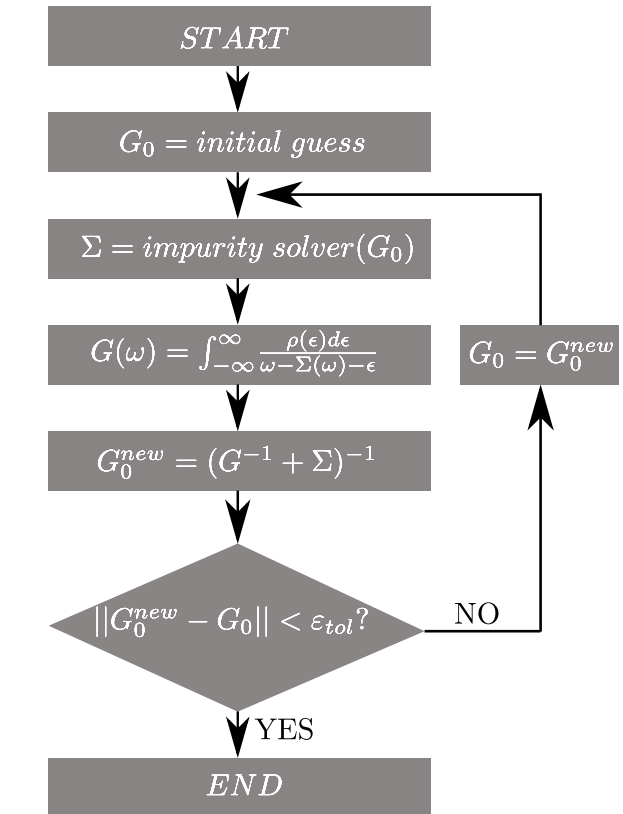ount local quantum fluctuations. It becomes exact in the limit of infinite coordination number [S2], while it can be considered as an approximation in finite number of dimensions that keeps only local correlations by assuming that the self-energy $\Sigma(\omega)$ is **k**-independent.

In practice, the DMFT reduces to solving the (Anderson) impurity problem in a frequency dependent Weiss field $G_0(\omega)$ that needs to be determined self-consistently. The bare propagator (Weiss field) $G_0(\omega)$ is responsible for the electron fluctuations between the impurity and the reservoir (conduction bath). On-site correlation is taken into account through the self-energy. The connection with the lattice problem is established by the requirement that the impurity self-energy $\Sigma_{\mathrm{imp}}(\omega)$ is equal to the lattice self-energy $\Sigma_{ii}(\omega)$ (while the nonlocal components $\Sigma_{ij}(\omega)$ are equal to zero within DMFT) and that the impurity Green's function $G_{\mathrm{imp}}(\omega)$ is equal to the local lattice Green's func-

$$\Sigma = \text{[diagram]} + \text{[diagram]} + \text{[diagram]} + \cdots$$
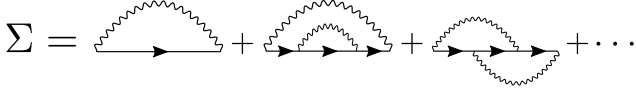
FIG. S2. First few DMFT Feynman diagrams of the self-energy in the expansion over G_0.

tion $G_{ii}(\omega) = \frac{1}{N}\sum_{\mathbf{k}} G_{\mathbf{k}}(\omega)$. The DMFT equations are solved iteratively as shown schematically in Fig. S1. For a given bare propagator G_0 an *impurity solver* is used to obtain the self-energy, and then the self-consistency is imposed by the Dyson equation. The subscripts for the impurity and the local lattice Green's function are omitted since these two quantities coincide when the self-consistency is reached.

The DMFT solution for the Holstein polaron follows the general concepts introduced for the Hubbard model with an important simplification which comes from the fact that we consider the dynamics of just a single electron. We briefly review some key aspects and for details we refer the reader to Ref. [S1].

The self-energy for the polaron impurity, which is coupled to the reservoir by the bare propagator $G_0(\omega)$, can be simply expressed in a form of the continued-fraction expansion (CFE), which is in a sharp contrast with the Hubbard model where the numerical solution of the Anderson impurity model is the most difficult step. Here, the self-energy at $T = 0$ is simply given by

$$\Sigma(\omega) = \cfrac{g^2}{G_0^{-1}(\omega - \omega_0) - \cfrac{2g^2}{G_0^{-1}(\omega - 2\omega_0) - \cfrac{3g^2}{G_0^{-1}(\omega - 3\omega_0) - \ldots}}}$$
(S1)

(For a derivation and generalization to $T > 0$ see Ref. [S1].) This expansion has an infinite number of terms and in practice it needs to be truncated. In order to understand which condition needs to be fulfilled for a truncation, we will look at the diagrammatic expansion of the self-energy.

For a single electron (i.e. in the zero density limit) the Feynman diagrams of the self-energy consist of a single electron line accompanied by the lines that describe the emission and the absorption of phonons. There are no bubble diagrams and hence there is no renormalization of the phonon propagator. As an illustration, a diagrammatic expansion over $G_0(\omega)$ up to the order g^4 is shown in Fig. S2. These diagrams are included if we keep the terms up to the second stage in the CFE.

There are two important implications from this diagrammatic expansion. First, if we keep in the expansion terms up to the order g^{2N} then only the phonon states $|n\rangle$ with $n \leq N$ appear as intermediate states. Therefore, since the importance of the multiphonon effects

can be estimated by the parameter $\alpha^2 = g^2/\omega_0^2$ [S4], we need to keep $N \gg \alpha^2$ terms in the CFE. Second, we see that the vertex corrections (involving the phonons on the same site in the real-space representation [S5]) are included in the DMFT solution. This should be contrasted with the self-consistent Migdal approximation (SCMA) which completely neglects the vertex corrections in the self-energy. However, we note that one should be careful in making a direct comparison to the SCMA, since the DMFT diagrams are expanded using G_0, unlike the SCMA.

B. Numerical implementation of the DMFT loop

We will now discuss step by step the self-consistency loop shown in Fig. S1. The DMFT loop starts by guessing the solution for the free propagator $G_0(\omega)$. Better guesses lead to fewer number of iterations, so depending on the parameter regime we take $G_0(\omega)$ to be either the Green's function in the Migdal approximation (S20) or the Green's function in the atomic limit (S25), since both of these expressions are analytically known. They correspond to the cases of very weak coupling and vanishing hopping, respectively. Next, the self-energy $\Sigma(\omega)$ is calculated using the impurity solver (S1) and its generalization to finite temperatures [S1]. In practice these are implemented using the recursion relations, which at finite temperature read as:

$$\Sigma(\omega) = G_0^{-1}(\omega) - G^{-1}(\omega), \quad \text{(S2a)}$$

$$G(\omega) = \sum_{n=0}^{\infty} \frac{(1 - e^{-\omega_0/T})e^{-n\omega_0/T}}{G_0^{-1}(\omega) - A_n^{(0)}(\omega) - B_n^{(0)}(\omega)}, \quad \text{(S2b)}$$

$$A_n^{(p)}(\omega) = \frac{(n-p)g^2}{G_0^{-1}(\omega + (p+1)\omega_0) - A_n^{(p+1)}(\omega)}, \quad \text{(S2c)}$$

$$B_n^{(p)}(\omega) = \frac{(n+p+1)g^2}{G_0^{-1}(\omega - (p+1)\omega_0) - B_n^{(p+1)}(\omega)}, \quad \text{(S2d)}$$

$$A_n^{(n)}(\omega) = 0, \quad B_n^{(\infty)}(\omega) = 0. \quad \text{(S2e)}$$

Quantities $A_n^{(p)}$ and $B_n^{(p)}$ are determined recursively, starting from (S2e) and going back to (S2d) and (S2c). Then, $G(\omega)$ is calculated using (S2b), which enables us to use Dyson Eq. (S2a) to obtain $\Sigma(\omega)$. For $T = 0$ the equations simplify and the self-energy can be written as $\Sigma(\omega) = B_0^{(0)}(\omega)$, which coincides with Eq. (S1). The physical interpretation of the quantities in Eq. (S2) is the following: $G(\omega)$ is the interacting Green's function of the impurity. The quantity $A_n^{(0)}(\omega)$ is just a finite fraction that takes into account the emission of phonons. Similarly, $B_n^{(0)}(\omega)$ is an infinite continued fraction, which takes into account the absorption of phonons. The infinite fraction $B_n^{(0)}(\omega)$ can be calculated accurately even if we truncate it $B_n^{(N)}(\omega) = 0$,

taking N to be a number much larger than α^2. The infinite series (S2b) can also be truncated by using the number of terms $n_{max} \gg T/\omega_0$ [S1].

Next step in the DMFT loop is calculating the local Green's function of the lattice using the self-energy $\Sigma(\omega)$ from the impurity solver. It is calculated as

$$G(\omega) = \int_{-\infty}^{\infty} \frac{\rho(\epsilon)d\epsilon}{\omega - \Sigma(\omega) - \epsilon}, \qquad (S3)$$

where $\rho(\epsilon)$ is the noninteracting density of states. This integral is convergent since we are integrating below the complex pole $\epsilon = \omega - \Sigma(\omega)$, as a consequence of the causality $\mathrm{Im}\,\Sigma(\omega) < 0$. However, numerical instabilities can arise due to the fact that the complex pole can be arbitrarily close to the real axis. Hence, the numerical integration of Eq. (S3) requires additional care. In Sec. I B 2 we present a numerical procedure which solves this problem. However, in the 1d case these numerical instabilities are completely avoided since Eq. (S3) admits an analytical solution, as shown in Sec. I B 1.

Following the DMFT algorithm from Fig. S1, we now calculate the next iteration of the free propagator using the Dyson equation

$$G_0^{\mathrm{new}}(\omega) = [G^{-1}(\omega) + \Sigma(\omega)]^{-1}. \qquad (S4)$$

We check if $|G_0^{new}(\omega) - G_0(\omega)| < \varepsilon_{\mathrm{tol}}$ (for each ω), where $\varepsilon_{\mathrm{tol}}$ is the tolerance parameter that we typically set to $\varepsilon_{tol} \sim 10^{-4}$ or smaller. If this condition is satisfied, the DMFT loop terminates and Σ, G_0 and G are found. Otherwise, G_0^{new} is used in the impurity solver and the procedure is repeated until convergence is reached.

After the DMFT loop has been completed, we can use the calculated self-energy $\Sigma(\omega)$ to find the retarded Green's function of our original problem

$$G_{\mathbf{k}}(\omega) = \frac{1}{\omega - \Sigma(\omega) - \varepsilon_{\mathbf{k}}}. \qquad (S5)$$

The spectral function is then simply given by

$$A_{\mathbf{k}}(\omega) = -\frac{1}{\pi}\mathrm{Im}G_{\mathbf{k}}(\omega). \qquad (S6)$$

1. Self-consistency equation for the local Green's function in one dimension

Let us now show how the local Green's function (S3) can be analytically evaluated in a 1d system with nearest neighbor hopping t_0. The noninteracting density of states reads as

$$\rho(\epsilon) = \frac{\theta(4t_0^2 - \epsilon^2)}{\pi\sqrt{4t_0^2 - \epsilon^2}}, \qquad (S7)$$

where θ is the Heaviside step function. Equation (S3) can be rewritten using the substitution $\epsilon = 2t_0 \sin x$

$$G(\omega) = \frac{1}{4t_0\pi} \int_{-\pi}^{\pi} \frac{dx}{B - \sin x}, \qquad (S8)$$

where we introduced

$$B = (\omega - \Sigma(\omega))/2t_0. \qquad (S9)$$

Additional substitution $z = e^{ix}$ leads us to

$$G(\omega) = -\frac{1}{2t_0\pi} \oint_C \frac{dz}{(z - z_+)(z - z_-)}, \qquad (S10)$$

where this represents the counterclockwise complex integral over the unit circle C and $z_{\pm} = iB \pm \sqrt{1 - B^2}$. In order to apply the method of residues, we first need to find out if $z_{\pm}$ are inside the complex unit circle $|z| = 1$. Causality implies that $\mathrm{Im}\,\Sigma(\omega) < 0$ which means that $\mathrm{Im}\,B > 0$. In this case one can show that $|z_+| < 1$ and $|z_-| > 1$, which means that only the pole at z_+ gives a non-vanishing contribution to the Eq. (S10)

$$G(\omega) = \frac{-i}{2t_0\sqrt{1 - B^2}} = \frac{1}{2t_0 B\sqrt{1 - \frac{1}{B^2}}}. \qquad (S11)$$

In Eq. (S11) we wrote the solution in two ways. They are completely equivalent in our case when $\mathrm{Im}\,B > 0$, but can otherwise give different results. Since B can be arbitrarily close to the real axis, it is important to ensure additional numerical stability by requiring that the expression for $G(\omega)$ satisfies that the $\mathrm{Im}\,B = 0$ solution coincides with the solution in the limit $\mathrm{Im}\,B \to 0$. This is not satisfied by the expressions in Eq. (S11), but it can be achieved by combining their imaginary and real parts

$$G(\omega) = \mathrm{Re}\,\frac{1}{2t_0 aB\sqrt{1 - \frac{1}{B^2}}} + i\,\mathrm{Im}\,\frac{-i}{2t_0 a\sqrt{1 - B^2}}. \qquad (S12)$$

2. Self-consistency equation for the local Green's function in arbitrary number of dimensions

Here we present a numerical procedure for the calculation of the local Green's function (S3) for arbitrary density of states $\rho(\epsilon)$, that completely eliminates the potential numerical singularity at $\epsilon = \omega - \Sigma(\omega)$. This is particularly important since the techniques presented in Sec. I B 1 fail when the dispersion relation even slightly changes. It is also relevant in the higher-dimensional systems where the density of states is not necessarily analytically know.

Let us suppose that the self-energy and the density of states are known only on a finite, equidistant grid $\omega_0, \omega_1 ... \omega_{N-1}$, where $\Delta\omega = \omega_{i+1} - \omega_i$. Further, suppose that the density of states is vanishing outside some closed interval $[D_1, D_2]$ and that the grid is wide enough so that there are at least a couple of points outside that closed interval: $\rho(\omega_0) = ... = \rho(\omega_3) = 0$ and $\rho(\omega_{N-1}) = ... = \rho(\omega_{N-4}) = 0$. These are quite general assumptions that are always satisfied in the systems we are examining. The local Green's function can now be rewritten as

$$G(\omega) = \sum_{i=0}^{N-2} \int_{\omega_i}^{\omega_{i+1}} d\epsilon \frac{\rho(\epsilon)}{\omega - \Sigma(\omega) - \epsilon}. \qquad (S13)$$

At each sub-interval $[\omega_i, \omega_{i+1}]$ the density of states is only known at the endpoints, so it is natural to approximate it using a linear function

$$\rho(\epsilon) = a_i + b_i(\epsilon - \omega_i), \qquad (S14)$$

where $a_i = \rho(\omega_i)$, $b_i = (\rho(\omega_{i+1}) - \rho(\omega_i))/\Delta\omega$. Introducing a shorthand notation $\xi = \omega - \Sigma(\omega)$, we evaluate Eq. (S13) analytically

$$\begin{aligned}
G(\omega) = &\sum_{i=0}^{N-2} b_i(\omega_i - \omega_{i+1}) \\
&+ \sum_{i=0}^{N-2} a_i \left[\ln(\xi - \omega_i) - \ln(\xi - \omega_{i+1})\right] \\
&+ \sum_{i=0}^{N-2} b_i(\xi - \omega_i)\left[\ln(\xi - \omega_i) - \ln(\xi - \omega_{i+1})\right].
\end{aligned} \qquad (S15)$$

The first line is just a telescoping series that is vanishing

$$\sum_{i=0}^{N-2} b_i(\omega_i - \omega_{i+1}) = \rho(\omega_0) - \rho(\omega_{N-1}) = 0. \qquad (S16)$$

The last two lines in Eq. (S15) can be transformed by shifting the indices $i+1 \to i$, taking into account that a few boundary terms are vanishing and using the identity $a_i - a_{i-1} = (\omega_i - \omega_{i-1})b_{i-1}$

$$\begin{aligned}
G(\omega) = &\sum_{i=0}^{N-2} \frac{\rho(\omega_{i+1}) - 2\rho(\omega_i) + \rho(\omega_{i-1})}{\Delta\omega} \\
&\times (\omega - \omega_i - \Sigma(\omega)) \ln(\omega - \omega_i - \Sigma(\omega)). \quad (S17)
\end{aligned}$$

This expression now has no numerical instabilities. This is most easily seen from the fact that it has the form $x \ln x$ which is well defined even in the limit $x \to 0$, where it vanishes. Of course, the results were obtained by using the linear interpolation of the density of states.
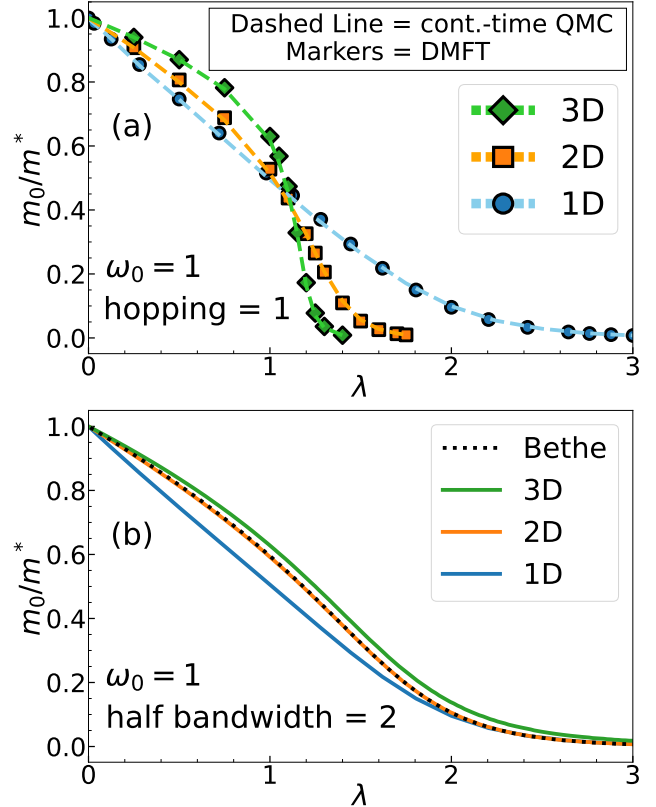

FIG. S3. (a) Continuous-time QMC (taken from Ref. S6) vs. DMFT mass renormalization in 1d, 2d and 3d, with $\omega_0 = 1$. (b) Comparison of the DMFT mass renormalization on different lattices.

This is completely justified if $\rho(\epsilon)$ is smooth or has finitely many cusps. However, the presence of van Hove singularities in $\rho(\epsilon)$ may require some special analytical treatment around them.

C. Effective mass in 1d, 2d and 3d

The DMFT mass renormalization is calculated in one, two and three dimensions. These are then compared to the continuous-time path-integral quantum Monte Carlo (QMC) results from Ref. S6. In that paper it was noted that the numerical accuracy of the QMC method is $0.1\% - 0.3\%$. The results are presented in Fig. S3(a). We note that the definition of λ and γ is slightly different than the one we gave in the main text. Here

$$\lambda = \frac{g^2}{\omega_0 W/2}; \quad \gamma = \frac{\omega_0}{W/2}, \qquad (S18)$$

where $W/2$ is the half bandwidth. This coincides with our previous definition in 1d, but gives an extra normalization in higher dimensions.
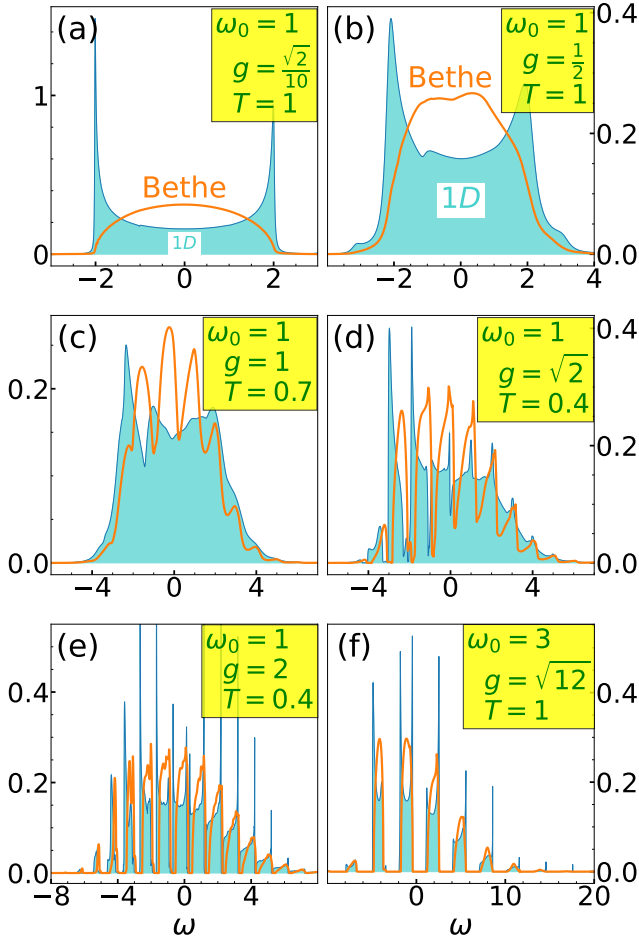
FIG. S4. 1d vs Bethe DMFT local spectral functions.

FIG. S5. 2d vs Bethe DMFT local spectral functions.

D. Comparisons with the Bethe lattice results

In the main text we emphasized that the misconception about the validity of the DMFT in 1d appeared since only the DMFT results on the Bethe lattice were used in comparisons with other methods [S7, S8]. In this section we illustrate why such comparison is inappropriate.

The main difference in practical implementation, compared to 1d, can be ascribed to the self-consistency condition for the Bethe lattice (corresponding to the semi-elliptic density of states) which can be formulated using a simple algebraic equation [S1]

$$G_0(\omega) = \left(\omega - \frac{(W/2)^2}{4}G(\omega)\right)^{-1}. \qquad (S19)$$

In Fig. S3(b) we compare the DMFT mass renormalization on different lattices using the same half-bandwidth. There is a clear discrepancy between the 1d and the Bethe lattice results, in accordance with the already mentioned earlier works.

The Bethe lattice lacks a dispersion relation since it has no translational symmetry. Therefore in Fig. S4 we compare only the local spectral functions $A(\omega) = -\frac{1}{\pi}\mathrm{Im}G(\omega) = -\frac{1}{\pi}\mathrm{Im}\frac{1}{N}\sum_k G_k(\omega)$ of the Bethe and 1d lattice. For small couplings, the spectral functions resemble the noninteracting density of state and we find a large discrepancy, as shown in panels (a) and (b). In contrast, close to the atomic limit in Fig. S4(f) spectral functions become more alike. We note that the regimes at panels (c)-(f) are the same as in Fig. 3 from the main text.

It is rather surprising that there is a striking agreement between the effective mass for 2d and the Bethe lattice as shown in Fig. S3(b), even though the noninteracting density of states are different, Fig. S5(a). Interestingly, we can see from Fig. S5 that the local spectral functions become very similar already for moderate interactions.

II.   WEAK-COUPLING LIMIT

In this section we introduce the self-consistent Migdal approximation (SCMA) and use it as a benchmark for the DMFT in the weak-coupling limit, where SCMA is exact. More importantly, we can examine a deviation of SCMA from DMFT for stronger couplings, which is shown in the main text and in the following sections of the SM.

A.   Migdal approximation

The Migdal approximation [S9], as shown in Fig. S6, is defined by taking into account only the lowest order Feynman diagram in the perturbation expansion of the self-energy.
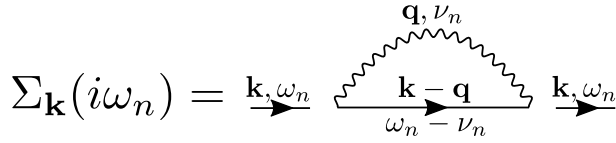
FIG. S6.   Feynman diagrams of the self-energy in the Migdal approximation

Due to its simplicity it can be evaluated analytically

$$\Sigma_k(\omega) = g^2(b+1)S(\omega - \omega_0) + g^2 b\, S(\omega + \omega_0), \quad \text{(S20)}$$

where $b \equiv b(\omega_0) = (e^{\omega_0/T} - 1)^{-1}$ and

$$S(\omega) = (\omega^2 - 4t_0^2)^{-1/2} \quad \text{for } \omega > 0,$$

while the solution for $\omega < 0$ can be obtained by noting that $\text{Im}S(\omega)$ and $\text{Re}S(\omega)$ are symmetric and antisymmetric functions, respectively. However, this solution is accurate only for very small coupling g. For larger coupling a much better solution is obtained within the self-consistent Migdal approximation.

B.   Self-consistent Migdal approximation
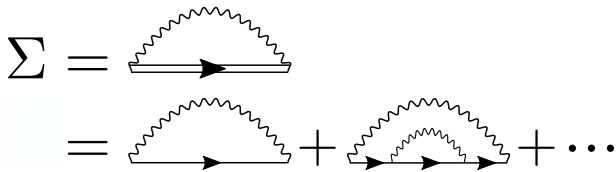
FIG. S7.   Feynman diagrams in the SCMA approximation.

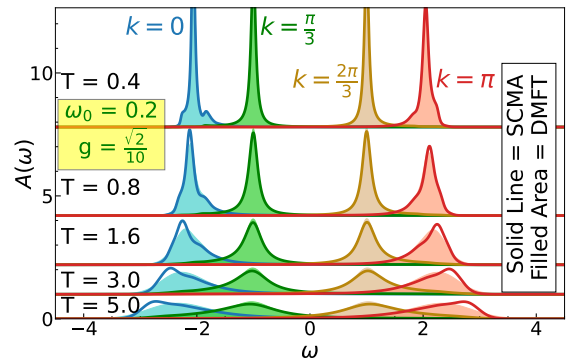In the SCMA, free fermionic propagator from Fig. S6 is replaced with the interacting propagator, as shown in
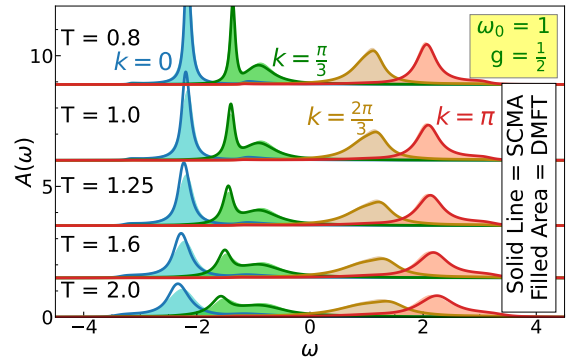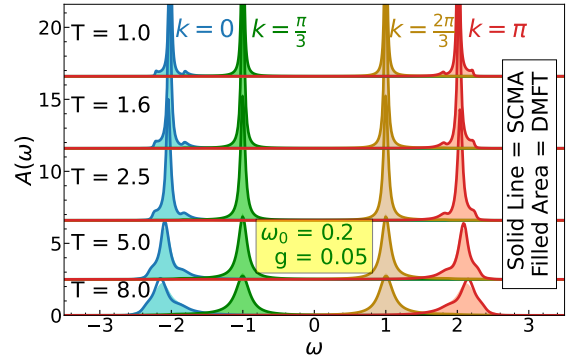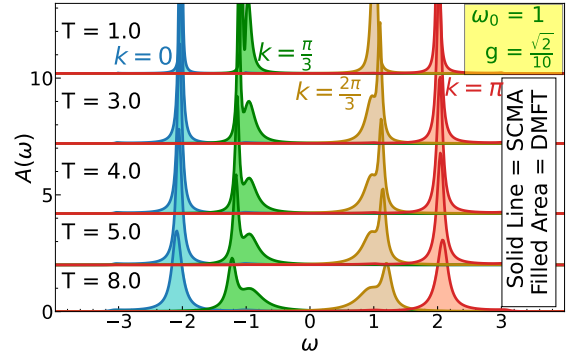

FIG. S8. DMFT vs. SCMA spectral functions in the weak-coupling regime.

Fig. S7. The corresponding equation for the self-energy can be written as

$$\Sigma_k(\omega) = g^2(b+1)G(\omega - \omega_0) + g^2 b\, G(\omega + \omega_0), \quad \text{(S21)}$$

where $G(\omega) = \frac{1}{N}\sum_k G_k(\omega)$ is the local Green's function. Equation (S21) needs to be solved self-consistently, since the Green's function can be expressed in terms of the self-energy (via the Dyson equation).

Using the expansion with respect to the free propagator, the formal solution for the self-energy can be written as an infinite series of non-crossing diagrams, as shown in Fig. S7. We see that the first term represents the Feynman diagram in the Migdal approximation. It is thus not at all surprising that the SCMA range of validity is much larger than the one-shot Migdal approximation.

We note that the SCMA self-energy is momentum-independent, which follows from Eq. (S21), making this method numerically cheap.

C. DMFT vs. SCMA in the weak coupling limit

A comparison of the DMFT and SCMA spectral functions in the weak coupling limit is shown in Fig. S8. Results almost fully coincide. As the electron-phonon coupling increases, the SCMA spectral functions starts to deviate from the exact solution, as we see from the main text and from the remaining part of the Supplemental Material.

III. STRONG COUPLING: EXACT DIAGONALIZATION

In the strong coupling regime we can approach the solution in the thermodynamic limit by using a small number of lattice sites. In SM Sec. IV we show that for $g = 2$, $\omega_0 = 1$ we are close to thermodynamic limit by considering a chain of just $N = 4$ sites. In this case we can reach a solution using the exact diagonalization (ED). In the following we describe our implementation of the ED method.

We calculate the spectral function by diagonalizing the Holstein Hamiltonian in the space spanned by the vectors $Uc_i^\dagger |n_1 n_2 \ldots n_N\rangle$, where n_i is the number of phonons at site $i \in \{1, \ldots, N\}$, satisfying $\sum_i n_i < n_{\max}$, while U is the unitary operator of the Lang-Firsov transformation [S10] given as

$$U = e^{\frac{g}{\omega_0} \sum_i c_i^\dagger c_i \left(a_i - a_i^\dagger\right)}. \tag{S22}$$

Both N and $n_{\max}$ need to be increased until convergence is reached. The spectral function is then calculated as

$$A_{\mathbf{k}}(\omega) = \frac{1}{Z_p} \sum_p e^{-\beta E_p} \sum_e \delta(\omega + E_p - E_e) |\langle p|c_{\mathbf{k}}|e\rangle|^2, \tag{S23}$$

where $|p\rangle$ denotes purely phononic states, the energy of which is E_p, $|e\rangle$ denotes the states with one electron and arbitrary number of phonons, the energy of which is E_e and $Z_p = \sum_p e^{-\beta E_p}$ is the phononic partition function. We found that convergent results for the spectral function when $g = 2$, $\omega_0 = 1$, $N = 4$ could be obtained for $n_{\max} = 16$. The results are shown in Figs. S16-S21, as well as in Figs. 2(b) and 3(e)-(f) of the main text. The spectral functions at $\mathbf{k}$ points different than $k = \frac{2\pi}{N}i$, $i \in \{0, \ldots, N - 1\}$ were obtained by employing so-called twisted boundary conditions, that is by changing the terms in the Hamiltonian $t_0 c_i^\dagger c_{i+1} \to t_0 e^{i\phi} c_i^\dagger c_{i+1}$ and $t_0 c_{i+1}^\dagger c_i \to t_0 e^{-i\phi} c_{i+1}^\dagger c_i$. The spectral function obtained from such a modified Hamiltonian corresponds then to the spectral function at $k + \phi$.

IV. FINITE-SIZE EFFECTS AND HEOM DEPTH

The numerically exact HEOM, QMC and ED methods are implemented on a 1d lattice of length N. Results which are representative of the thermodynamic limit can be obtained by taking large enough N. Furthermore, the hierarchy of HEOM needs to be truncated using sufficient depth D. In the ED method the number of phonons in the Hilbert space need to be specified. All of these parameters should be as large as possible, but the practical numerical implementation is restricted by the available computer memory. Finite-N and finite-D analysis was performed in all parameter regimes where we have HEOM results. In Figs. S9, S10, and S11 we briefly illustrate such analysis in the intermediate and strong coupling regime.

The optimal value of D strongly depends on the interaction strength and temperature. For large interaction we need large D since many phonon states are populated even at $T = 0$. Similarly, larger temperature also requires larger HEOM depth. As illustrated in Fig. S9(a)-(b), for $\omega_0 = 1$, $g = 1$ the convergence is nearly reached already for $D = 6$. For $g = \sqrt{2}$ (Fig. S10(a)-(b)), we need slightly larger D. However, in the strong-coupling regime for $g = 2$ we need much larger D, and from a comparison with the ED results for $N = 4$ in Fig. S11 we can conclude that the HEOM result has rather well converged only for $D = 17$. We can also observe that the results at $k = 0$ typically converge faster with respect to D than the results at $k = \pi$.

The value N for which the spectral functions correspond to those in the thermodynamic limit also depends on the
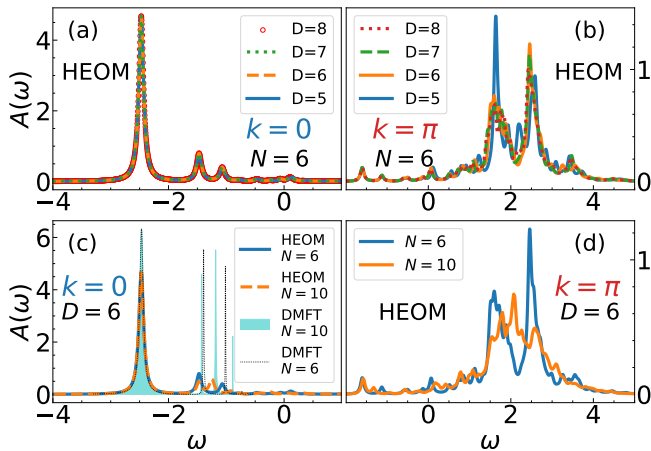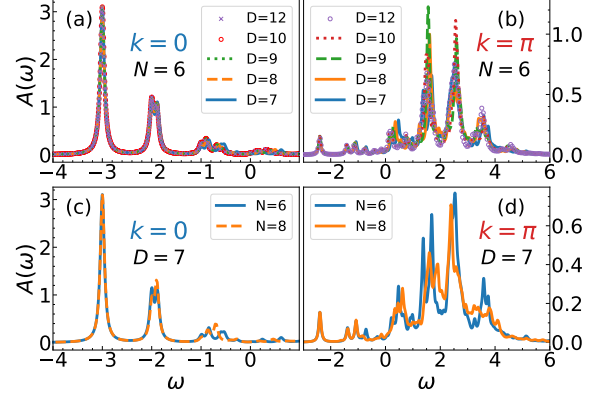

FIG. S10.   Finite-N and finite-D effects in the HEOM at intermediate coupling $\omega_0 = 1$, $g = \sqrt{2}$, $T = 0$, which is the same regime as in Fig. 2(c) of the main text. Here we use Lorentzian broadening with $\eta = 0.05$.

parameter regime: for larger interaction g and for higher T the chain length N can be smaller, while for smaller g and lower T we need larger N. In panels (c) and (d) of Figs. S9 and S10 we see that for intermediate coupling there is some difference in spectral functions for $N = 6$ and $N = 10$ ($N = 8$). At $k = 0$ it is particularly visible in the first satellite structure for $g = 1$. Remarkably, the DMFT on a finite lattice $N = 6$ ($N = 10$) predicts very similar satellite structure as HEOM for the same N. This indicates that the correct satellite peak in Fig. 2(a) of the main text should be closer to DMFT, while HEOM results have some artefacts because of the finite lattice size. On the other hand, for $g = 2$ it is enough to set $N = 4$, as we now demonstrate.

It is very efficient to analyze the finite-size effects using the DMFT applied on a finite system with N sites. This is very simple to implement in the DMFT loop. The only difference is in the self-consistency equation: instead of the integral over the density of states, the local Green function is obtained as an average over the k vectors

$$G(\omega) = \frac{1}{N} \sum_{i=1}^{N} G_{k_i}(\omega). \tag{S24}$$

We can see from Fig. S12 that there is very little difference between $N = 4$, $N = 6$ and thermodynamic limit for $g = 2$, $\omega_0 = 1$. We showed only the results for $T = 0.4$, but we checked that the conclusions remain true even for $T = 0$. Therefore, setting $N = 4$ in HEOM and ED calculations is enough. This left enough computer memory to use large $D = 17$ in HEOM calculations. Then all three methods give very similar spectral functions as seen in Fig. S11.

Fig. S13 shows the DMFT finite-size effects close to the atomic limit, both for the spectral function $A_k(\omega)$ and

FIG. S9.   Finite-N and finite-D effects in the HEOM method at intermediate coupling $\omega_0 = 1$, $g = 1$, $T = 0$, which is the same regime as in Fig. 2(a) of the main text. Here we use Lorentzian broadening with $\eta = 0.05$.

for the self-energy $\Sigma(\omega)$. The spectral functions are not strongly N-dependent. On the other hand, the details of the self-energy are much more sensitive to finite-size effects. Finite N results show a kind of a stripe pattern, while $N = \infty$ results are smoother.
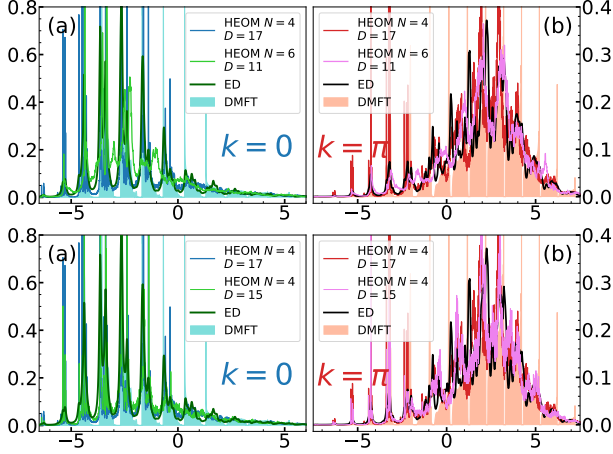

FIG. S11. Finite-N and finite-D effects in the strong coupling regime $\omega_0 = 1$, $g = 2$, $T = 0.4$, which is the same regime as in Figs. 3(e)-(f) of the main text. ED spectral functions ($N = 4$) are shown using Lorentzian broadening with $\eta = 0.05$, while other methods are shown without broadening. DMFT results are in thermodynamic limit.
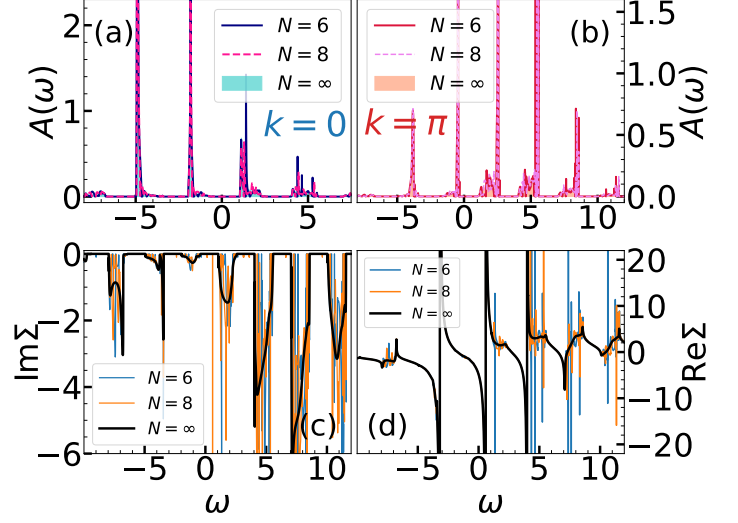

FIG. S13. DMFT finite-size effects close to the atomic limit $\omega_0 = 3$, $g = \sqrt{12}$, $T = 1$

FIG. S12. DMFT spectral functions for different N.

V. ATOMIC LIMIT

Here we investigate the DMFT solution close to the atomic limit. For decoupled sites ($t_0 = 0$), using the Lang-Firsov transformation [S4, S10], the Green's function at $T = 0$ is given by

$$G(\omega) = \sum_{n=0}^{\infty} \frac{\alpha^{2n} e^{-\alpha^2}}{n!} \frac{1}{\omega - n\omega_0 - E_p + i0^+}, \quad \text{(S25a)}$$

and at $T > 0$

$$G(\omega) = \sum_{n=-\infty}^{\infty} \frac{I_n\left(2\alpha^2\sqrt{b(b+1)}\right)}{\omega - n\omega_0 - E_p + i0^+} e^{-(2b+1)\alpha^2 + n\omega_0/2T}.$$
$$\text{(S25b)}$$

Here $E_p = -g^2/\omega_0$ is the ground-state energy, I_n are the modified Bessel functions of the first kind and $b \equiv b(\omega_0) = (e^{\omega_0/T} - 1)^{-1}$. We see that the atomic limit spectrum consists of a series of delta functions at a distance ω_0 from each other. At $T = 0$ the lowest energy peak is at $\omega = E_p$, which corresponds to the ground-state (polaron) energy. At finite temperatures more delta peaks emerge even below the polaron peak.

The integrated DMFT spectral weight at $T = 0$ is shown in Fig. S14 and compared to the exact atomic limit. It was calculated using the numerical procedure introduced in Sec. X. $I(\omega)$ features jumps at frequencies where $A(\omega)$ has peaks and the height of those jumps is equal to the weight of the peaks. Nonzero hopping in the DMFT solution introduces small momentum dependence of $I_k(\omega)$, which is why Fig. S14 shows the result averaged over all momenta. A more detailed comparison is presented in Table S1. It shows the numerical values of the DMFT $I(\omega)$ at the positions of delta peaks (for a given k and averaged over many k) in comparison with the analytical $t_0 = 0$ result from Eq. (S25a). These delta peaks, positioned at $n\omega_0 + E_p$, have the weights equal to $\alpha^{2n} e^{-\alpha^2}/n!$ for $n = 0, 1 \ldots$

For $T > 0$, the peaks are located both below and above E_p. The DMFT spectra averaged over k are shown in Fig. S15. They have a characteristic fork-shaped form at low T, which is the consequence of the 1d density of states. The weight of the peaks are very close to the analytical result $I_n(2\alpha^2\sqrt{b(b+1)})e^{-(2b+1)\alpha^2 + n\omega_0/2T}$. These spectral weights, averaged over momenta k, are given in Table S2.
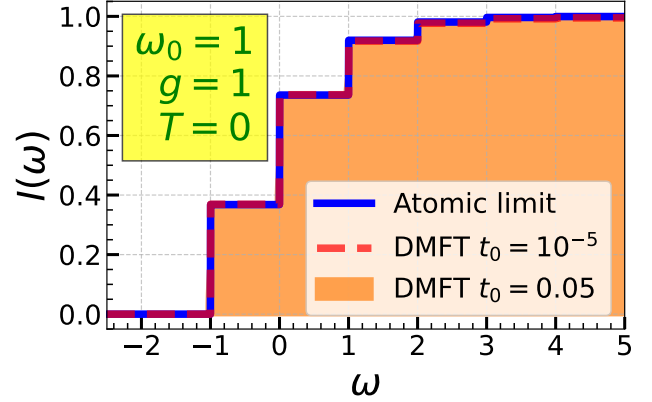

FIG. S14. DMFT integrated spectral weight for $t_0 = 0.05$ (shaded) and $t_0 = 10^{-5}$ (red dashed line) averaged over all momenta, $I(\omega) = \frac{1}{N}\sum_k \int_{-\infty}^{\omega} A_k(\nu)d\nu$, in comparison to the exact $t_0 = 0$ result (blue solid line).

TABLE S1. Integrated spectral weight $I(\omega)$ for $\omega_0 = 1$, $g = 1$ at $T = 0$. The exact atomic limit corresponds to $t_0 = 0.00$. For $t_0 = 10^{-5}$ the DMFT solution has no k-dependence within the specified accuracy. We denote the k-values to be 'av.' if the answer is averaged over all momenta.

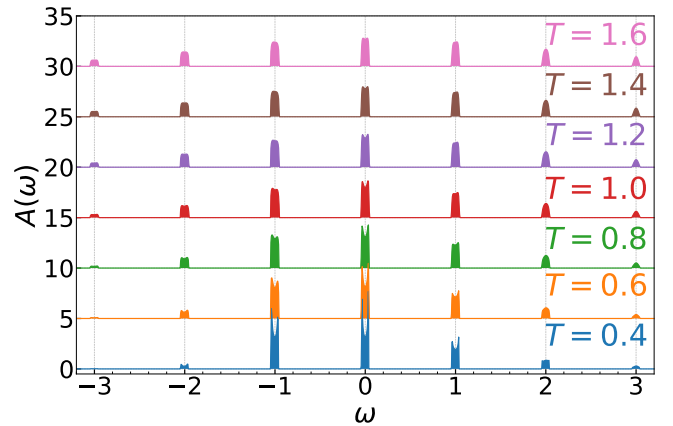| k	t_0	-2	-1	0	1	2	3
	0.00	0.00	0.37	0.74	0.92	0.98	1.0
all	10^{-5}	0.00	0.37	0.74	0.92	0.98	1.0
av.	0.05	0.00	0.37	0.73	0.92	0.98	1.0
0	0.05	0.00	0.40	0.76	0.94	0.99	1.0
$\pi/2$	0.05	0.00	0.37	0.74	0.92	0.98	1.0
π	0.05	0.00	0.33	0.71	0.91	0.98	0.99

FIG. S15. DMFT spectral functions $A(\omega) = \frac{1}{N}\sum_k A_k(\omega)$ for $\omega_0 = 1$, $g = 1$, $t_0 = 0.05$, at several temperatures.

TABLE S2. Spectral weights of the peaks located at $\omega = n\omega_0 + E_p$ for $n = -2, -1, 0, 1, 2, 3$. The DMFT spectra, obtained for $t_0 = 0.05$, are averaged over k. The atomic limit values ($t_0 = 0.00$) are obtained from the analytical formula. Here $\omega_0 = 1$, $g = 1$.

T	t_0 \ ω	−2	−1	0	1	2	3
0.4	0.00	0.03	0.34	0.35	0.19	0.07	0.02
0.4	0.05	0.03	0.34	0.34	0.18	0.07	0.02
0.6	0.00	0.06	0.30	0.33	0.19	0.08	0.02
0.6	0.05	0.06	0.30	0.33	0.19	0.08	0.02
0.8	0.00	0.09	0.27	0.30	0.19	0.09	0.03
0.8	0.05	0.09	0.27	0.30	0.19	0.09	0.03
1.0	0.00	0.10	0.25	0.28	0.19	0.09	0.04
1.0	0.05	0.10	0.25	0.28	0.19	0.10	0.04
1.2	0.00	0.11	0.23	0.26	0.19	0.10	0.04
1.2	0.05	0.11	0.23	0.26	0.19	0.10	0.04
1.4	0.00	0.12	0.21	0.24	0.19	0.11	0.05
1.4	0.05	0.12	0.21	0.24	0.19	0.11	0.05

VI. SPECTRAL FUNCTIONS AT T = 0: ADDITIONAL RESULTS

Spectral functions and integrated spectral weights at $T = 0$ for $k = 0$ are shown in Fig. 2 of the main text. In Figs. S16 - S18, we show the results for additional momenta. We note that the integrated spectral weight was calculated without broadening, using the numerical scheme described in Sec. X. The spectral functions are shown with a small Lorentzian broadening η,

$$A_\eta(\omega) = \frac{1}{\pi} \int_{-\infty}^{\infty} d\nu \frac{\eta A(\nu)}{\eta^2 + (\omega - \nu)^2}, \qquad (S26)$$

We see that there is a very good agreement between DMFT and HEOM/ED results. In every regime where HEOM was implemented, we checked that the results were well converged with respect to the lattice size N and the maximum hierarchy depth D. These values are shown in Table S3.

We note that the HEOM/ED method imposes the periodic boundary conditions on a finite lattice. This means that the HEOM/ED spectral functions are available only for a discrete values of momenta, unlike the DMFT which is calculated in the thermodynamic limit. Results for additional k-values are obtained using twisted boundary conditions.
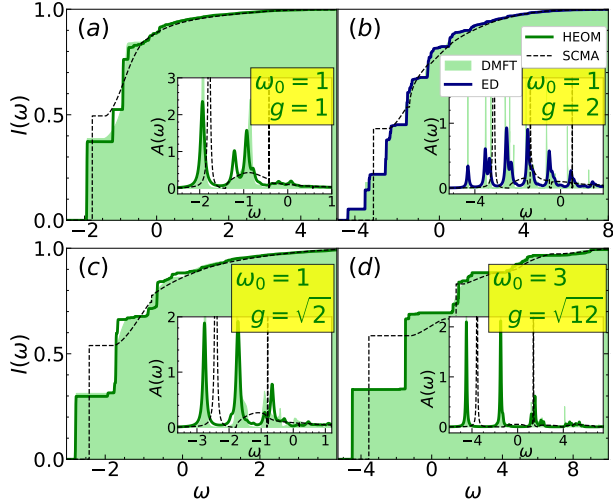

FIG. S16. Integrated spectral weight at $T = 0$ with no broadening. The insets show spectral functions with $\eta = 0.05$ Lorentzian broadening. Different panels have the following values of the momenta: (a) $k = \frac{8\pi}{25}$, (b) $k = \frac{\pi}{4}$, (c) $k = \frac{\pi}{4}$, (d) $k = \frac{\pi}{3}$.
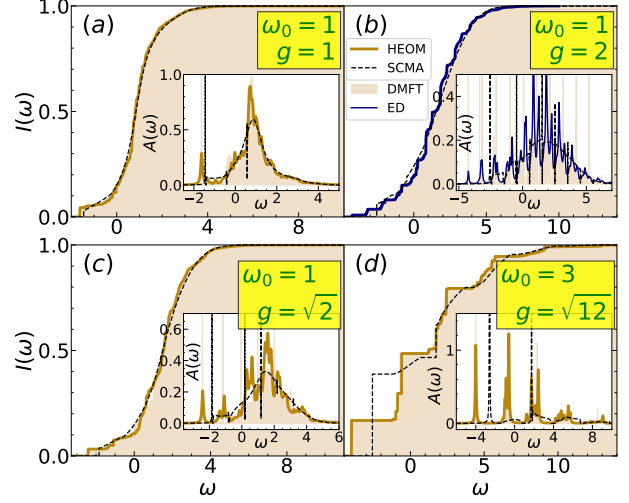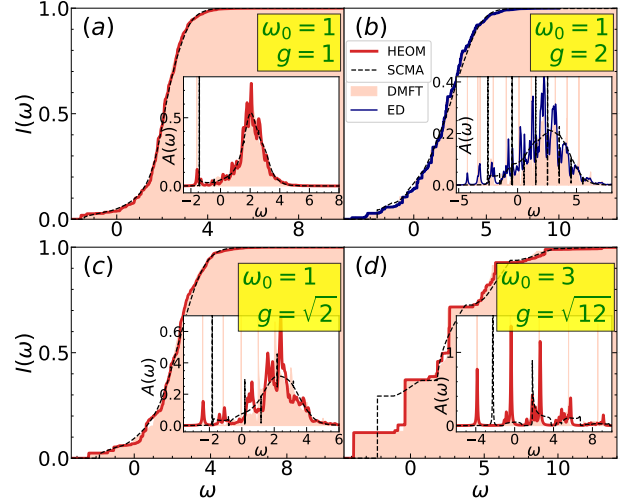

FIG. S17. Integrated spectral weight at $T = 0$ with no broadening. The insets show spectral functions with $\eta = 0.05$ Lorentzian broadening. Different panels have the following values of the momenta: (a) $k = \frac{16\pi}{25}$, (b) $k = \frac{3\pi}{4}$, (c) $k = \frac{3\pi}{4}$, (d) $k = \frac{2\pi}{3}$.

FIG. S18. Integrated spectral weight at $T = 0$ with no broadening. The insets show spectral functions with $\eta = 0.05$ Lorentzian broadening. Every panel is calculated for $k = \pi$.

TABLE S3. Lattice size N and the maximum hierarchy depth D used in the HEOM calculations which correspond to Figs. S16-S18 and Fig. 2 from the main text.

Parameters		N	D
$\omega_0 = 1$	$g = 1$	10	6
$\omega_0 = 1$	$g = \sqrt{2}$	8	7
$\omega_0 = 3$	$g = \sqrt{12}$	6	9

VII. SPECTRAL FUNCTIONS AT T > 0: ADDITIONAL RESULTS

Spectral functions for $k = 0$ and $k = \pi$, shown in Fig. 3 of the main text, are supplemented with the results for different k in Fig. S19. Overall, the agreement of DMFT and HEOM/ED spectra is very good which confirms that the nonlocal correlations are not pronounced. Results for different temperatures are shown in Figs. S20 and S21. We checked that the HEOM results are well converged with respect to lattice size N and maximum hierarchy depth D. The values of N and D, used in the calculations, are shown in Table S4.

TABLE S4. Lattice size N and the maximum hierarchy depth D used in the HEOM calculations which correspond to Figs. S19 - S21 and Fig. 3 from the main text.

Parameters			N	D
$\omega_0 = 1$ $g = 1$	$T = 0.7$		10	6
$\omega_0 = 1$ $g = 1$	$T = 1$		10	6
$\omega_0 = 1$ $g = \sqrt{2}$	$T = 0.4$		8	8
$\omega_0 = 1$ $g = \sqrt{2}$	$T = 0.6$		8	7
$\omega_0 = 1$ $g = \sqrt{2}$	$T = 0.8$		8	7
$\omega_0 = 1$ $g = 2$	$T = 0.4$		4	17
$\omega_0 = 3$ $g = \sqrt{12}$	$T = 1$		6	9

It is common to present the spectral functions as color plots in the $k-\omega$ plane. In Fig. S22 we show the DMFT color plot for parameters as in Figs. S19 - S21. For comparison purposes, in Fig. S23 we also show the DMFT color plot for the same parameters as in the finite-T Lanczos results from Fig. 2 of Ref. [S11]. Small difference in DMFT vs. Lanczos method color plots is due to the more pronounced peaks in the DMFT spectra.
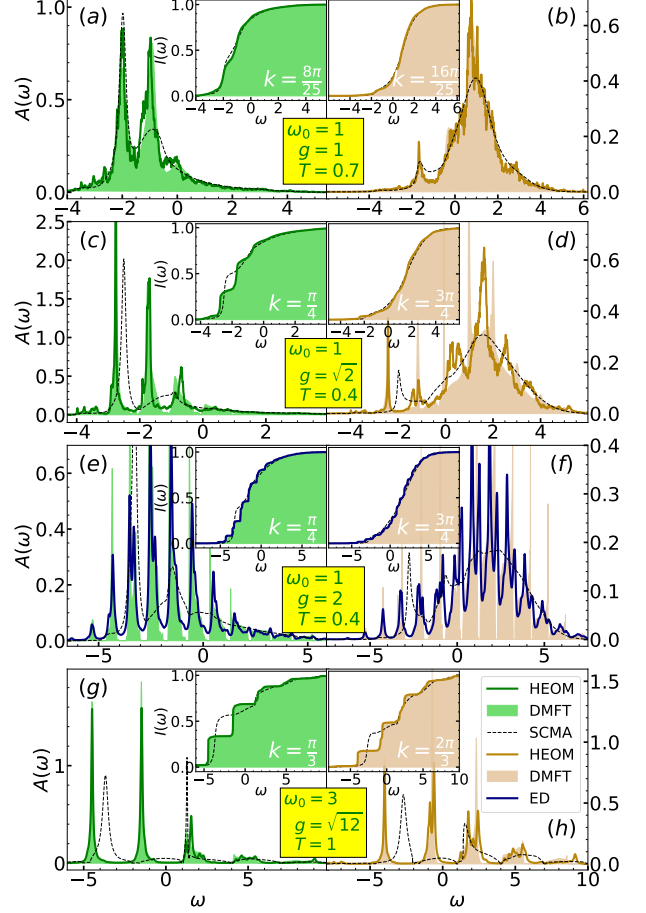

FIG. S19. HEOM, DMFT, SCMA and ED spectral functions for different parameters. On the left panels $\pi/4 \le k \le \pi/3$, whereas $\pi/2 \le k \le 3\pi/4$ on the right. The integrated spectral weight is presented in the insets without broadening. In panels (g) and (h) Lorentzian broadening with $\eta = 0.05$ is used for all spectral functions, while only ED is broadened in (e) and (f) using the same η.
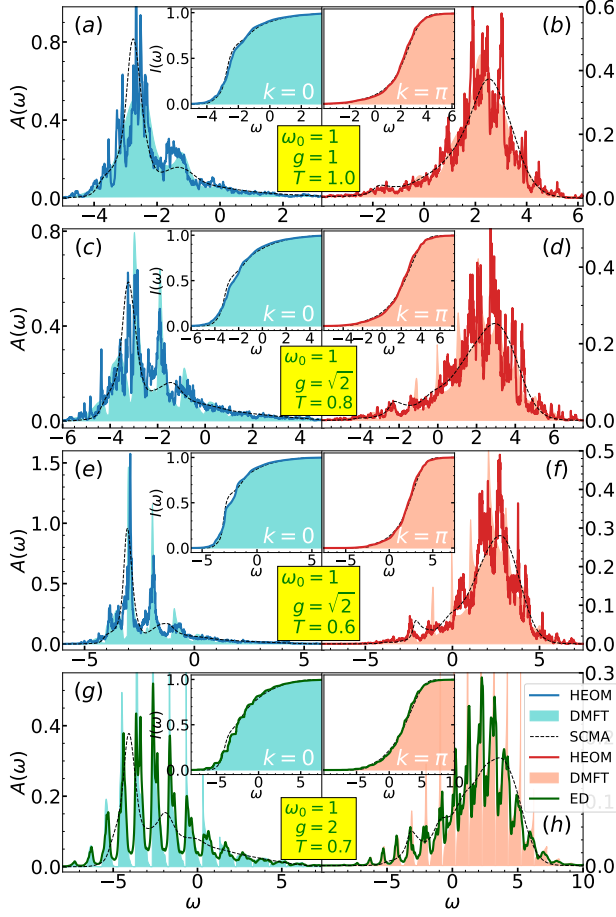
FIG. S20. HEOM, DMFT, SCMA and ED spectral functions for different parameters. On the left panels $k = 0$, whereas $k = \pi$ on the right. The integrated spectral weight is presented in the insets without broadening. The Lorentzian broadening with $\eta = 0.05$ is used only for ED spectral functions.
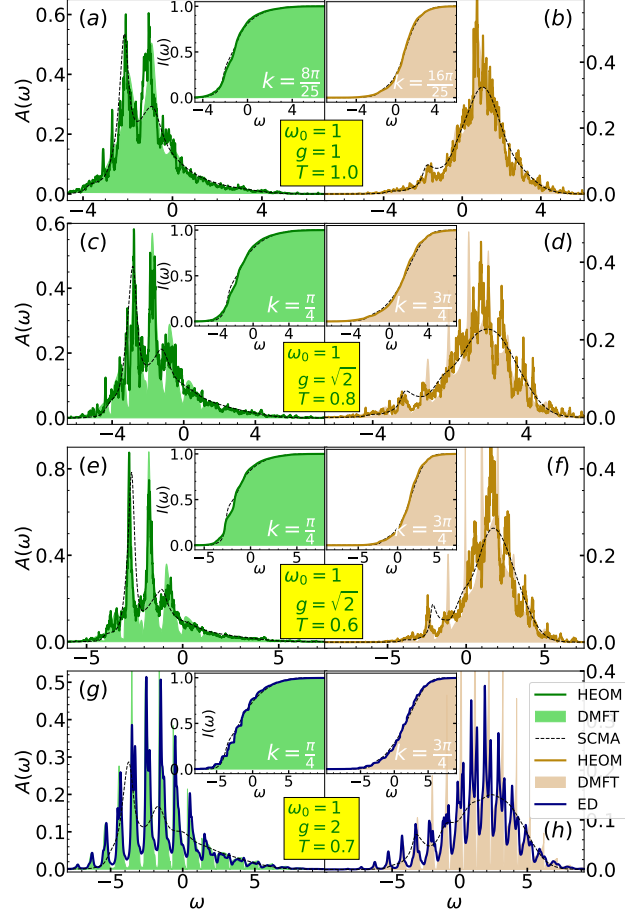
FIG. S21. HEOM, DMFT, SCMA and ED spectral functions for different parameters. On the left panels $\pi/4 \leq k \leq \pi/3$, whereas $\pi/2 \leq k \leq 3\pi/4$ on the right. The integrated spectral weight is presented in the insets without broadening. The Lorentzian broadening with $\eta = 0.05$ is used only for ED spectral functions.
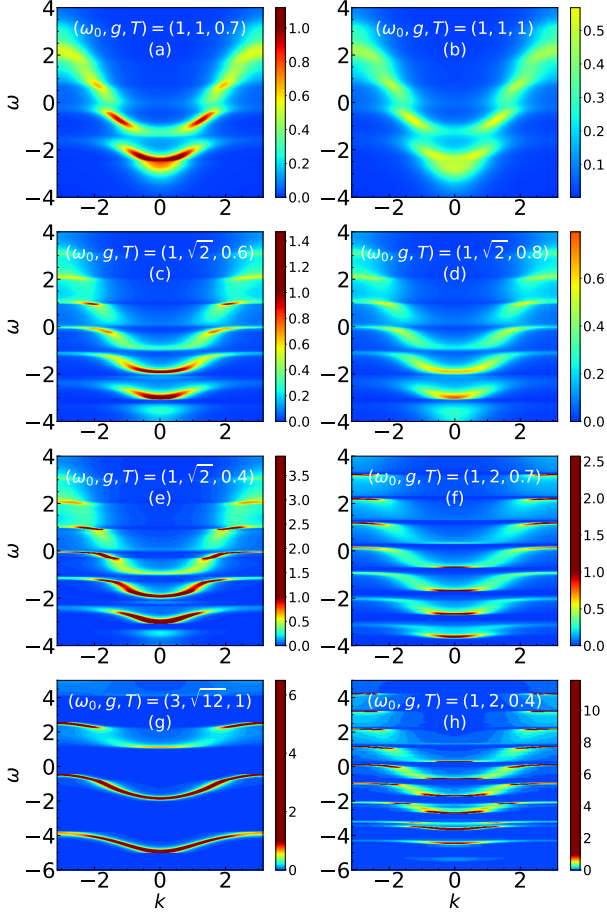
FIG. S22. The DMFT spectral functions $A_k(\omega)$ for parameters as in Figs. S19 - S21. The same color coding is used in all plots.
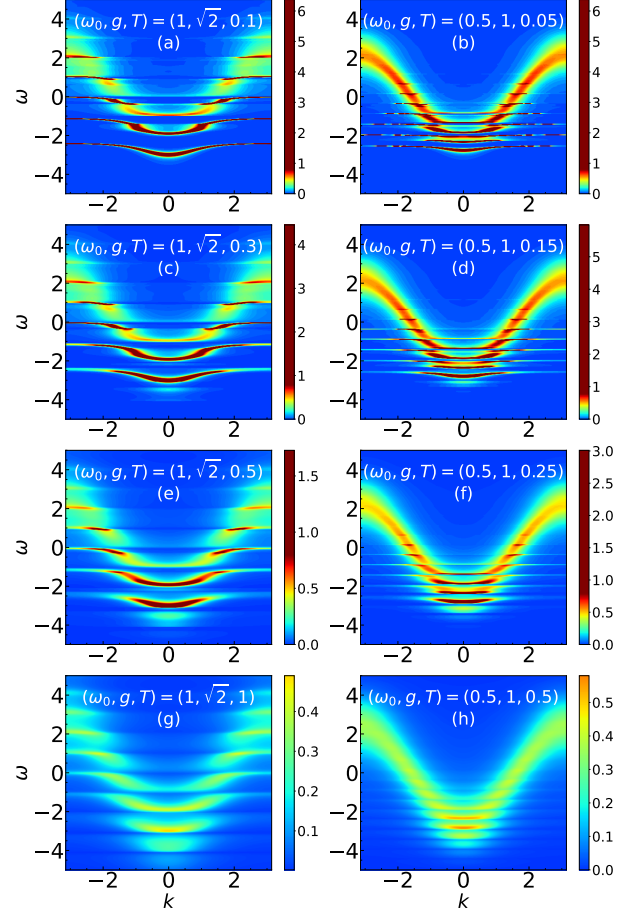
FIG. S23. The DMFT spectral functions $A_k(\omega)$ for parameters as in Fig. 2 of Ref. [S11]. The same color coding is used in all plots.

VIII. HEOM SELF-ENERGIES

The results for the spectral functions, as well as for the effective mass and ground state energy, have shown that the DMFT gives an excellent approximate solution of 1d Holstein model in the whole parameter space. This indicates that the self-energy is approximately local which we explicitly demonstrate in this Section. Since $\Sigma_k(\omega) = \Sigma_{-k}(\omega)$ we will show only the results for $k \geq 0$.

In Fig. S24 we present the HEOM and DMFT self-energies in the intermediate coupling regime. Panels (a) and (b) of Fig. S24 show that the self-energies are nearly local, whereas the DMFT solution interpolates in between. The self-energy is approximately local also for $g = \sqrt{2}$, Fig. S24(c)-(d). There is a visible discrepancy only at higher momenta, which reflects in a shift of the spectral functions with respect to the DMFT solution in Fig. 3d of the main text.

The results for the strong coupling are presented in Fig. S25. The DMFT solution for ImΣ falls to zero between the peaks, as opposed to the HEOM solution where such behavior is observed only for the first few peaks. This is why, for the sake of clarity, the DMFT self-energy is omitted. This is consistent with Fig. S11 where the HEOM results feature the dips, while DMFT solution has gaps. Nevertheless, the presented HEOM results are enough to conclude that the self-energy is nearly local. This is particularly important conclusion since these parameters correspond to strongly renormalized effective mass, $m^*/m \approx 10$.

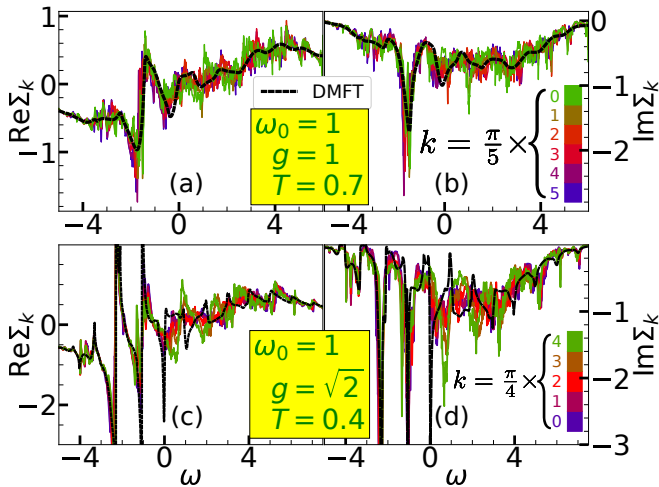The regime close to the atomic limit is investigated in Fig. S26. Panels (c) and (d) show that the results are
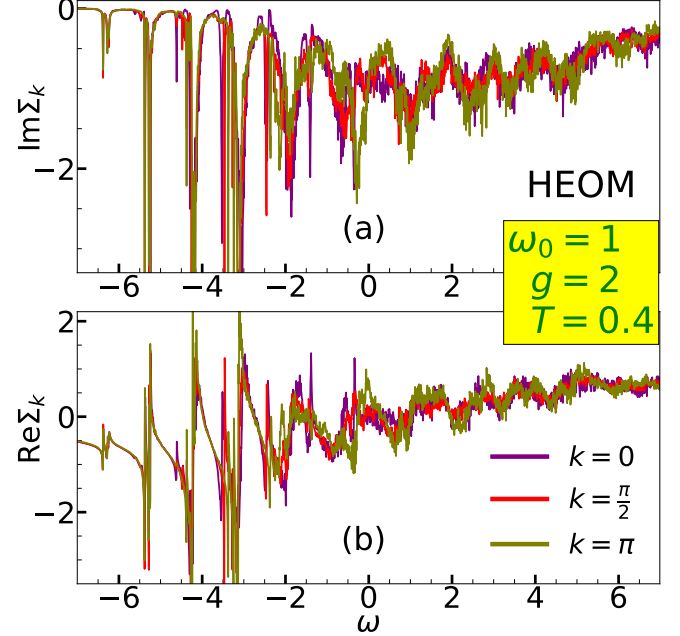

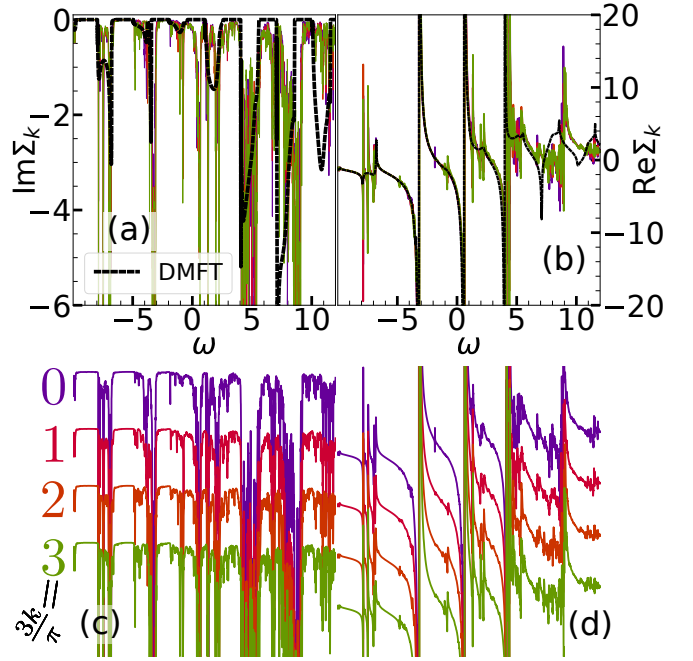FIG. S25. HEOM self-energies for strong coupling. Here $N = 4$ and $D = 17$.

FIG. S26. Panels (a) and (b) show HEOM and DMFT self-energies close to the atomic limit $\omega_0 = 3$, $g = \sqrt{12}$, $T = 1$. Panels (c)-(d) show the same HEOM results as in (a)-(b) but shifted for different values of momenta k.

FIG. S24. HEOM and DMFT self-energies for intermediate coupling.

nearly local, but have a kind of stripe pattern, unlike the DMFT solution which is in thermodynamic limit. This is here just a consequence of the finite-size effects, as

shown in Fig. S13. As discussed in Sec. IV, even though the finite-size effects are visible as stripes in the self-energies, they will not significantly affect the spectral functions. This is why we see a very good agreement between the DMFT and $N = 6$ HEOM spectral functions in panels (g) and (h) of Fig. 3 in the main text.

IX.   CORRELATION FUNCTIONS

Here we present a detailed comparison between QMC, HEOM and DMFT correlation functions. The QMC correlation function is defined by

$$C_k(\tau) = \langle c_k(\tau) c_k^\dagger \rangle_{T,0}, \tag{S27}$$

where $c_k(\tau) = e^{\tau H} c_k e^{-\tau H}$ and $0 \leq \tau \leq 1/T$. In Sec. XI D we proved the following relation

$$C_k(\tau) = \int_{-\infty}^{\infty} d\omega\, e^{-\omega\tau} A_k(\omega). \tag{S28}$$

Eq. (S28) can now be used to check whether the spectral functions that we calculated using other methods are consistent with the QMC results. A calculation of the spectral functions from the QMC data would assume an analytical continuation which is an ill-defined procedure, particularly problematic when the spectrum has several pronounced peaks. Therefore, we have to settle for a comparison on the imaginary axis.

Fig. S27 shows the imaginary time QMC, DMFT and HEOM correlation functions and their deviation from the QMC result, for parameters as in Fig. 4 of the main text. We see that the deviation is very small, the relative discrepancy being just a fraction of a percent at $T = 1$. The discrepancy between the DMFT and QMC increases at lower temperatures when the nonlocal correlations are expected to be more important, but it remains quite small even at $T = 0.4$. As we can see, the DMFT gives better results at $k = 0$ than at $k = \pi$.

In Fig. S28 we present the correlation function comparison over a broad set of parameters. The DMFT, HEOM and QMC are in excellent agreement, with the relative discrepancy of the order of one percent for $\tau \sim 1/T$. The SCMA results are also included for comparison.

From Eq. (S28) we see that the correlation function unevenly treats different frequencies from the spectral function. Because of the exponential term, it takes into account low-frequency contributions with much larger weight. Thus, the correct DMFT and HEOM predictions about correlation function reveal that the low-frequency parts of the corresponding spectral functions behave appropriately and fall off fast enough. This is very important property for calculating quantities where the low-frequency part gives large contribution to the result, which would be the case for optical conductivity.

Let us now estimate how much a Gaussian centered at frequency a,

$$A_k^G(\omega) = \frac{W}{\sigma\sqrt{2\pi}} e^{-\frac{(\omega-a)^2}{2\sigma^2}}, \tag{S29}$$

would contribute to the correlation function. Here W is the spectral weight and σ is the standard deviation
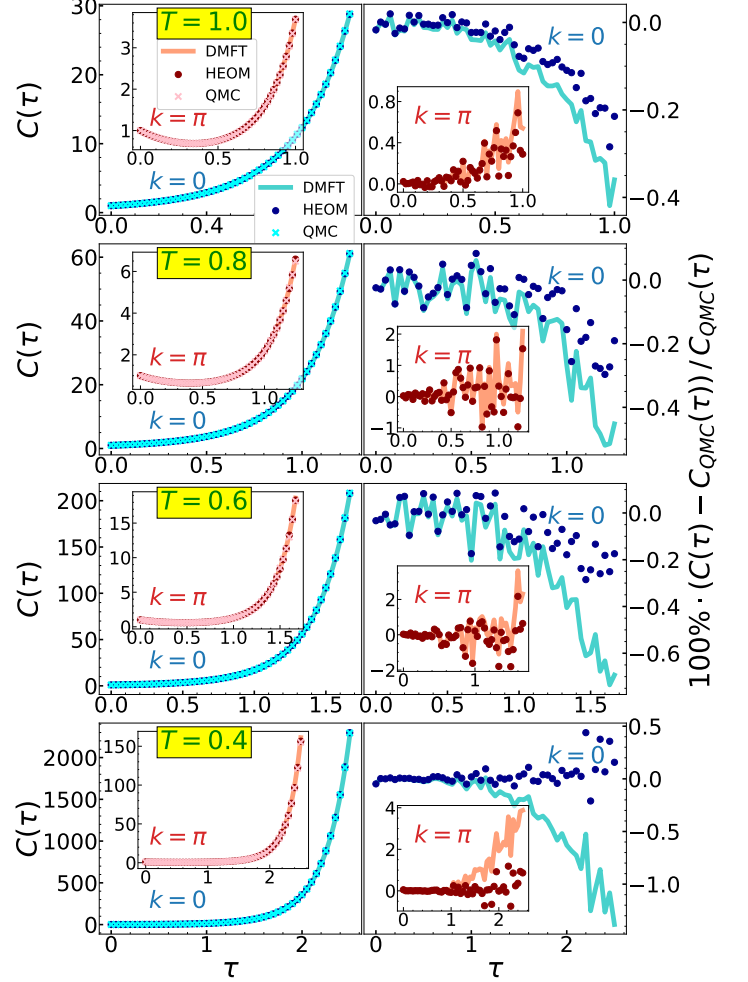

FIG. S27.   DMFT, HEOM and QMC correlation functions for $\omega_0 = 1$, $g = \sqrt{2}$ at $k = 0$ and $k = \pi$ at several temperatures. The right panels show the relative discrepancy between DMFT and HEOM results with respect to QMC.

of the Gaussian. This could model a tiny peak present due to the noise, or a real physical contribution. The corresponding part of the correlation function C_k^G can be singled out since Eq. (S28) is linear in A_k. It can be evaluated analytically, giving

$$C_k^G(\tau) = W e^{\frac{\sigma^2\tau^2}{2} - a\tau}. \tag{S30}$$

We see that the spectral weight contributes linearly, while the position of the delta peak contributes exponentially (note that a can be negative). The width of the Gaussian σ, as well as the imaginary time τ, are quadratic inside the exponential. Hence, Eq. (S30) explicitly shows that precise calculation of the correlation function requires very accurate spectral functions at low frequencies. Even a small error or noise can produce a completely wrong result. Reliable comparison of $C_k(\tau)$

was made possible only due to the high precision of both DMFT and HEOM calculations.
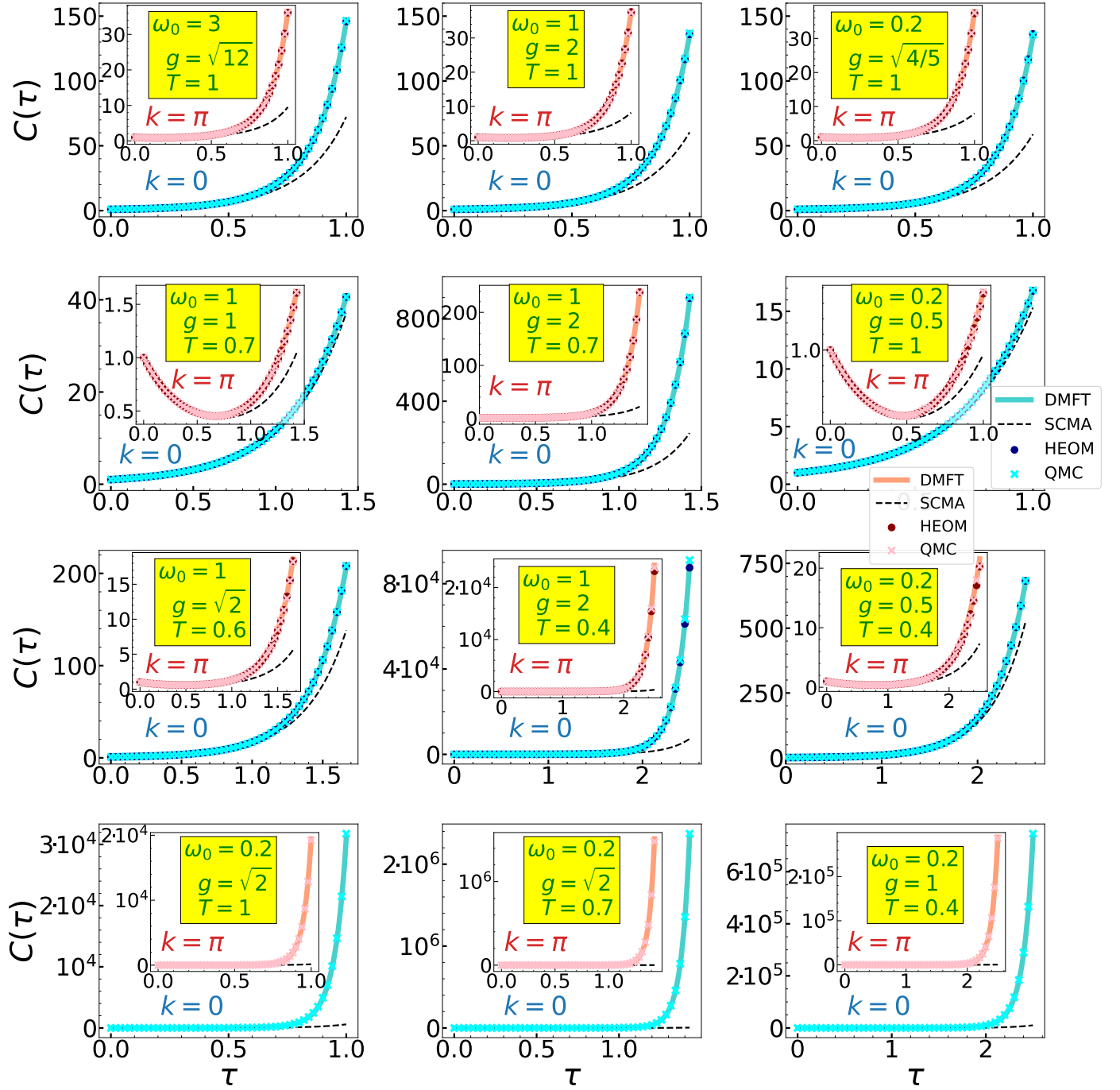
FIG. S28. Comparison of DMFT, HEOM, QMC and SCMA correlation functions over a wide range of parameters. The HEOM results are not available for the parameters in the last row.

X. TECHNICAL NOTE: NUMERICAL CALCULATION OF THE INTEGRATED SPECTRAL WEIGHT

We describe a numerical scheme for calculating the integrated spectral weight. Integrated spectral weight is defined as

$$I_k(\omega) = \int_{-\infty}^{\omega} A_k(\nu) d\nu, \qquad (S31)$$

where $A_k(\nu)$ is the spectral function. Straightforward numerical integration of Eq. (S31) can sometimes lead to the conclusion that the spectral sum rule $I_k(\infty) = 1$ is violated. This happens because the numerical representation of $A_k(\nu)$ on a finite grid does not detect the possible presence of delta function peaks without introducing artificial broadening. This is why our numerical scheme calculates $I_k(\omega)$ directly from the self-energy $\Sigma(\omega)$.

Let us suppose that the self-energy data $\{\Sigma_0, \Sigma_1...\Sigma_{N-1}\}$ are known on a grid $\{\omega_0, \omega_1...\omega_{N-1}\}$. The integrated spectral weight can then be rewritten as

$$I_k(\omega_l) = -\frac{1}{\pi}\mathrm{Im} \int_{-\infty}^{\omega_l} \frac{d\nu}{\nu - \Sigma(\nu) - \varepsilon_k}$$

$$\approx -\frac{1}{\pi}\mathrm{Im} \sum_{q=0}^{l-1} \int_{\omega_q}^{\omega_{q+1}} \frac{d\nu}{\nu - \Sigma(\nu) - \varepsilon_k}. \qquad (S32)$$

The delta peaks in Eq. (S32) occur whenever our subintegral function is (infinitely) close to the singularity, i.e. when $\mathrm{Im}\Sigma(\nu) \to 0^-$ and $\nu - \mathrm{Re}\Sigma(\nu) - \varepsilon_k \approx 0$. These are most easily taken into account by using the linear interpolation of the denominator in Eq. (S32) and evaluating the integral analytically

$$I_k(\omega_l) \approx -\frac{1}{\pi}\mathrm{Im} \sum_{q=0}^{l-1} \int_{\omega_q}^{\omega_{q+1}} \frac{d\nu}{\nu - \varepsilon_k - \left[\Sigma_q + \Sigma_q'(\nu - \omega_q)\right]}$$

$$= -\frac{1}{\pi}\mathrm{Im} \sum_{q=0}^{l-1} \frac{1}{1 - \Sigma_q'} \ln\left[\frac{\omega_{q+1} - \varepsilon_k - \Sigma_{q+1}}{\omega_q - \varepsilon_k - \Sigma_q}\right], \qquad (S33)$$

where $\Sigma_q' = (\Sigma_{q+1} - \Sigma_q)/(\omega_{q+1} - \omega_q)$. In the last line of Eq. (S33) we used that $\ln x - \ln y = \ln(x/y)$, which holds since $\mathrm{Im}\Sigma_q < 0$ (for every q).

In the limit when $\Delta\omega_q = \omega_{q+1} - \omega_q$ is small, Eq. (S33) predicts that the contribution which corresponds to the interval (ω_q, ω_{q+1}) is equal to

$$\frac{1}{1 - \frac{\Sigma_{q+1} - \Sigma_q}{\omega_{q+1} - \omega_q}} \approx \frac{1}{1 - \partial_\omega\Sigma}, \qquad (S34)$$

if the interval contains a delta peak, whereas it is

$$-\frac{1}{\pi}\mathrm{Im}\left[\frac{\Delta\omega_q}{\omega_q - \varepsilon_k - \Sigma_q}\right] \qquad (S35)$$

otherwise. The analytical result for the contribution of the delta peak coincides with Eq. (S34), while Eq. (S35) is exactly the term we would get using the standard Riemann sum. Having in mind that the Riemann sum approach is completely justified in the absence of delta peaks, we conclude that the integration scheme presented in Eq. (S33) is perfectly well-suited for the calculation of the integrated spectral weight.

XI.   TECHNICAL NOTE: EQUIVALENCE OF SPECTRAL FUNCTIONS FROM DIFFERENT DEFINITIONS

Throughout this paper we compared spectral and correlation functions obtained with various methods. Each method uses different definition of the spectral function. The purpose of this Section is to show that all of them are equivalent in the case we are considering, which is a single electron in a system. We also present the relation which connects the spectral function with the imaginary-time correlation function obtained from QMC calculation.

A.   Spectral function from greater Green's function

In the HEOM method, the most natural starting point is the greater Green's function [S12]

$$G_{\mathbf{k}}^{>}(t) = -i \left\langle c_{\mathbf{k}}(t) c_{\mathbf{k}}^{\dagger} \right\rangle_{T,0}. \tag{S36}$$

Here $c_{\mathbf{k}}$ and $c_{\mathbf{k}}^{\dagger}$ are the electron annihilation and creation operators, while

$$c_{\mathbf{k}}(t) = e^{iHt} c_{\mathbf{k}}(0) e^{-iHt}.$$

The notation $\langle \ldots \rangle_{T,0}$ denotes the thermal overage over the space of states containing zero electrons

$$\langle x \rangle_{T,0} = \frac{\sum_p \langle p|e^{-H_{\mathrm{ph}}/T} x|p\rangle}{\sum_p \langle p|e^{-H_{\mathrm{ph}}/T}|p\rangle} = \frac{1}{Z_p} \sum_p \langle p|e^{-H_{\mathrm{ph}}/T} x|p\rangle. \tag{S37}$$

Here $|p\rangle$ denotes the states containing no electrons and arbitrary number of phonons, H_{ph} is purely phononic part of the Hamiltonian and Z_p is the phononic partition function. The spectral function is now defined as

$$A_{\mathbf{k}}(\omega) = -\frac{1}{2\pi} \mathrm{Im} G_{\mathbf{k}}^{>}(\omega), \tag{S38}$$

where

$$G_{\mathbf{k}}^{>}(\omega) = \int_{-\infty}^{\infty} \mathrm{d}t \, e^{i\omega t} G_{\mathbf{k}}^{>}(t). \tag{S39}$$

These expressions can be cast into explicit form using the Lehmann spectral representation (using the basis of energy eigenstates $H|n\rangle = E_n|n\rangle$)

$$G_{\mathbf{k}}^{>}(t) = \frac{-i}{Z_p} \sum_{p,e} e^{-E_p/T} e^{iE_p t} \langle p|c_{\mathbf{k}}|e\rangle \, e^{-iE_e t} \langle e|c_{\mathbf{k}}^{\dagger}|p\rangle, \tag{S40}$$

where $|e\rangle$ denotes the states containing one electron and an arbitrary number of phonons. The spectral function

can now be obtained by taking the Fourier transform of previous expression and using Eq. (S38)

$$A_{\mathbf{k}}(\omega) = \frac{1}{Z_p} \sum_p e^{-E_p/T} \sum_e \delta(\omega + E_p - E_e) |\langle p|c_{\mathbf{k}}|e\rangle|^2. \tag{S41}$$

B.   Spectral function from retarded and time-ordered Green's function

In the DMFT/SCMA, we can start from the time-ordered Green's function [S1] with just a single electron inserted into the system

$$G_{\mathbf{k}}(t) = -i\langle T c_{\mathbf{k}}(t) c_{\mathbf{k}}^{\dagger} \rangle_{T,0}. \tag{S42}$$

As in the case of the greater Green's function, here we average only over the phonon degrees of freedom. This means that (S42) gives nonvanishing contribution only for $t > 0$

$$G_{\mathbf{k}}(t) = -i\theta(t)\langle c_{\mathbf{k}}(t) c_{\mathbf{k}}^{\dagger} \rangle_{T,0}. \tag{S43}$$

In our case of a single electron in the system, this coincides with the retarded Green's function. Ref [S1] explains in detail how is this connected to the polaron impurity problem. Now, the spectral function can be obtained as

$$A_{\mathbf{k}}(\omega) = -\frac{1}{\pi} \mathrm{Im} G_{\mathbf{k}}(\omega), \tag{S44}$$

where

$$G_{\mathbf{k}}(\omega) = \lim_{\varepsilon \to 0^+} \int_{-\infty}^{\infty} \mathrm{d}t \, e^{i(\omega + i\varepsilon)t} G_{\mathbf{k}}(t). \tag{S45}$$

Let us now check whether the definitions of spectral functions from Secs. XI A and XI B are in agreement with one another. This can be easily checked by utilizing the Lehmann spectral representation

$$G_{\mathbf{k}}(t) = \frac{-i\theta(t)}{Z_p} \sum_{p,e} e^{-E_p/T} e^{i(E_p - E_e)t} |\langle p|c_{\mathbf{k}}|e\rangle|^2. \tag{S46}$$

The spectral function is now obtained by performing the Fourier transform, using Eq. (S44) and the Plemelj-Sokhotski theorem $\mathrm{Im} \lim_{\varepsilon \to 0^+} \frac{1}{x + i\varepsilon} = -\pi\delta(x)$. We obtain the result which coincides with (S41). Furthermore, these results also coincide with Eq. (S23). This confirms that all of these approaches are consistent with one another.

C. Spectral function from grand canonical ensemble

It is also quite common to work within the grand canonical ensemble, not restricting ourselves explicitly to a single electron in a system. Here we use the usual definition of the retarded Green's function

$$G_{\mathbf{k}}(t) = -i\theta(t)\left\langle\left\{c_{\mathbf{k}}(t), c_{\mathbf{k}}^\dagger\right\}\right\rangle_T, \qquad (S47)$$

where

$$c_{\mathbf{k}}(t) = e^{iKt}c_{\mathbf{k}}e^{-iKt}, \qquad (S48)$$

$K = H - \mu N$ and N being the electron number operator. The notation $\langle\ldots\rangle_T$ denotes the average value in the grand canonical ensemble and $\{,\}$ is the anticommutator. The spectral function is obtained by substituting $G_{\mathbf{k}}(t)$ from (S47) into Eqs. (S45) and (S44). A more explicit form can be obtained using the Lehmann spectral representation (using the basis of energy eigenstates $K|n\rangle = K_n|n\rangle$)

$$A_{\mathbf{k}}(\omega) = \frac{1}{Z}\sum_{n_1 n_2} e^{-\beta K_{n_1}}\left[|\langle n_1|c_{\mathbf{k}}|n_2\rangle|^2\,\delta(K_{n_1} - K_{n_2} + \omega)\right.$$
$$\left. + \left|\langle n_1|c_{\mathbf{k}}^\dagger|n_2\rangle\right|^2\,\delta(K_{n_2} - K_{n_1} + \omega)\right], \qquad (S49)$$

where $Z = \mathrm{Tr}(e^{-\beta K})$ is the partition function. Let us now consider what happens in the case we are interested in, which is the zero density limit. This corresponds to $\mu \to -\infty$.

We note first that the dominant terms in the partition function Z in this limit are from the states with zero electrons

$$Z = \sum_n e^{-\beta K_n} = \sum_p e^{-\beta K_p} = Z_p. \qquad (S50)$$

The states containing a larger number of electrons introduce an additional term $e^{\beta\mu N}$ which is exponentially small when $\mu \to -\infty$. Consequently, we have shown that Z from Eq. (S49) is the same as Z_p from Eq. (S41) in the limit $\mu \to -\infty$.

Next, we consider the sum in Eq. (S49). Due to the $e^{-\beta K_{n_1}}$ factor, the dominant contribution to the sum over n_1 comes from the states $|n_1\rangle$ containing zero electrons. The states containing a larger number of electrons introduce an additional term $e^{\beta\mu N}$ which is exponentially small when $\mu \to -\infty$. Therefore, the sum over n_1 in Eq. (S49) can be replaced by a sum over p, where $|p\rangle$ denote the states containing no electrons. The second term containing $\langle n_1|c_{\mathbf{k}}^\dagger|n_2\rangle$ in Eq. (S49) is then

zero, while the first term containing $\langle n_1|c_{\mathbf{k}}|n_2\rangle$ is different from zero only when $|n_2\rangle$ is the state containing one electron. The sum in Eq. (S49) then reads as

$$A_{\mathbf{k}}(\omega) = \frac{1}{Z_p}\sum_{p,e} e^{-\beta K_p}\,|\langle p|c_{\mathbf{k}}|e\rangle|^2\,\delta(K_p - K_e + \omega), \qquad (S51)$$

We further note that the last equation can be also expressed in the form

$$A_{\mathbf{k}}(\omega - \mu) = \frac{1}{Z_p}\sum_{p,e} e^{-\beta E_p}\,|\langle p|c_{\mathbf{k}}|e\rangle|^2\,\delta(E_p - E_e + \omega). \qquad (S52)$$

The right hand side in previous equation coincides with Eq. (S41). This proves that the spectral function within the grand canonical formalism needs to be considered in the limit $\mu \to -\infty$ and also the result needs to be shifted $A_{\mathbf{k}}(\omega) \to A_{\mathbf{k}}(\omega - \mu)$ if we want our result to coincide with Eq. (S41).

All of these results give us to flexibility to work within different formalisms knowing that all of them give the same result. Hence, we proved that the definitions of spectral functions within HEOM, DMFT, SCMA and ED are all in agreement.

D. Relation between the spectral function and imaginary-time correlation function

In QMC we calculate the quantity

$$C_{\mathbf{k}}(\tau) = \langle c_{\mathbf{k}}(\tau)c_{\mathbf{k}}^\dagger\rangle_{T,0}, \qquad (S53)$$

where

$$c_{\mathbf{k}}(\tau) = e^{\tau H}c_{\mathbf{k}}e^{-\tau H}. \qquad (S54)$$

Again, using the Lehmann spectral representation in Eq. (S53) we get

$$C_{\mathbf{k}}(\tau) = \frac{1}{Z_p}\sum_{p,e} e^{-\beta E_p}|\langle p|c_{\mathbf{k}}|e\rangle|^2 e^{\tau(E_p - E_e)}. \qquad (S55)$$

By performing straightforward integration, one then finds from Eqs. (S41) and (S55)

$$C_{\mathbf{k}}(\tau) = \int_{-\infty}^{\infty} d\omega\, e^{-\omega\tau} A_{\mathbf{k}}(\omega). \qquad (S56)$$

This proves Eq. (S28), which connects the correlation functions from QMC with spectral functions, obtained from other methods.

[S1] S. Ciuchi, F. de Pasquale, S. Fratini, and D. Feinberg, Phys. Rev. B 56, 4494 (1997).

[S2] A. Georges, G. Kotliar, W. Krauth, and M. J. Rozenberg, Rev. Mod. Phys. **68**, 13 (1996).

[S3] R. M. Martin, L. Reining, and D. M. Ceperley, *Interacting Electrons: Theory and Computational Approaches* (Cambridge University Press, 2016).

[S4] G. Mahan, *Many-Particle Physics* (Kluwer Academic, New York, 2000).

[S5] O. S. Barišić, Phys. Rev. B **76**, 193106 (2007).

[S6] P. E. Kornilovitch, Phys. Rev. Lett. **81**, 5382 (1998).

[S7] A. H. Romero, D. W. Brown, and K. Lindenberg, J. Comp. Phys. **109**, 6540 (1998).

[S8] L.-C. Ku, S. A. Trugman, and J. Bonča, Phys. Rev. B **65**, 174306 (2002).

[S9] A. Migdal, Zh. Eksp. Teor. Fiz. **34**, 1438 (1958), [Sov. Phys. JETP **7**, 996 (1958)].

[S10] I. Lang and Y. A. Firsov, Zh. Eksp. Teor. Fiz. **43**, 1843 (1962), [Sov. Phys. JETP **16**, 1301 (1963)].

[S11] J. Bonča, S. A. Trugman, and M. Berciu, Phys. Rev. B **100**, 094307 (2019).

[S12] V. Janković and N. Vukmirović, Phys. Rev. B **105**, 054311 (2022).

Cumulant expansion in the Holstein model: Spectral functions and mobility

Petar Mitrić ⬤, Veljko Janković ⬤, Nenad Vukmirović ⬤, and Darko Tanasković ⬤

Institute of Physics Belgrade, University of Belgrade, Pregrevica 118, 11080 Belgrade, Serbia

We examine the range of validity of the second-order cumulant expansion (CE) for the calculation of spectral functions, quasiparticle properties, and mobility of the Holstein polaron. We devise an efficient numerical implementation that allows us to make comparisons in a broad interval of temperature, electron-phonon coupling, and phonon frequency. For a benchmark, we use the dynamical mean-field theory which gives, as we have recently shown, rather accurate spectral functions in the whole parameter space, even in low dimensions. We find that in one dimension, the CE resolves well both the quasiparticle and the first satellite peak in a regime of intermediate coupling. At high temperatures, the charge mobility assumes a power law $\mu \propto T^{-2}$ in the limit of weak coupling and $\mu \propto T^{-3/2}$ for stronger coupling. We find that, for stronger coupling, the CE gives slightly better results than the self-consistent Migdal approximation (SCMA), while the one-shot Migdal approximation is appropriate only for a very weak electron-phonon interaction. We also analyze the atomic limit and the spectral sum rules. We derive an analytical expression for the moments in CE and find that they are exact up to the fourth order, as opposed to the SCMA where they are exact to the third order. Finally, we analyze the results in higher dimensions.

I. INTRODUCTION

The cumulant expansion (CE) method presents an alternative to the usual Dyson equation approach in the calculation of spectral functions of interacting quantum many-particle systems [1]. In this method, we express the Green's function in real time as an exponential function of an auxiliary quantity $C(t)$, called the cumulant, which can be calculated perturbatively [2]. In the late 1960s, it was established that the lowest order CE gives the exact solution of the problem of a core hole coupled to bosonic excitations (plasmons or phonons) [3,4]. While there were early papers that emphasized the potential role of CE as an approximate method to treat the electronic correlations in metals beyond the *GW* approximation [5–8] and the electron-phonon interaction in semiconductors and narrow band metals beyond the Migdal approximation (MA) [9–11], a surge of studies of CE has appeared only recently.

Renewed interest has emerged due to the possibility of combining CE with *ab initio* band-structure calculations. The CE for the electron-phonon interaction was used to obtain the spectral functions of several doped transition-metal oxides [12,13], showing a favorable comparison with angle-resolved photoemission spectroscopy [14]. A particularly appealing feature of the CE approach is that it describes the quasiparticle part of the spectrum as well as the satellite structure (sidebands). Combining the CE with the Kubo formula for charge transport gives an attractive route to calculate mobility in semiconductors beyond the Boltzmann approach, which is applicable only for weak electron-phonon coupling [15]. This was very recently demonstrated for SrTiO$_3$ [16] and naphthalene [17]. CE was also applied to elemental metals where a correction to the standard MA is discussed [18]. Similarly, the CE is successfully used to treat the electronic correlations beyond the *GW* approximation [19–25]. Further-

more, CE was used to study absorption spectra in molecular aggregates representative of photosynthetic pigment-protein complexes [26–28].

Despite the wide use of the lowest order CE, there seems to be a lack of studies establishing its range of validity, which represents the central motivation for this paper. To achieve this, we turn to simplified models of the electron-phonon interaction. CE for the Fröhlich model [29,30] gives the ground-state energy and the effective mass similar to the exact quantum Monte Carlo calculations for moderate interaction [31]. This is in contrast to the Dyson-Migdal approach, which severely underestimates mass renormalization. A comparison of the corresponding spectral functions is, however, missing, since reliable quantum Monte Carlo results are not available due to the well-known problems with analytical continuation. The Holstein polaron model gives a unique opportunity to explore the applicability of the CE since various numerically exact methods are developed and applied to this model covering different parameter regimes [32–49]. This was the approach of a very recent work by Reichman and collaborators [50,51]. Still, there are several questions that remained unresolved. Most importantly, a comparison of spectral functions was made just for a small set of parameters on a finite-size lattice, where the benchmark spectral functions were available from the finite-temperature Lanczos results, while the charge transport was not examined.

In our recent work [52], we established that the dynamical mean-field theory (DMFT) [53] gives close to exact spectral functions of the Holstein polaron for different phonon frequencies, electron-phonon couplings, and temperatures even in low dimensions, covering practically the whole parameter space. This method is computationally very fast and precise, which makes us ideally positioned to perform comprehensive comparisons with the CE method, which is the goal of

this paper. Within the CE, we calculate the spectral functions and charge mobility for a broad set of parameters and make detailed comparisons with DMFT and (self-consistent) MA. We find that the one-shot MA is appropriate only for very weak electron-phonon coupling. The validity of the CE and self-consistent Migdal approximation (SCMA) is much broader and for intermediate interaction CE even outperforms SCMA. We also derive analytical CE expressions for the ground-state energy, renormalized mass, and scattering rate as well as the spectral sum rules, and make comparisons between the methods. We establish a power-law behavior for the charge mobility at high temperatures. We also compare the performance of different methods as the bandwidth is reduced toward the atomic limit.

The remaining part of the paper is organized as follows. In Sec. II, we introduce the CE method and present details of its implementation on the Holstein model. DMFT and SCMA are here introduced as benchmark methods. Representative spectral functions are shown in Sec. III from weak toward the strong coupling. The high-temperature and atomic limits are analyzed in detail, as well as the spectral sum rules. In Sec. IV, we present the results for the effective mass and ground-state energy. The temperature dependence of the electron mobility is analyzed in Sec. V, and Sec. VI contains our conclusions. Some details concerning numerical implementations and additional figures for various parameters are shown in the Appendix and in the Supplemental Material (SM) [54].

II. MODEL AND METHODS

The Holstein model is the simplest model of the lattice electrons interacting with the phonons. It assumes a local electron-phonon interaction and dispersionless phonons. The Hamiltonian is given by

$$H = -t_0 \sum_{\langle ij \rangle} (c_i^\dagger c_j + \text{H.c.})$$
$$- g \sum_i n_i (a_i^\dagger + a_i) + \omega_0 \sum_i a_i^\dagger a_i. \quad (1)$$

Here, t_0 is the hopping parameter between the nearest neighbors and ω_0 is the phonon frequency. c_i and a_i are the electron and the phonon annihilation operators, $n_i = c_i^\dagger c_i$, and g denotes the electron-phonon coupling strength. We set $\hbar$, k_B, elementary charge e, and lattice constant to 1. We also often use a parameter $\alpha = g/\omega_0$. We study the model in the thermodynamic limit (number of sites $N \to \infty$). Furthermore, we consider a dynamics of a single electron in the conduction band and treat the electrons as spinless, since we are interested only in weakly doped semiconductors. This is equivalent to setting the chemical potential far below the conduction band, i.e., considering the limit $\tilde{\mu} \to -\infty$. This case is often referred to as the Holstein polaron problem. We mostly focus on the one-dimensional (1D) system, but we also consider the system in 2D and 3D.

A. Cumulant expansion

1. General theory

The central quantity of this paper is the electron spectral function $A_\mathbf{k}(\omega) = (-1/\pi)\text{Im}G_\mathbf{k}(\omega)$, where $\mathbf{k}$ is the momen-

tum and $G_\mathbf{k}(\omega)$ is the retarded Green's function in frequency domain [1]. Its exact evaluation is often a formidable task, which is why approximate techniques are usually employed. One needs to be careful with such approaches not to violate some analytic properties, such as the pole structure of the Green's function, the positivity of the spectral function, or the spectral sum rules. At least some of these properties can be easily satisfied if the Green's function is not calculated directly but instead through some auxiliary quantity, such as the self-energy $\Sigma_\mathbf{k}(\omega)$. In the latter case, the connection with the Green's function is established via the Dyson equation

$$G_\mathbf{k}(\omega) = \frac{1}{G_{\mathbf{k},0}(\omega)^{-1} - \Sigma_\mathbf{k}(\omega)} = \frac{1}{\omega - \varepsilon_\mathbf{k} - \Sigma_\mathbf{k}(\omega)}, \quad (2)$$

where $G_{\mathbf{k},0}(\omega)$ is the noninteracting Green's function and $\varepsilon_\mathbf{k}$ is the noninteracting dispersion relation.

An alternative to the Dyson equation based approaches is the so-called cumulant expansion method [19], in which the exponential ansatz is chosen for the Green's function in the time domain:

$$G_\mathbf{k}(t) = G_{\mathbf{k},0}(t)e^{C_\mathbf{k}(t)} = -i\theta(t)e^{-i\varepsilon_\mathbf{k}t}e^{C_\mathbf{k}(t)}. \quad (3)$$

Here, $\theta(t)$ is the Heaviside step function and $C_\mathbf{k}(t)$ plays the role of an auxiliary quantity which is called the cumulant. Both Eqs. (2) and (3) would correspond to the same Green's function in frequency and time domain if the cumulant $C_\mathbf{k}(t)$ and the self-energy $\Sigma_\mathbf{k}(\omega)$ could be evaluated exactly [1]. In practice, however, one of these approaches is expected to perform better. The spectral function within the CE can be obtained as follows:

$$A_\mathbf{k}(\omega + \varepsilon_\mathbf{k}) = \frac{1}{\pi}\text{Re}\int_0^\infty dt e^{i\omega t}e^{C_\mathbf{k}(t)}. \quad (4)$$

Equation (4) circumvents the Fourier transform of the whole Green's function $A_\mathbf{k}(\omega) = -\frac{1}{\pi}\text{Im}G_\mathbf{k}(\omega)$, which is useful in practice, as the free electron part $e^{-i\varepsilon_\mathbf{k}t}$ typically oscillates much more quickly than $e^{C_\mathbf{k}(t)}$.

The expression for $C_\mathbf{k}(t)$ in the lowest order perturbation expansion can be obtained by taking the leading terms in the Taylor expansion of the Dyson equation $G_\mathbf{k}(\omega) = (G_{\mathbf{k},0}(\omega)^{-1} - \Sigma_\mathbf{k}(\omega))^{-1} \approx G_{\mathbf{k},0}(\omega) + G_{\mathbf{k},0}(\omega)\Sigma_\mathbf{k}(\omega)G_{\mathbf{k},0}(\omega)$, taking its inverse Fourier transform and equating it to Eq. (3), where the cumulant in the exponent is replaced with its linear approximation $e^{C_\mathbf{k}(t)} \approx 1 + C_\mathbf{k}(t)$:

$$C_\mathbf{k}(t) = ie^{i\varepsilon_\mathbf{k}t}\int_{-\infty}^\infty \frac{d\omega}{2\pi}\frac{e^{-i\omega t}\Sigma_\mathbf{k}(\omega)}{(\omega - \varepsilon_\mathbf{k} + i0^+)^2}. \quad (5)$$

Using the spectral representation of the self-energy

$$\Sigma_\mathbf{k}(\omega) = \int \frac{d\nu}{\pi}\frac{|\text{Im}\Sigma_\mathbf{k}(\nu)|}{\omega - \nu + i0^+}, \quad (6)$$

and the contour integration over ω, Eq. (5) simplifies to [19]

$$C_\mathbf{k}(t) = \frac{1}{\pi}\int_{-\infty}^\infty d\omega \frac{|\text{Im}\Sigma_\mathbf{k}(\omega + \varepsilon_\mathbf{k})|}{\omega^2}(e^{-i\omega t} + i\omega t - 1). \quad (7)$$

The corresponding spectral function satisfies the first two sum rules, irrespective of $\Sigma_\mathbf{k}(\omega)$. This is a consequence of the behavior of $C_\mathbf{k}(t)$ for small t; see Sec. III C. In general, $C_\mathbf{k}(t = 0) = 0$ is sufficient for the first spectral sum rule $\int A_\mathbf{k}(\omega)d\omega = 1$ to be satisfied. The second sum rule

$\int A_{\mathbf{k}}(\omega)\omega d\omega = \varepsilon_{\mathbf{k}}$ can also be satisfied if we additionally impose that the cumulant's first derivative at $t = 0$ is vanishing, $\frac{dC_{\mathbf{k}}}{dt}(0) = 0$. Both of these conditions are satisfied by the cumulant function in Eq. (7), as it is a quadratic function of time for small arguments $e^{-i\omega t} + i\omega t - 1 \approx -\omega^2 t^2 / 2$ for $t \to 0$.

The application of Eq. (7) is facilitated by the fact that it does not contain any iterative self-consistent calculations. However, one needs to overcome the numerical challenges caused by the removable singularity at $\omega = 0$ and by the rapidly oscillating trigonometric factor $e^{-i\omega t}$ for large t. The latter is important for the weak electron-phonon couplings, where it is necessary to propagate $C_{\mathbf{k}}(t)$ up to long times until the Green's function is sufficiently damped out. The same problem occurs in other regimes as well (e.g., close to the atomic limit), where the Green's function does not attenuate at all; see Sec. II A 4.

The numerical singularity at $\omega = 0$ can be completely avoided if we consider the cumulant's second derivative

$$\frac{d^2 C_{\mathbf{k}}(t)}{dt^2} = \int_{-\infty}^{\infty} \frac{d\omega}{\pi} \operatorname{Im}\Sigma_{\mathbf{k}}(\omega + \varepsilon_{\mathbf{k}}) e^{-i\omega t} \equiv 2e^{i\varepsilon_{\mathbf{k}} t} \tilde{\sigma}_{\mathbf{k}}(t), \quad (8)$$

where we used $\operatorname{Im}\Sigma_{\mathbf{k}}(\omega) < 0$ and introduced $\tilde{\sigma}_{\mathbf{k}}(t) \equiv \int_{-\infty}^{\infty} \operatorname{Im}\Sigma_{\mathbf{k}}(\omega) e^{-i\omega t} \frac{d\omega}{2\pi}$. Then, $C_{\mathbf{k}}(t)$ is obtained as a double integral over time of Eq. (8),

$$C_{\mathbf{k}}(t) = 2 \int_0^t dt' \int_0^{t'} dt'' e^{i\varepsilon_{\mathbf{k}} t''} \tilde{\sigma}_{\mathbf{k}}(t''), \quad (9)$$

where the lower boundaries of both integrals have to be zero, as guaranteed by the initial conditions $C_{\mathbf{k}}(0) = \frac{dC_{\mathbf{k}}}{dt}(0) = 0$. Using the Cauchy formula for repeated integration, this can also be written as a single integral:

$$C_{\mathbf{k}}(t) = 2 \int_0^t (t - x) e^{i\varepsilon_{\mathbf{k}} x} \tilde{\sigma}_{\mathbf{k}}(x) dx. \quad (10)$$

This completely removed the problem of numerical singularities. Still, the problem of rapid oscillations of the subintegral function remains due to the presence of $e^{i\varepsilon_{\mathbf{k}} x}$ term. In Sec. II A 3, we provide an elegant solution for this issue, focusing on the case of the Holstein model.

2. Asymptotic expansion for cumulant when $t \to \infty$

The asymptotic expansion of $C_{\mathbf{k}}(t)$ for large times, as we now demonstrate, completely determines the quasiparticle properties within this method. This is one of the main motivations for studying the $t \to \infty$ limit. From Eq. (8), we see that

$$\begin{aligned} i\frac{dC_{\mathbf{k}}}{dt}(t \to \infty) &= i \int_0^{\infty} \frac{d^2 C_{\mathbf{k}}(t)}{dt^2} dt \\ &= -\frac{i}{\pi} \int_{-\infty}^{\infty} d\omega |\operatorname{Im}\Sigma_{\mathbf{k}}(\omega + \varepsilon_{\mathbf{k}})| \int_0^{\infty} dt \, e^{-i\omega t} \\ &= \Sigma_{\mathbf{k}}(\varepsilon_{\mathbf{k}}), \end{aligned} \quad (11)$$

where we used the identity $\int_0^{\infty} dt \, e^{-i\omega t} = \pi\delta(\omega) - i\mathcal{P}\frac{1}{\omega}$ and the Kramers-Kronig relations for the self-energy. Hence, the cumulant function $C_{\mathbf{k}}(t)$, and also the whole exponent in Eq. (3) is a linear function of time $C_{\mathbf{k}}(t) - i\varepsilon_{\mathbf{k}} t \approx -i\tilde{E}_{\mathbf{k}} t +$

const for $t \to \infty$, where

$$\tilde{E}_{\mathbf{k}} = \varepsilon_{\mathbf{k}} + \Sigma_{\mathbf{k}}(\varepsilon_{\mathbf{k}}). \quad (12)$$

As a consequence, the Green's function in Fourier space has a simple pole situated at $\tilde{E}_{\mathbf{k}}$, as seen from the following expression:

$$G_{\mathbf{k}}(\omega) = -i \int_0^{\infty} e^{it(\omega - \varepsilon_{\mathbf{k}} - \frac{iC_{\mathbf{k}}(t)}{t})} dt. \quad (13)$$

Therefore, quasiparticle properties are encoded in $\tilde{E}_{\mathbf{k}}$: its real and imaginary parts correspond to the quasiparticle energy and scattering rate, respectively. We note that, in our present analysis, we implicitly assumed that $\frac{dC_{\mathbf{k}}}{dt}(t \to \infty)$ exists and is finite. Although this is generally true, there are a few exceptions. In the Holstein model, the first assumption is violated at the atomic limit [$t_0 = 0$; see Eq. (28)], while the second assumption is violated at the adiabatic limit ($\omega_0 = 0$) for $k = 0$ or $k = \pm\pi$; see Eqs. (18) or (19).

The knowledge that we gained about the analytic properties of the $C_{\mathbf{k}}(t)$ provides us with an intuitive understanding of how the shape of the cumulant determines the shape of the spectral function. The asymptotic limits $t \to \infty$ [where $C_{\mathbf{k}}(t)$ is linear] and $t \to 0$ [where $C_{\mathbf{k}}(t)$ is quadratic] by themselves, to a large extent, describe only the simple one-peak spectral functions, while the crossover between these limits is responsible for the emergence of satellite peaks. This can be explained as follows: If the cumulant was quadratic over the whole t domain $C_{\mathbf{k}}(t) = ct^2$, the spectral function would have a simple Gaussian shape. Similarly, the Lorentzian shape would be obtained from the linear cumulant $C_{\mathbf{k}}(t) = ct$. This suggests that the simple crossover between quadratic (at small t) and linear (at large t) behaviors would also give a simple one-peak shape of the spectral function. The information about phonon satellites is thus completely encoded in the $C_{\mathbf{k}}(t)$ for intermediate times t, which depends on the system and approximation in which the cumulant function is calculated.

3. Second-order cumulant expansion for the Holstein model

Let us now concentrate on a specific example, the Holstein model on a hypercubic lattice in n dimensions. The second-order cumulant is given by Eq. (7), where the self-energy is taken to be in the MA $\Sigma_{\mathbf{k}}(\omega) = \Sigma^{\mathrm{MA}}(\omega)$, i.e., of the second (lowest) order with respect to the electron-phonon coupling g. This is in accordance with the derivation from Sec. II A 1, since we restricted ourselves to the lowest order terms in the Taylor expansion of the Dyson equation and of $e^{C_{\mathbf{k}}(t)}$. An alternative derivation of this expression is given in Sec. I of the SM [54]. MA is briefly discussed in Sec. II B 1. For our present purpose, we only need the expression for the imaginary part of the self-energy

$$\operatorname{Im}\Sigma^{\mathrm{MA}}(\omega) = -\pi g^2 [(n_{\mathrm{ph}} + 1)\rho(\omega - \omega_0) + n_{\mathrm{ph}}\rho(\omega + \omega_0)], \quad (14)$$

where $n_{\mathrm{ph}} = 1/(e^{\omega_0/T} - 1)$ is the Bose factor, $\rho(\omega) = \frac{1}{N}\sum_{\mathbf{k}} \delta(\omega - \varepsilon_{\mathbf{k}})$ is the density of electron states for the system of size N, which we take in the thermodynamic limit $N \to \infty$, and $\varepsilon_{\mathbf{k}} = -2t_0 \sum_{j=1}^n \cos k_j$ is the noninteracting dispersion relation.
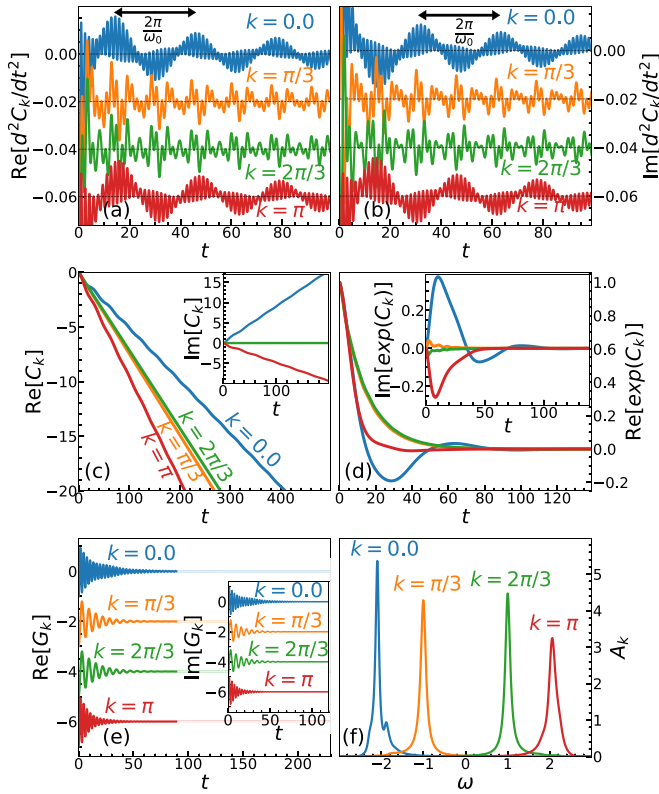
FIG. 1. (a)–(f) The cumulant, Green's, and spectral function on the example of the one-dimensional Holstein model with the following values of the model parameters: $\omega_0 = 0.2$, $g = 0.2$, $T = 0.3$, and $t_0 = 1$.

FIG. 2. Quasiparticle lifetime $\tau_{\mathbf{k}}$ in the CE method for $T/t_0 = 2$ and $g/t_0 = 1$.

The expression for the cumulant function, as seen from Eq. (10), is related to the inverse Fourier transform of $\mathrm{Im}\Sigma^{\mathrm{MA}}(\omega)$, which in turn is completely determined by the inverse Fourier transform of the density of states $\tilde{\rho}(t)$. The latter admits a closed-form solution

$$\tilde{\rho}(t) = \int_{-\infty}^{\infty} \frac{d\omega e^{-i\omega t}}{(2\pi)^{n+1}} \int_{[0,2\pi)^n} d^n\mathbf{k}\, \delta\left(\omega + 2t_0 \sum_{j=1}^{n} \cos k_j\right)$$

$$= \frac{1}{2\pi}\left(\frac{1}{2\pi}\int_0^{2\pi} dk\, e^{2it_0 t \cos k}\right)^n = \frac{J_0(2t_0 t)^n}{2\pi}, \qquad (15)$$

where J_0 is the Bessel function of the first kind of order zero. Hence, Eqs. (10), (14), and (15) imply that the cumulant function can be written as

$$C_{\mathbf{k}}(t) = -g^2 \int_0^t dx(t-x)iD(x)e^{ix\varepsilon_{\mathbf{k}}} J_0(2t_0 x)^n, \qquad (16)$$

where $iD(t) = (n_{\mathrm{ph}}+1)e^{-i\omega_0 t} + n_{\mathrm{ph}}e^{i\omega_0 t}$ is the phonon propagator in real time (for $t > 0$). In Fig. 1, we illustrate the cumulant function, as well as the corresponding Green's function and spectral function. Figures 1(a) and 1(b) show the second derivative of the cumulant

$$\frac{d^2 C_{\mathbf{k}}(t)}{dt^2} = -g^2 iD(t)e^{it\varepsilon_{\mathbf{k}}} J_0(2t_0 t)^n \qquad (17)$$

to demonstrate the rapid oscillations that are also present in the cumulant itself. These are not easily observed by inspect-
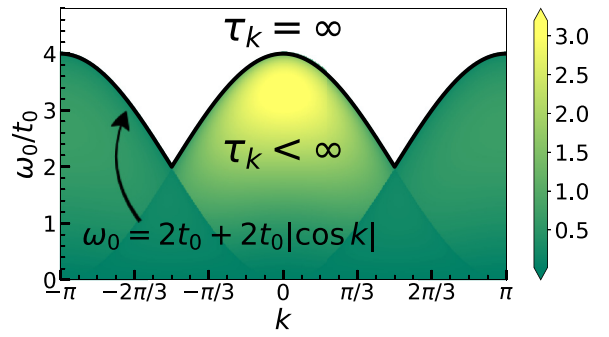
ing $C_{\mathbf{k}}(t)$ directly, as the linear behavior dominates for large times. We observe that the $k = 0$ and $k = \pi$ results possess an oscillating envelope with period $2\pi/\omega_0$, while intermediate momenta have a much less regular structure. This can have direct consequences on the spectral functions, as the satellite peaks are expected to be at a distance ω_0 from each other. To be more explicit, oscillating envelopes suggest that there is a much higher chance for the occurrence of satellite peaks near the bottom ($k \approx 0$) and the top ($k \approx \pi$) of the band, than otherwise. However, that does not guarantee that the satellite peaks will in fact occur. Figure 1(c) shows that $\mathrm{Re}C_{\mathbf{k}}(t)$ is declining faster for $k > 0$ than for $k = 0$. As a consequence, $e^{C_{\mathbf{k}}(t)}$ in Fig. 1(d) attenuates slower for $k = 0$, having enough time to complete a full period, while $k = \pi$ results are reminiscent of an overdamped oscillator. A similar, although much less evident, effect can be seen in the Green's function itself; see Fig. 1(e). This is why the $k = \pi$ spectral function in Fig. 1(f) has a simple one-peak shape, while only the $k = 0$ result captures one small satellite peak.

From a numerical point of view, Eq. (16) is treated using Levin's collocation method [55], which is reviewed in Appendix A. It provides a controlled, accurate, and numerically efficient way to integrate the product of trigonometric, Bessel, and some slowly varying function. This approach avoids using a dense t grid, which would otherwise be required, as the subintegral function in Eq. (16) has the same type of rapid oscillations present in $d^2 C_{\mathbf{k}}(t)/dt^2$.

4. Lifetime

Another question of practical importance is how long we should propagate the cumulant function in real time until the corresponding Green's function attenuates. A rough estimate of such quantity is given by the quasiparticle lifetime $\tau_{\mathbf{k}}$. The lifetime is given by $\tau_{\mathbf{k}} = 1/(2|\mathrm{Im}\tilde{E}_{\mathbf{k}}|)$, where $\tilde{E}_{\mathbf{k}}$ is given by Eq. (12) and the self-energy is taken in the MA [see Eq. (14)]:

$$\tau_{\mathbf{k}}^{-1} = 2|\mathrm{Im}\tilde{E}_{\mathbf{k}}| = 2g^2 \frac{\theta\left(4t_0^2 - (\varepsilon_{\mathbf{k}} - \omega_0)^2\right)}{\sqrt{4t_0^2 - (\varepsilon_{\mathbf{k}} - \omega_0)^2}}(n_{\mathrm{ph}}+1)$$

$$+ 2g^2 \frac{\theta\left(4t_0^2 - (\varepsilon_{\mathbf{k}} + \omega_0)^2\right)}{\sqrt{4t_0^2 - (\varepsilon_{\mathbf{k}} + \omega_0)^2}}n_{\mathrm{ph}}. \qquad (18)$$

This is illustrated in Fig. 2. We observe that there is a considerable part of the parameter space where the lifetime is
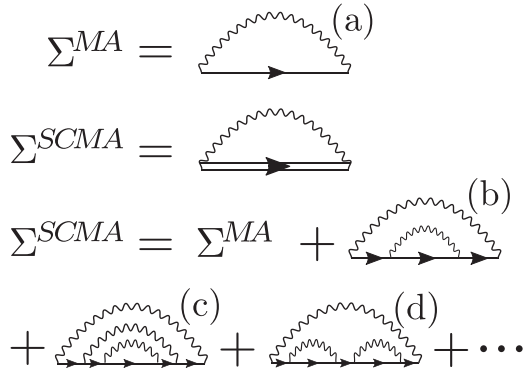
FIG. 3. Feynman diagrams in the Migdal approximation and the self-consistent Migdal approximation.

infinite, which means that the corresponding Green's function never attenuates. This occurs for $\omega_0 > 2t_0 + 2t_0|\cos k|$ in the case of finite temperatures, and for $\omega_0 > 4t_0 \sin^2 k/2$ in the $T = 0$ case. In these regimes, one could presume that this is reflected in the spectral functions through the appearance of Dirac delta peaks, which is not expected at finite temperatures. This illustrates one of the limitations of this method.

B. Benchmark methods

1. Migdal and self-consistent Migdal approximation

The Migdal approximation [56] is the simplest perturbation approach, whose self-energy is represented with a single, lowest order Feynman diagram, as shown in Fig. 3(a). The imaginary part of the self-energy is given by Eq. (14) in the case when there is just a single electron in the band, regardless of the dispersion relation or the number of dimensions of the system. The corresponding real part is obtained using the Kramers-Kronig relations, and in 1D reads as

$$
\begin{aligned}
\mathrm{Re}\,\Sigma^{\mathrm{MA}}(\omega) = {} & g^2(n_{\mathrm{ph}} + 1) \frac{\theta\big((\omega - \omega_0)^2 - 4t_0^2\big)\mathrm{sgn}(\omega - \omega_0)}{\sqrt{(\omega - \omega_0)^2 - 4t_0^2}} \\
& + g^2 n_{\mathrm{ph}} \frac{\theta\big((\omega + \omega_0)^2 - 4t_0^2\big)\mathrm{sgn}(\omega + \omega_0)}{\sqrt{(\omega + \omega_0)^2 - 4t_0^2}}.
\end{aligned}
\tag{19}
$$

The range of validity of the MA can be extended if we substitute the noninteracting electron propagator in Fig. 3(a) with an interacting one. At the same time, the interacting propagator itself is expressed through the self-energy via the Dyson equation. These relations constitute the SCMA. Figure 3 illustrates that the SCMA self-energy consists of a series of noncrossing diagrams, whose lowest order coincides with the MA. Figure 3(b) shows the second-order contribution, while the third-order contributions are shown in Figs. 3(c) and 3(d).

Mathematically, the self-consistency relations are straightforwardly derived and, in our case, read as

$$
\Sigma^{\mathrm{SCMA}}(\omega) = g^2(n_{\mathrm{ph}} + 1)G(\omega - \omega_0) + g^2 n_{\mathrm{ph}} G(\omega + \omega_0),
\tag{20a}
$$

$$
G(\omega) = \frac{1}{(2\pi)^n} \int_{-\pi}^{\pi} d^n\mathbf{k} \frac{1}{\omega - \varepsilon_{\mathbf{k}} - \Sigma^{\mathrm{SCMA}}(\omega)}, \tag{20b}
$$

where $G(\omega)$ is the local Green's function. We see that in the case of the Holstein model, the SCMA self-energy is $\mathbf{k}$ independent.

2. Dynamical mean-field theory

Dynamical mean-field theory is a nonperturbative approximate method, that represents a natural generalization of the traditional mean-field theory [57]. It simplifies the original lattice problem by mapping it to a single site impurity problem, embedded into an external bath that is described with a frequency-dependent (i.e., dynamical) field $G_0(\omega)$, which needs to be determined self-consistently. This simplification is reflected on the self-energy, which is assumed to be $\mathbf{k}$-independent $\Sigma_{\mathbf{k}}(\omega) = \Sigma(\omega)$. The DMFT becomes exact in the limit of infinite dimensions or, equivalently, infinite coordination number.

In practice, $G_0(\omega)$ and $\Sigma(\omega)$ are determined self-consistently, by imposing that the local Green's function of the lattice problem

$$
G(\omega) = \int_{-\infty}^{\infty} \frac{\rho(\epsilon)d\epsilon}{\omega - \Sigma(\omega) - \epsilon}, \tag{21}
$$

and the self-energy $\Sigma(\omega)$ coincide with the corresponding quantities of the impurity problem. Here, $\rho(\epsilon)$ is the noninteracting density of states. The self-consistent loop is closed using the Dyson equation $G_0(\omega) = (G^{-1}(\omega) + \Sigma(\omega))^{-1}$. In the case of the Holstein model, the (polaron) impurity problem can be solved exactly, directly on the real-frequency axis, in terms of the continued fraction expansion [53]. Furthermore, in the one-dimensional case, Eq. (21) assumes a closed-form solution and reads as

$$
G(\omega) = \mathrm{Re}\,\frac{1}{2t_0 B(\omega)\sqrt{1 - \frac{1}{B(\omega)^2}}} + i\mathrm{Im}\,\frac{-i}{2t_0\sqrt{1 - B(\omega)^2}}, \tag{22}
$$

where $B(\omega) = (\omega - \Sigma(\omega))/(2t_0)$; see Supplemental Material of Ref. [52]. We note that Eq. (22) can also be used for the SCMA in Eq. (20).

We have very recently shown [52], by using extensive comparisons with several numerically exact methods covering various parameter regimes, that the DMFT can provide a rather accurate solution for the Holstein polaron even in low dimension. Hence, the DMFT has emerged as a unique numerical method that gives close to exact spectral functions in practically the whole space of parameters, irrespective of the number of dimensions. This makes the DMFT an ideal benchmark method for comparisons with the CE results for the Holstein model.

III. SPECTRAL FUNCTIONS

In this section, we present the CE spectral functions of the 1D Holstein model. The DMFT is used as a benchmark, while MA and SCMA represent the main competitors and alternatives to the CE method. Section III A shows the results for $k = 0$, whereas heat plots and the $k = \pi$ results are shown in Sec. III B. High-temperature spectral functions and spectral sum rules are presented in Sec. III C. The behavior near the atomic limit is discussed in Sec. III D. We present only
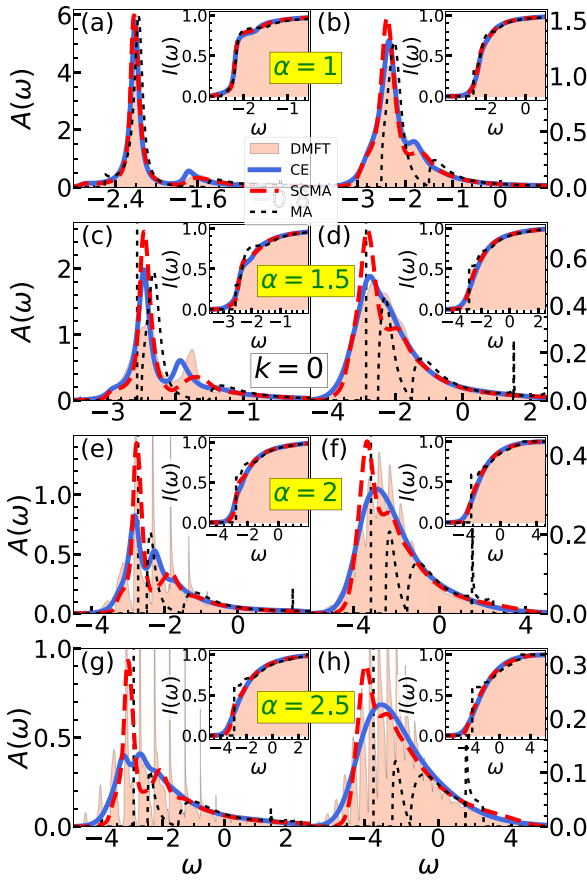
FIG. 4. (a)–(h) Spectral functions for $t_0 = 1$, $\omega_0 = 0.5$ and $k = 0$. In the left panels $T = 0.3$, while $T = 0.7$ in the right panels. Insets show the integrated spectral weights $I_{\mathbf{k}}(\omega) = \int_{-\infty}^{\omega} A_{\mathbf{k}}(\nu) d\nu$.
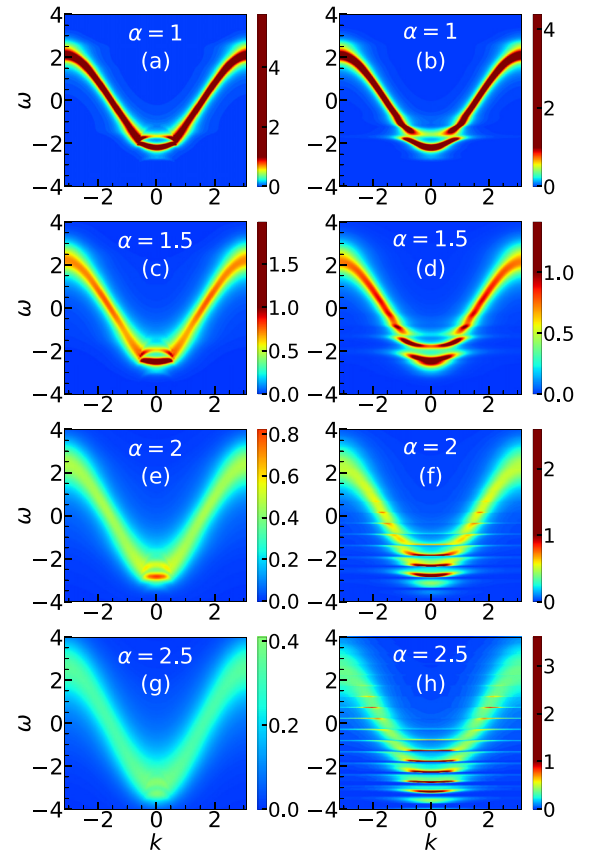

FIG. 5. (a)–(h) Heat maps of $A_{\mathbf{k}}(\omega)$ for $t_0 = 1$, $\omega_0 = 0.5$, and $T = 0.3$. In the left panels, we present CE results, while the DMFT benchmark is presented in the right panel. All plots use the same color coding.

the results for $\omega_0 = 0.5$, while the results for other phonon frequencies and various momenta are shown in Sec. II of SM [54]. The 2D spectral functions are presented in Appendix B.

A. Low and intermediate temperatures for $k = 0$

In the weak-coupling limit $\alpha \to 0$, all these approximate methods (DMFT, CE, SCMA, MA) provide accurate results. In Fig. 4, we investigate how far from this strict limit each of our methods continues to give reasonably accurate spectral functions. In Fig. 4(a), we see that for $\alpha = 1$ all methods correctly capture the quasiparticle peak, which dominates in the structure of the spectrum. The MA satellite peak is slightly shifted towards higher frequencies, which becomes significantly more pronounced at higher temperatures; see Fig. 4(b). The limitations of the MA become more obvious for stronger couplings, where even the position and weight of the quasiparticle peak are inaccurate; see Figs. 4(c)–4(h).

While the quasiparticle properties of the CE and SCMA seem to be quite similar if α is not too large, some difference in satellite peaks is already visible in Figs. 4(b) and 4(c). Figure 4(c) shows that SCMA gives broader satellites than the DMFT benchmark, whereas CE slightly underestimates the position of the satellite. Neither CE nor SCMA can be characterized as distinctly better in this regime. On the other hand, Figs. 4(e) and 4(g) display a clear advantage of the CE.

We see that it captures rather well the most distinctive features of the solutions, which are the first few satellites. This is not the case for SCMA.

Figures 4(f) and 4(h) demonstrate that the CE gives a rather quick crossover toward the high-temperature limit, as it predicts a simple broad one-peak structure for the spectral function already for $T = 0.7$. This large difference between the spectral functions for $T_1 = 0.3$ and $T_2 = 0.7$ can be understood by examining the ratio of their corresponding lifetimes $\tau(T_1)/\tau(T_2) = n_{\mathrm{ph}}(T_2)/n_{\mathrm{ph}}(T_1) \approx 8.5$. This implies that $\mathrm{Re}C_{\mathbf{k}}(t)$ for $T = 0.7$ has a much steeper slope as a function time, which suppresses the appearance of satellites, as explained in Sec. II A 3.

B. Low and intermediate temperatures for $k \neq 0$

To proceed with the analysis of the CE ,we want to answer: (i) Whether the conclusions that we reached for $k = 0$ can be carried over to other momenta as well? (ii) Does CE continue to be better than SCMA at much higher temperatures? The first question is answered in Fig. 5, where we compare CE and DMFT heat plots. Figures 5(a) and 5(b) demonstrate that CE results are quite reminiscent of the DMFT results for $\alpha = 1$, even at nonzero momenta. The same conclusion holds for weaker couplings as well. On the other hand, there are differences between the results for somewhat stronger
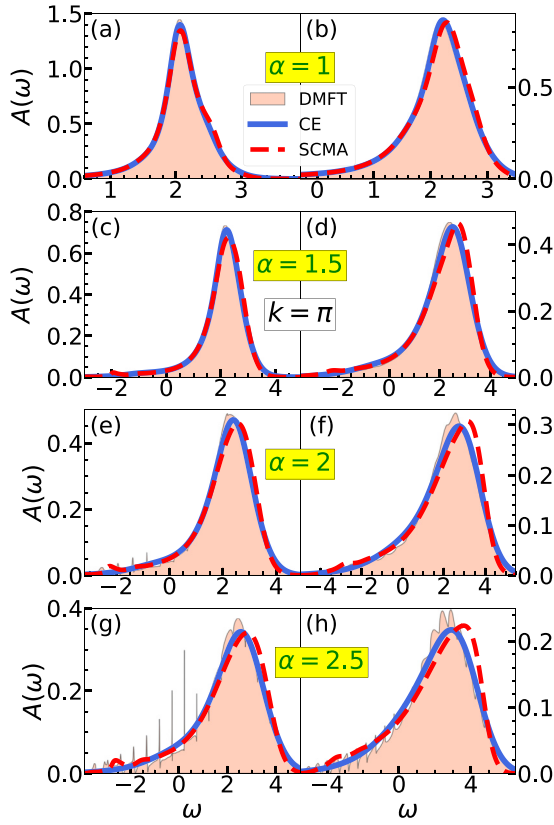
FIG. 6. (a)–(h) Spectral functions for $t_0 = 1$, $\omega_0 = 0.5$, and $k = \pi$. In the left panels $T = 0.3$, while $T = 0.7$ in the right panels.

coupling $\alpha = 1.5$, as shown in Figs. 5(c) and 5(d). While the polaron bands in both of these figures are convex, the CE predicts the first satellite to be concave, unlike the DMFT. In other words, CE predicts that the distance between the polaron peak and the satellites decreases as we increase the momentum. This is counterintuitive, as the satellites are perceived as the quasiparticle that absorbed or emitted a phonon, which should consequently be just at energy distance ω_0 apart. These limitations of the CE are much more pronounced for stronger electron-phonon couplings. While the DMFT solution in Figs. 5(f) and 5(h) exhibits a series of distinct bands, Figs. 5(e) and 5(g) demonstrate that the polaron and satellite bands of the CE merge into a single band at higher momenta. However, the most noticeable feature here is the fact that the CE is too smeared, as if the temperature is too high. This is a consequence of the fact that the lifetime in Eq. (18) scales as $\tau_{\mathbf{k}} \sim 1/g^2$. While the heat maps reveal noticeable discrepancies between the DMFT and CE for $k \neq 0$, it seems that these differences are much less pronounced around $k = \pi$. A more detailed comparison is presented in Fig. 6 that shows the results for the same regimes as in Fig. 4. The DMFT solution in Figs. 6(a)–6(d) shows that the main feature of the spectral function is a single broad peak for $\alpha \lesssim 1.5$, which is in agreement with the CE results. This is also the case for the SCMA, although we observe a slight tendency of the main peak to lean toward higher frequencies at higher temperatures. For larger interaction strengths, CE cannot fully reproduce the sharp peaks at lower frequencies of the low-temperature spectral function or the fine structure of the main peak at higher

temperatures; see Figs. 4(e)–4(h). Similarly, CE misses the quasiparticle peak as well, situated at low energy, although it is typically tiny and not (clearly) visible in Figs. 6(a)–6(h) (see Appendix C). A detailed comparison of the spectral functions for other momenta and phonon frequencies is presented in Sec. II of the SM [54].

Overall, we find that the CE gives the most accurate results for $k = 0$ and $k = \pi$ and that it is less accurate for other momenta. Although it cannot fully reproduce a tiny quasiparticle peak for $k = \pi$, it describes well a wide single-peak structure, which is the most prominent feature of the spectrum. A much larger discrepancy for $k = \pi$, between the CE and a reliable benchmark, was reported in Ref. [50] by examining the system on a finite lattice system with $N = 6$. In Appendix C, we examine the same parameter regime as in Ref. [50] and show that these discrepancies are significantly reduced in the thermodynamic limit.

C. Spectral functions at high temperatures and spectral sum rules

In Fig. 7, we show CE, SCMA, and DMFT spectral functions at high temperatures for the same electron-phonon couplings as in Figs. 4 and 6. We see that CE performs very well both for $k = 0$ and $k = \pi$. There are only small discrepancies at stronger interactions [see, e.g., Fig. 7(c)]. In contrast, the SCMA solution gets tilted relative to the DMFT and CE. In addition, it poorly reproduces the low-frequency part of the spectrum. It is not obvious whether the CE method is exact in the high-temperature limit $T \to \infty$. As we now demonstrate, this can be answered by examining the spectral sum rules:

$$\mathcal{M}_n(\mathbf{k}) = \int_{-\infty}^{\infty} A_{\mathbf{k}}(\omega)\omega^n d\omega. \tag{23}$$

These can be calculated both exactly,

$$\mathcal{M}_n^{\text{exact}}(\mathbf{k}) = \left\langle \underbrace{[\ldots[[c_{\mathbf{k}}, H], H]\ldots, H]}_{n \text{ times}} c_{\mathbf{k}}^{\dagger} \right\rangle_T, \tag{24}$$

and within the CE approximation, where by combining Eqs. (4) and (23) we find

$$\mathcal{M}_n^{\text{CE}}(\mathbf{k}) = \text{Re}\left[i^n \left(\frac{d}{dt}\right)^n e^{C_{\mathbf{k}}(t)}\right]\bigg|_{t=0}$$
$$- \sum_{p=1}^{n} \binom{n}{p}(-\varepsilon_{\mathbf{k}})^p \mathcal{M}_{n-p}^{\text{CE}}(\mathbf{k}). \tag{25}$$

The difference between these quantities $\mathcal{M}_n^{\text{CE}}(\mathbf{k}) - \mathcal{M}_n^{\text{exact}}(\mathbf{k})$ is zero for $n = 0$ and $n = 1$, as noted in Sec. II A 1. Higher order sum rules for the CE method are easily calculated, while the evaluation of the exact sum rules quickly becomes cumbersome for increasing n. The first five ($0 \leqslant n \leqslant 4$) sum rules were already calculated by Kornilovitch [58]

$$\mathcal{M}_2(\mathbf{k}) = \varepsilon_{\mathbf{k}}^2 + (2n_{\text{ph}} + 1)g^2, \tag{26a}$$

$$\mathcal{M}_3(\mathbf{k}) = \varepsilon_{\mathbf{k}}^3 + g^2\omega_0 + 2g^2(2n_{\text{ph}} + 1)\varepsilon_{\mathbf{k}}, \tag{26b}$$

$$\mathcal{M}_4(\mathbf{k}) = \varepsilon_{\mathbf{k}}^4 + 2g^2\varepsilon_{\mathbf{k}}\omega_0 + g^2(2n_{\text{ph}} + 1)$$
$$\times \left(2t_0^2 + 3\varepsilon_{\mathbf{k}}^2 + \omega_0^2\right) + 3g^4(2n_{\text{ph}} + 1)^2. \tag{26c}$$
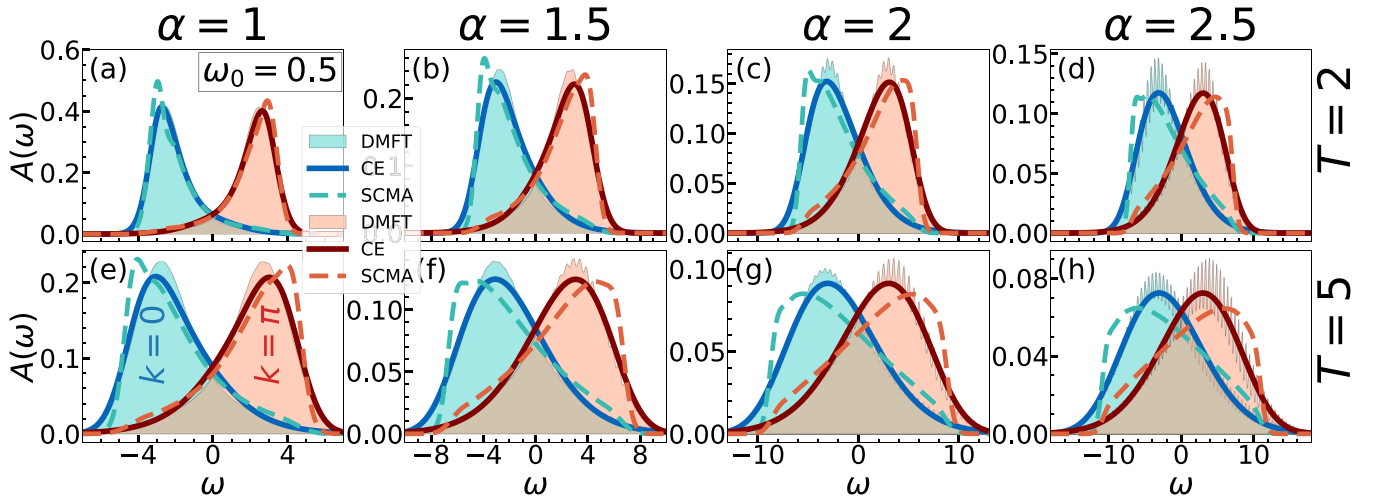
FIG. 7. (a)–(h) CE, DMFT, and SCMA spectral functions in 1D for $t_0 = 1$, $\omega_0 = 0.5$, and $k = 0, \pi$.

All of these are correctly predicted by the CE. However, the disagreement between $\mathcal{M}_n^{\text{exact}}$ and $\mathcal{M}_n^{\text{CE}}$ appears for $n = 5$, where we find

$$
\begin{aligned}
\mathcal{M}_5^{\text{exact}}(\mathbf{k}) = {}& \varepsilon_{\mathbf{k}}^5 + 3g^2\omega_0\big(2t_0^2 + \varepsilon_{\mathbf{k}}^2\big) + g^2\omega_0^3 \\
& + 2g^2\big(2\varepsilon_{\mathbf{k}}^3 + 5g^2\omega_0 + \varepsilon_{\mathbf{k}}\omega_0^2 + 2t_0^2\varepsilon_{\mathbf{k}}\big)(2n_{\text{ph}} + 1) \\
& + 7g^4\varepsilon_{\mathbf{k}}(2n_{\text{ph}} + 1)^2, \quad\quad (27\text{a})
\end{aligned}
$$

$$
\mathcal{M}_5^{\text{CE}}(\mathbf{k}) = \mathcal{M}_5^{\text{exact}}(\mathbf{k}) - 2g^4\varepsilon_{\mathbf{k}}(2n_{\text{ph}} + 1)^2. \quad (27\text{b})
$$

Hence, CE cannot be exact in the limit $T \to \infty$. However, we see that there are two limits where CE can potentially be exact: the weak-coupling limit $g \to 0$ and the atomic limit $\varepsilon_{\mathbf{k}} \to 0$. It turns out that CE is actually exact in both of these limits, as seen from Eqs. (3), (7), and (14) for the weak-coupling and Sec. III D for the atomic limit. We note that the SCMA gives correct sum rules only for $n \leqslant 3$ [42]. This is a consequence of the fact that SCMA ignores one of the fourth-order diagrams ($\sim g^4$) since it includes only the noncrossing diagrams. Also, we numerically checked that the DMFT results are in agreement with all of the sum rules that we listed above.

D. Atomic limit

In the atomic limit ($t_0 = 0$), the cumulant function can be evaluated exactly:

$$
C(t) = \alpha^2(-2n_{\text{ph}} - 1 + it\omega_0 + iD(t)). \quad (28)
$$

This follows from Eq. (16), using $J_0(0) = 1$. If we express the phonon propagator as $iD(t) = 2\sqrt{n_{\text{ph}}(n_{\text{ph}} + 1)} \cos[\omega_0(t + \frac{i}{2T})]$ and use the modified Jacobi-Anger identity

$$
e^{2\alpha^2\sqrt{n_{\text{ph}}(n_{\text{ph}}+1)}\cos[\omega_0(t+\frac{i}{2T})]}
$$

$$
= \sum_{l=-\infty}^{\infty} I_l\big(2\alpha^2\sqrt{n_{\text{ph}}(n_{\text{ph}} + 1)}\big)e^{-il\omega_0 t}e^{\frac{l\omega_0}{2T}}, \quad (29)
$$

where I_l are the modified Bessel functions of the first kind, the spectral function [see Eqs. (3) and (4)] can be calculated

analytically and reads as

$$
A(\omega) = e^{-\alpha^2(2n_{\text{ph}}+1)}
$$

$$
\times \sum_{l=-\infty}^{\infty} I_l\big(2\alpha^2\sqrt{n_{\text{ph}}(n_{\text{ph}} + 1)}\big)e^{\frac{l\omega_0}{2T}}\delta(\omega + \alpha^2\omega_0 - l\omega_0).
$$

$$
(30)
$$

In the limit $T \to 0$, the previous expression reduces to

$$
A(\omega) = e^{-\alpha^2} \sum_{l=0}^{\infty} \frac{\alpha^{2l}}{l!}\delta(\omega + \omega_0(\alpha^2 - l)). \quad (31)
$$

This proves that CE gives correct results in the atomic limit, as Eqs. (30) and (31) coincide with the known exact results [1,44].

In contrast, the SCMA (let alone the MA) does not share this property, which is easy to show at zero temperature. In this case, Eq. (20a) and the Dyson equation imply that

$$
G(\omega) = \frac{1}{\omega - g^2 G(\omega - \omega_0)}. \quad (32)
$$

The previous equation can be solved by the iterative application of itself in terms of the continued fraction

$$
G(\omega) = \cfrac{1}{\omega - \cfrac{g^2}{\omega - \omega_0 - \cfrac{g^2}{\omega - 2\omega_0 - \cfrac{g^2}{\omega - 3\omega_0 - \cdots}}}}. \quad (33)
$$

This does not coincide with Eq. (35) from Ref. [53], which represents the exact solution. Thus, SCMA cannot reproduce the correct result in the atomic limit.

While the CE is exact in the atomic limit ($t_0 = 0$), it is not immediately obvious how far from this limit it continues to give reliable results. This is why we now examine the regimes with small hopping parameter t_0. Since the lifetime is infinitely large in some of these regimes (see Fig. 2), we introduce artificial attenuation η for the Green's function in real time by making a replacement $G(t) \to G(t)e^{-\eta t}$. The results are presented in Fig. 8. Here, the dotted line is the analytic solution in the atomic limit ($t_0 = 0$), determined by Eq. (30), where the Dirac delta functions have been replaced by Lorentzians of half-width η. It is used as a measure to see
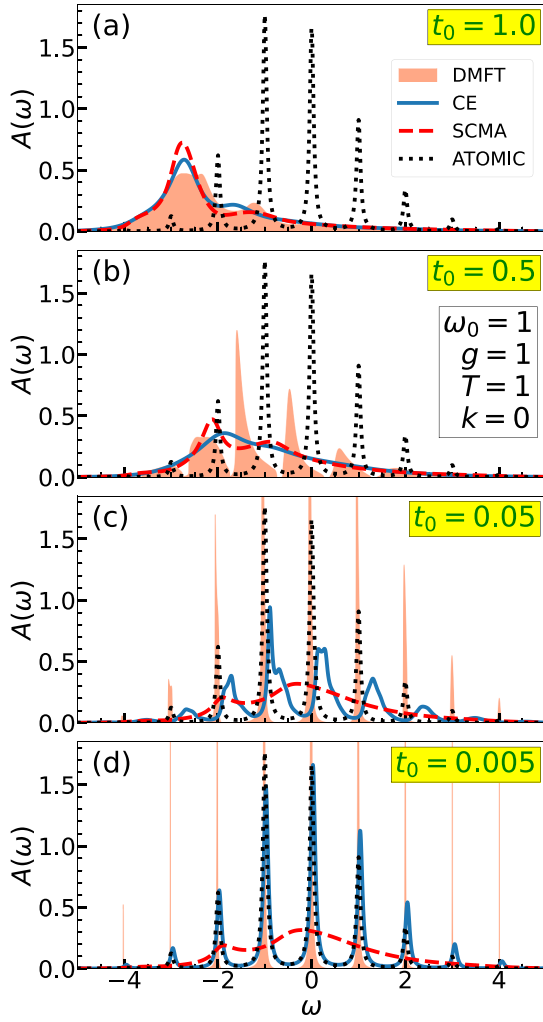
FIG. 8. (a)–(f) CE, DMFT, and SCMA spectral functions close to the atomic limit. Here, we use artificial Lorentzian broadening with half width set to $\eta = 0.05$.

how far the regime we are examining is from the exact atomic limit. In Fig. 8(a), we see that DMFT, SCMA, and CE spectral functions are in agreement. This regime is quite far from the atomic limit, as indicated by the dotted line. Figure 8(b) shows that the DMFT spectral function already consists of a series of peaks for $t_0 = 0.5$, while the CE and SCMA spectral functions are too flattened out. While the CE solution significantly improved in Fig. 8(c), it is still not giving satisfactory results, even though the DMFT suggests that we are already close to the atomic limit. Only for $t_0 \lesssim 0.005$ does the CE solution give accurate results; see Fig. 8(d). However, this is practically already at the atomic limit. It is interesting to note that while both the DMFT and the CE are exact in the weak-coupling and in the atomic limit, their behavior in other regimes can be quite different.

IV. QUASIPARTICLE PROPERTIES

We now investigate the quasiparticle properties obtained from the CE method and compare them extensively to the results obtained from the DMFT and SCMA. We note that

the lifetime within the CE was already studied in Sec. II A 4, so we supplement that study here with the results for the ground-state energy and the effective mass. Here we show the results in one, two, and three dimensions. Comparison with the MA ground-state energy, in the 1D case, is presented in Sec. III of the SM [54].

A. Ground-state energy

The polaron band dispersion $E_{p,\mathbf{k}}$ within the CE is given by the real part of Eq. (12), where the self-energy is taken in the MA:

$$E_{p,\mathbf{k}} = \varepsilon_{\mathbf{k}} + \operatorname{Re}\Sigma^{\mathrm{MA}}(\varepsilon_{\mathbf{k}}). \tag{34}$$

Since we deal with a single electron in the band, the ground-state energy E_p is given by $E_{p,\mathbf{k}=0}$ evaluated at zero temperature. In the 1D case, E_p is straightforwardly evaluated using Eq. (19) and reads as follows:

$$E_p^{\mathrm{1D}} = -2t_0 - \frac{\alpha^2\omega_0^2}{\sqrt{\omega_0^2 + 4\omega_0 t_0}}. \tag{35}$$

For the expression in higher dimensions, we need to go back to Eq. (14) that holds in any number of dimensions. At $T = 0$, it reads as

$$\operatorname{Im}\Sigma^{\mathrm{MA}}(\omega) = -\pi\alpha^2\omega_0^2\rho(\omega - \omega_0). \tag{36}$$

The real part of $\Sigma^{\mathrm{MA}}(\omega)$ is obtained using the Kramers-Kronig relation

$$\operatorname{Re}\Sigma^{\mathrm{MA}}(\omega) = \pi\alpha^2\omega_0^2\mathcal{H}[\rho](\omega - \omega_0), \tag{37}$$

where $\mathcal{H}[\rho](\omega) = \mathcal{P}\int_{-\infty}^{\infty}\frac{d\nu}{\pi}\frac{\rho(\nu)}{\omega-\nu}$ is the Hilbert transform of the density of states $\rho(\omega)$ and $\mathcal{P}$ is the Cauchy principle value. The evaluation of the Hilbert transform may be reduced to the evaluation of the Fourier transform $\mathcal{F}$, using the following identity:

$$\mathcal{F}^{-1}\mathcal{H}[\rho](t) = -i\operatorname{sgn}(t)\,\mathcal{F}^{-1}[\rho](t). \tag{38}$$

The inverse Fourier transform of the density of states on the right-hand side was already calculated in Eq. (15) for the case of the hypercubic lattice with the nearest-neighbor hopping. Hence, $\mathcal{H}[\rho](\omega)$ is obtained by applying $\mathcal{F}$ on both sides of Eq. (38),

$$\mathcal{H}[\rho](\omega) = \frac{1}{\pi}\int_0^{\infty}dx J_0(2t_0 x)^n \sin(x\omega), \tag{39}$$

where n is the number of dimensions. The polaron band dispersion then reads as

$$E_{p,\mathbf{k}} = \varepsilon_{\mathbf{k}} + \alpha^2\omega_0^2\int_0^{\infty}dx J_0(2t_0 x)^n \sin\left(x(\varepsilon_{\mathbf{k}} - \omega_0)\right). \tag{40}$$

E_p is thus a linear function with respect to α^2, whose intercept is $\varepsilon_{\mathbf{k}}$, while its slope can be calculated accurately using the numerical scheme described in Appendix A. In the 2D case, it admits an analytical solution

$$E_p^{\mathrm{2D}} = -4t_0 - \frac{2\alpha^2\omega_0^2}{\pi(4t_0 + \omega_0)}K\left(\frac{4t_0}{4t_0 + \omega_0}\right), \tag{41}$$

where $K(k) = \int_0^{\pi/2} d\theta/\sqrt{1 - k^2\sin^2\theta}$ is the complete elliptic integral of the first kind. In the case $n = 3$, the integral
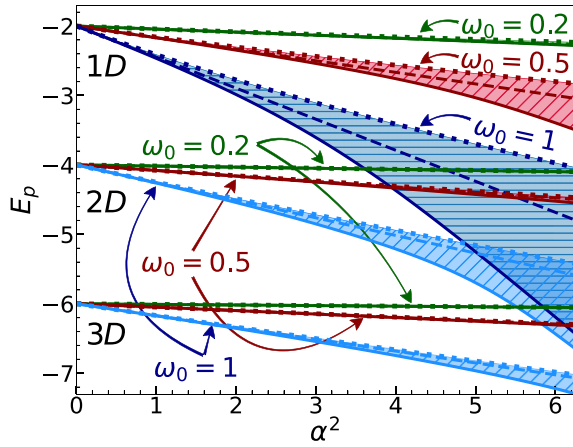
FIG. 9. Ground-state energy within the DMFT (solid line), CE (dashed line), and SCMA (dotted line). Here, $t_0 = 1$ and $T = 0$.

in Eq. (40) does not admit a closed-form solution and thus requires numerical calculation.

The polaron band dispersion $E_{p,\mathbf{k}}$ (and thus the ground state E_p) within the DMFT and SCMA is obtained numerically, as the smallest solution of the following equation:

$$E_{p,\mathbf{k}} = \varepsilon_{\mathbf{k}} + \text{Re}\,\Sigma(E_{p,\mathbf{k}}). \tag{42}$$

Results for the 1D, 2D, and 3D case are presented in Fig. 9. The DMFT benchmark, which is known to be very accurate [52], always gives the lowest ground-state energy predictions in comparison to the CE and SCMA. We see that CE always outperforms the SCMA, despite the fact that its predictions of the energy are always a linear function of α^2. In the 1D case, we see that CE results for $\omega_0 = 0.5$ start to deviate more significantly from the DMFT just around $\alpha = 2.5$. Hence, the range of validity for the CE is similar as for the spectral functions in Fig. 4. The analogous conclusions can also be drawn from $\omega_0 = 1$ data as well. In contrast, all three methods seem to be in agreement for $\omega_0 = 0.2$ in the whole range of presented values of α. This is a consequence of the fact that the ground-state energy correction is small, as seen from Eqs. (35), (40), and (41) by fixing α and decreasing ω_0. However, if we fix $g = \omega_0 \alpha$ and then decrease ω_0, the ground-state energy would change substantially [see, e.g., Eq. (35)], and the CE would certainly give poorer results.

Similar trends are observed in higher dimensions as well. Seemingly, the range of validity of the CE is increased in higher dimensions. However, one should keep in mind that the hopping parameter is always taken to be unity, which means that the bandwidth of the 2D and 3D systems are, respectively, two and three times larger than their 1D counterpart. Therefore, the correlation is weaker for a given coupling α.

B. Effective mass

Around the bottom ($|\mathbf{k}| \approx 0$) of the conduction band, the dispersion $E_{p,\mathbf{k}}$ assumes the following parabolic form:

$$E_{p,\mathbf{k}} \approx \text{const} + \frac{\mathbf{k}^2}{2m^*}, \tag{43}$$

where m^* is the effective mass, which we now calculate.
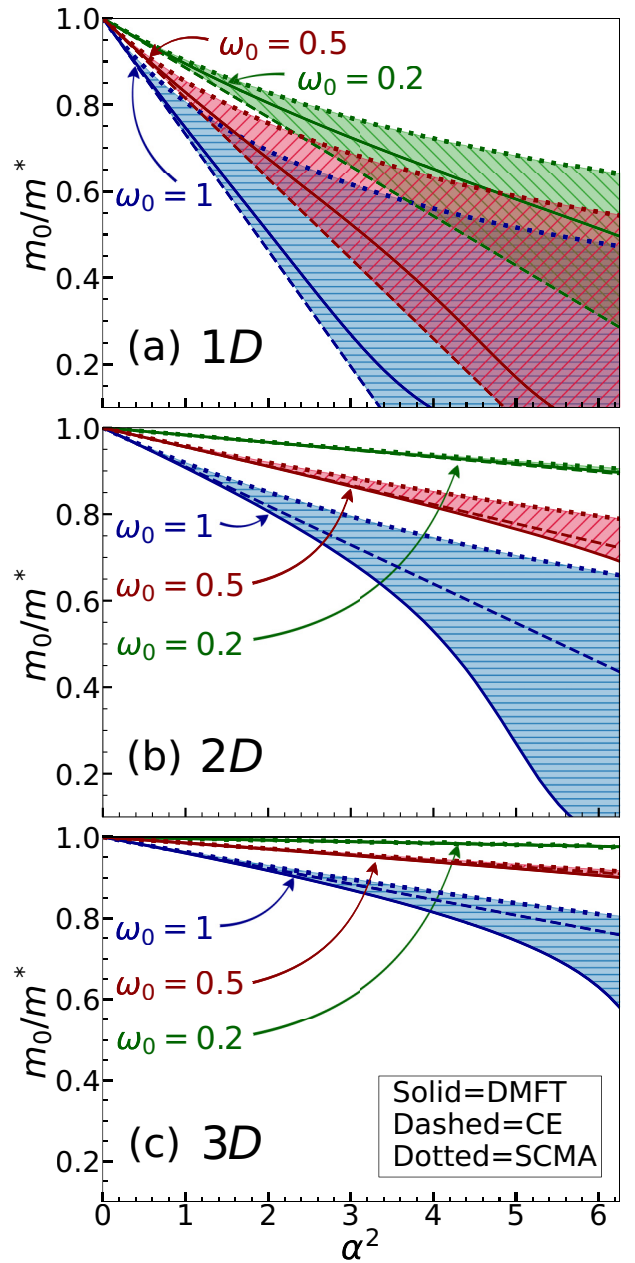
FIG. 10. Effective mass results within the DMFT, CE, and SCMA for $t_0 = 1$ and $T = 0$.

In the 1D case, one obtains the analytical result for the effective mass using Eqs. (19) and (34),

$$\left.\frac{m^*}{m_0}\right|_{1D,T=0} = \frac{1}{1 - \frac{(2t_0 + \omega_0)\alpha^2\sqrt{\omega_0}}{(4t_0 + \omega_0)^{3/2}}}, \tag{44}$$

where $m_0 = 1/(2t_0)$ is the band mass which remains the same irrespective of the number of dimensions. Results for the higher number of dimensions are evaluated using Eq. (40). As for the ground-state energy, the 2D case admits an analytic solution

$$\left.\frac{m^*}{m_0}\right|_{2D,T=0} = \frac{1}{1 - \frac{2\alpha^2\omega_0}{\pi(8t_0 + \omega_0)}E\left(\frac{4t_0}{4t_0 + \omega_0}\right)}, \tag{45}$$

where $E(k) = \int_0^{\pi/2} d\theta \sqrt{1 - k^2 \sin^2 \theta}$ is the complete elliptic integral of the second kind. Results in the n-dimensional case are given by

$$\left.\frac{m^*}{m_0}\right|_{T=0} = \frac{1}{1 + \pi\alpha^2\omega_0^2 \left.\frac{d\mathcal{H}[\rho]}{d\omega}\right|_{\omega=-2nt_0-\omega_0}}, \qquad (46)$$

and require numerical calculation in the general case. From Eq. (46) we see that m_0/m^* is a linear function of α^2. This linear behavior has to break down at one point, as m_0/m^* cannot be negative. This happens for strong interaction, where the CE is certainly not expected to be reliable. The mass renormalization within the DMFT and SCMA is calculated numerically as

$$\left.\frac{m^*}{m_0}\right|_{T=0} = 1 - \left.\frac{d\Sigma(\omega)}{d\omega}\right|_{\omega=E_p}, \qquad (47)$$

where E_p is the ground-state energy. Results for the DMFT, CE, and SCMA effective mass in different parameter regimes and for different number of dimensions are presented in Fig. 10. In the 1D case, we see that the CE always underestimates, while the SCMA overestimates the results from the DMFT benchmark. Still, CE clearly outperforms the SCMA for $\omega_0 = 1$ and $\omega_0 = 0.5$, while the results in the vicinity of the adiabatic limit ($\omega_0 = 0.2$) seem to be equally well (poor) represented by both methods.

In the higher-dimensional case, we see that the CE is always a clearly better approximation than the SCMA, while both of them overestimate the DMFT predictions. As for the ground-state energy, we emphasize again that the hopping parameter was set to 1. As a consequence, the system has a larger bandwidth in the higher-dimensional case and, therefore, the correlations are weaker.

V. MOBILITY

The mobility is defined as the DC conductivity, normalized to the concentration of charge carriers n_e (and their unit charge which we set to $e = 1$), i.e., $\mu = \sigma^{DC}/n_e$. It can be calculated using the Kubo formalism, which relates μ to the current-current correlation function [1]. The latter can be written as a sum of the so-called bubble part, which is completely determined by the spectral functions $A_{\mathbf{k}}(\omega)$ and the vertex corrections. Within the DMFT, the vertex corrections vanish [57,59], while estimating their contribution in the general case is beyond the scope of this paper. In the following, we calculate the mobility solely from the bubble part.

In the case of a 1D system with a single spinless electron in the band, the mobility in the bubble approximation can be written as [1,60]

$$\mu = \frac{4\pi t_0^2}{T} \frac{\sum_k \int_{-\infty}^{\infty} d\nu A_k(\nu)^2 e^{-\nu/T} \sin^2 k}{\sum_k \int_{-\infty}^{\infty} d\nu A_k(\nu) e^{-\nu/T}}. \qquad (48)$$

The processing time required for the calculation of μ within the CE method rises linearly with the number of k points we sum over. This is not the case for the DMFT and SCMA, as their self-energies are k independent and thus need to be calculated only once for a given parameter set. In every parameter regime the CE was applied to, we checked that 64 sampling points in the Brillouin zone are enough to be representative of
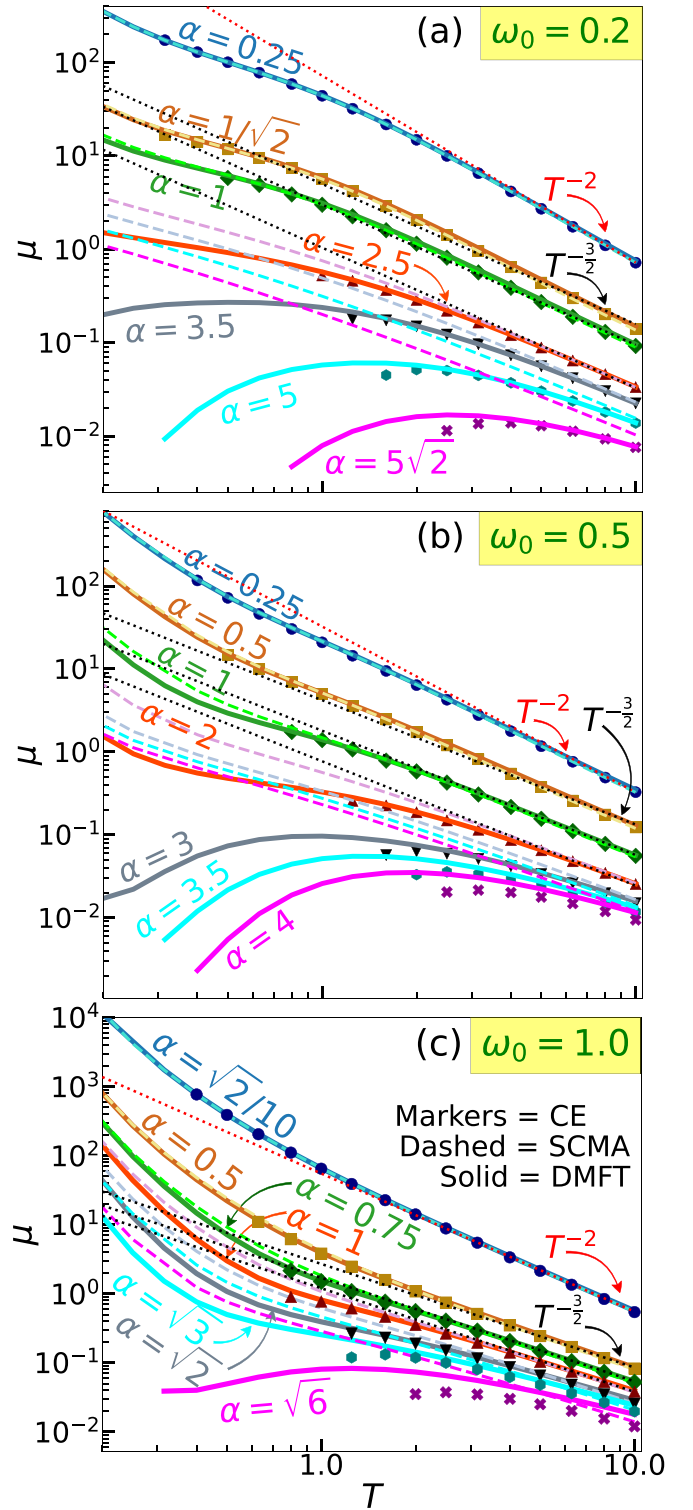

FIG. 11. Temperature dependence of the mobility for the CE, DMFT, and SCMA. The dotted red (black) lines are auxiliary lines with the power law behavior $\mu \propto T^{-2}$ ($\mu \propto T^{-3/2}$). Here $t_0 = 1$.

the thermodynamic limit. This was also crosschecked using the DMFT.

The exponential term $e^{-\nu/T}$ in Eq. (48) has some important implications. Despite the factor $\sin^2 k$, it implies that the largest contribution to the mobility most commonly comes

from the spectral functions around the bottom of the band ($k \approx 0$), as they are typically situated at lower frequencies with respect to their higher momentum counterparts. This is actually helpful, as we have seen that the CE is more reliable for $k \approx 0$ than for $0 < k < \pi$. However, $e^{-\nu/T}$ also introduces numerical instabilities, as even a small numerical noise of $A_k(\nu)$ at $\nu \ll -1$ will be inflated and give an enormous overall error in the mobility. This is why the integrals in Eq. (48) require introducing some kind of negative frequency cutoff $\int_{-\infty}^{\infty} \to \int_{-\Lambda}^{\infty}$. We always check that the mobility results converge with respect to Λ. This is easily done in both the DMFT and SCMA due to the high numerical accuracy of our numerical implementations. The convergence with respect to Λ is much harder to achieve within the CE, as the Green's functions are initially calculated in the time domain and require the use of numerical Fourier transform. We have implemented a well-known interpolation scheme [61] to increase the precision of the Fourier transform. Still, the numerical noise at low temperatures and strong interactions prevented us from precisely calculating the mobility in these regimes. We show only the data where an accurate calculation was possible.

In Fig. 11, we present numerical results for the temperature dependence of the electron mobility. For weak electron-phonon coupling, all methods are in agreement; see Fig. 11(a) for $\alpha \leqslant 1$ and Figs. 11(b) and 11(c) for $\alpha \leqslant 0.5$. Electron-phonon scattering is weak in these regimes, which is why the quasiparticle lifetime τ_k is long, and the linear time dependence dominates in the cumulant function. The spectral function and its square can thus be approximated as $A_k(\omega) \approx \delta(\omega - E_{p,k})$ and $A_k^2(\omega) \approx \frac{\tau_k}{\pi} \delta(\omega - E_{p,k})$, where δ is the Dirac delta function and $E_{p,k}$ is given by Eq. (34). The mobility from Eq. (48) thus simplifies to

$$\mu_{\text{weak}} \approx \frac{4t_0^2}{T} \frac{\sum_k \tau_k e^{-E_{p,k}/T} \sin^2 k}{\sum_k e^{-E_{p,k}/T}}. \quad (49)$$

At high temperatures, Eq. (49) further simplifies as $e^{-E_{p,k}/T} \approx 1$. In this case, the lifetime is inversely proportional to the temperature $\tau_k \propto 1/T$, as seen from Eq. (18), which implies the power-law behavior of the mobility $\mu_{\text{weak}} \propto 1/T^2$. This conclusion holds only for very weak electron-phonon couplings, where the assumption of weak scattering is still satisfied despite the high temperatures; see Figs. 11(a) and 11(b) for $\alpha = 0.25$ and Fig. 11(c) for $\alpha = \sqrt{2}/10$. This assumption is also violated at extremely high temperatures $T \to \infty$.

For stronger couplings, in the limit of high-temperatures $T \gg t_0, \omega_0$, the Green's function in the time domain is quickly damped, which is why $C_k(t)$ can be approximated with just the lowest order (quadratic) Taylor expansion around $t = 0$. Hence, Eqs. (3) and (17) imply that the Green's function can be written as

$$G_k(t) = -i\theta(t) e^{-i\varepsilon_k t} e^{-\frac{g^2}{2}(2n_{\text{ph}}+1)t^2}, \quad (50)$$

while the corresponding spectral function is given by the Gaussian:

$$A_k(\omega) = \frac{e^{-\frac{(\omega-\varepsilon_k)^2}{2g^2(2n_{\text{ph}}+1)}}}{\sqrt{2\pi g^2(2n_{\text{ph}}+1)}}. \quad (51)$$

Plugging this back into Eq. (48) and changing the sum over momenta to integral, we obtain

$$\mu_{\text{high}-T} = \frac{t_0}{g}\sqrt{\frac{\pi}{2n_{\text{ph}}+1}} \exp\left(-\frac{g^2(2n_{\text{ph}}+1)}{4T^2}\right) \frac{I_1\left(\frac{2t_0}{T}\right)}{I_0\left(\frac{2t_0}{T}\right)}, \quad (52)$$

where I_0 and I_1 are modified Bessel functions of the first kind, of zeroth and first orders, respectively. Equation (52) can be simplified by using the following approximations: $2n_{\text{ph}} + 1 \approx 2T/\omega_0$ and $I_1(2t_0/T)/I_0(2t_0/T) \approx t_0/T$, that are valid for large T. Such a simplified formula coincides with the mobility obtained by combining the Einstein relation, between the mobility and diffusion coefficient, with the Marcus formula [45,62]. Furthermore, Eq. (52) implies the power-law behavior for the mobility $\mu_{\text{high}-T} \propto T^{-3/2}$, in the limit $T \gg t_0, \omega_0$. This is confirmed by our numerical results for a wide range of the electron-phonon coupling strengths, where all three methods are in agreement; see Fig. 11(a) for $1/\sqrt{2} \leqslant \alpha \leqslant 2.5$, Fig. 11(b) for $0.5 \leqslant \alpha \leqslant 2$, and Fig. 11(c) for $0.5 \leqslant \alpha \leqslant 1$.

While the SCMA gives satisfactory results for high temperatures and intermediate electron-phonon couplings, it deviates from the DMFT at lower temperatures [see, e.g., Fig. 11(a) for $\alpha = 2.5$ and Fig. 11(b) for $\alpha = 2$] and also for stronger coupling strengths [see, e.g., Fig. 11(a) for $\alpha > 2.5$ and Fig. 11(b) for $\alpha > 2$]. At these stronger couplings, the DMFT predicts the nonmonotonic mobility, where a region of decreasing mobility with decreasing temperature is ascribed to the hopping transport in phenomenological theories [38,62]. The strong coupling mobility is better described by the CE than SCMA, although low-temperature results are missing due to our inability to converge the results with respect to the cutoff Λ. In Appendix D, we also give mobility predictions of the MA.

VI. CONCLUSIONS AND OUTLOOK

In summary, we have presented a comprehensive analysis of the CE method in the context of the Holstein model. The second-order cumulant $C(t)$ is calculated in a broad temperature range for three vibrational frequencies $\omega_0/t_0 = 0.2, 0.5$, and 1, covering a regime from a weak to strong electron-phonon coupling. We mostly focused on the 1D system in the thermodynamic limit but some of the results are shown also in 2D and 3D. To avoid numerical instabilities and to reach high numerical precision, we derived a number of analytical expressions and we used the collocation method in calculations of the cumulant, as well as an interpolation scheme for the Fourier transform in corresponding calculations of the spectral functions. The quasiparticle properties, spectral functions, and charge mobility are shown in comparison to the DMFT and SCMA results. The DMFT, which gives close to the exact solution for the Holstein polaron throughout the parameter space [52], gave a valuable benchmark and facilitated a detailed analysis of the validity of the CE method.

At weak coupling (roughly corresponding to $m_0/m^* \gtrsim 0.9$) CE, DMFT, and SCMA give very similar spectral functions. Most of the spectral weight for $k = 0$ is in the quasiparticle peak, while even a small sideband (satellite) spectral weight is rather well reproduced in all three methods. As the interaction increases, a clear difference in the spectral functions

emerges. Nevertheless, the positions of the CE and DMFT quasiparticle and the first satellite peak at low temperatures are in rather good agreement. Furthermore, the overall spectral weight distribution is in a decent agreement even though the satellite peaks are more pronounced in DMFT for stronger electron-phonon coupling. Roughly speaking, there is a decent agreement in 1D up to the interactions corresponding to $m_0/m^* \sim 0.5$. Interestingly, the agreement between the CE and DMFT spectral functions persists also for $k = \pi$, although CE does not capture a tiny quasiparticle peak. In this case, the DMFT spectral weight almost merges to a single broad peak. We note that the difference for $k = \pi$ observed in Ref. [50] is solely due to considering a lattice of finite $N = 6$ size. The deviation of CE from the exact solution is most obvious for intermediate momenta where the CE solution merges to a single peak, while the satellite structure is seen in DMFT. At high temperatures, one might suspect that the CE would give the exact spectral functions. However, this is not the case, as we showed that the CE gives the exact spectral moments only up to the order $n = 4$. We note that in all these regimes, the CE gives slightly better results than the SCMA, while a single-shot MA is adequate only for very weak interactions.

The spectral functions were used to calculate the charge mobility from the Kubo formula without the vertex corrections. The agreement between DMFT and CE is quite good. This is the case even for stronger electron-phonon coupling where the CE even indicates nonmonotonic behavior of $\mu(T)$, with a region of increasing mobility with temperature which is usually assigned to hopping conduction in phenomenological theories. For strong electron-phonon coupling, the CE mobility results are shown only for $T \gtrsim t_0$ since a very small numerical noise at frequencies $\omega \ll E_p$ affects a precise calculation of mobility at lower temperatures. For high temperatures, the mobility assumes a universal form: For weak electron-phonon coupling $\mu \propto T^{-2}$, while for stronger coupling $\mu \propto T^{-3/2}$. These high-temperature limits can be obtained also analytically from the CE.

The CE method can be easily applied to different Hamiltonians, which makes it a particularly attractive method for the calculation of electronic properties beyond the weak-coupling limit in various systems. In particular, we argue that it will be most useful in calculations of charge mobility, as has already been done in *ab initio* calculations for SrTiO₃ [16] and naphthalene [17]. While our analysis may suggest that the DMFT appears computationally superior to CE, we note that the numerical efficiency that we achieved with DMFT is restricted to the Holstein model by virtue of the analytic solution for the impurity problem [53] and the local Green's function [52]. For predicting the properties of real materials, the numerical resources within the DMFT are vastly increased and also the issue of nonlocal correlations may emerge, while the CE remains simple and relatively inexpensive. Of course, for a definitive answer on the range of validity of CE in connection with *ab initio* calculations, one needs to perform a similar analysis for the Fröhlich model and for other models which can be used for realistic description of the electronic spectra and charge transport in real materials. A useful hint in this direction is provided by Ref. [51], which shows that the CE, around the bottom of the band, gives promising results for the spectral function even in the case when the phonons have a dispersion [63]. Another very interesting question that we leave for further work is a possible contribution of vertex corrections to conductivity. Based on the weak coupling result [64], one might assume that their contribution is small for optical phonons, but this remains to be determined in the case of stronger coupling. Our high-temperature results for mobility may also be quite useful when analyzing a dominant type of electron-phonon coupling in real materials. Still, one needs to be cautious in such analyses since we see that at lower temperatures $\mu(T)$ does not assume a simple universal form.

APPENDIX A: NUMERICAL INTEGRATION SCHEME FOR THE HIGHLY OSCILLATING FUNCTIONS IN THE CE METHOD

We present a numerical integration scheme for the calculation of the cumulant function from Eq. (16). Since $C_{\mathbf{k}}(t)$ will be expressed numerically on some t-grid $[t_0 = 0, t_1 \ldots t_{G-1}]$, it is much better to divide the integral $\int_0^t$ from Eq. (16) into a sum of integrals of the form $\int_{t_{i-1}}^{t_i}$, where t_i are times from the previously defined t grid. In this manner, we do not integrate over the same interval multiple times. To shorten the notation, from now on, we denote $a \equiv t_{i-1}$ and $b \equiv t_i$. There are two different types of integrals in Eq. (16), and both of them have the following form:

$$I = \int_a^b dx\, g(x) e^{i r_1 x} J_0(r_2 x)^n, \qquad (A1)$$

where $g(x)$ is either a linear or a constant function, $r_1 = \varepsilon_{\mathbf{k}} \pm \omega_0$, and $r_2 = 2t_0$. Numerical integration of Eq. (A1) has already been studied by Levin for arbitrary r_1 and r_2 and slowly varying $g(x)$ [55]. In the rest of this Appendix, we review this method in the 1D ($n = 1$), 2D ($n = 2$), and 3D ($n = 3$) cases. The main idea is to rewrite the subintegral function as a scalar product of two columns $|\tilde{g}(x)\rangle$ and $|\tilde{J}(x)\rangle$, whose elements are functions:

$$I = \int_a^b dx \langle \tilde{g}(x) | \tilde{J}(x) \rangle. \qquad (A2)$$

Column $|\tilde{g}(x)\rangle$ consists exclusively of slowly varying functions, while $|\tilde{J}(x)\rangle$ contains highly oscillating functions, with the property that

$$\frac{d|\tilde{J}(x)\rangle}{dx} = \hat{A}(x)|\tilde{J}(x)\rangle, \qquad (A3)$$

where $\hat{A}(x)$ is a matrix of slowly varying functions. Then, the integral from Eq. (A2) can be written as

$$I = \int_a^b dx \frac{d}{dx} \langle \tilde{f}(x)|\tilde{J}(x)\rangle = \langle \tilde{f}(b)|\tilde{J}(b)\rangle - \langle \tilde{f}(a)|\tilde{J}(a)\rangle, \tag{A4}$$

where $|\tilde{f}(x)\rangle$ satisfies

$$\left(\frac{d}{dx} + \hat{A}^{\dagger}(x)\right)|\tilde{f}(x)\rangle = |\tilde{g}(x)\rangle. \tag{A5}$$

This is then, following Levin [55], solved by formally expanding $|\tilde{f}(x)\rangle = \sum_{k=1}^M u_k(x)[c_k \ d_k \ \dots]^T$ into a basis set of polynomials $u_k(x) = (x - \frac{a+b}{2})^{k-1}$ and determining the unknown polynomial coefficients $c_k, d_k \dots$ by imposing that Eq. (A5) is exactly satisfied at M uniformly distributed collocation points $x_j = a + \frac{(j-1)(b-a)}{M-1}$, $j = 1 \dots M$. The initial problem is thus reduced to a simple linear algebra problem.

1. 1D case

In the 1D case ($n = 1$), columns $|\tilde{g}(x)\rangle$ and $|\tilde{J}(x)\rangle$ assume the following form:

$$|\tilde{g}(x)\rangle = [g(x) \ 0]^T, \tag{A6a}$$

$$|\tilde{J}(x)\rangle = e^{ir_1 x}[J_0(r_2 x) \ J_1(r_2 x)]^T, \tag{A6b}$$

where $J_0(x)$ and $J_1(x)$ are the Bessel functions of the first kind, of zeroth and first order. The matrix $\hat{A}(x)$, such that Eq. (A3) holds, is given by

$$\hat{A}(x) = \begin{bmatrix} ir_1 & -r_2 \\ r_2 & ir_1 - \frac{1}{x} \end{bmatrix}. \tag{A7}$$

The unknown coefficients c_k and d_k, which determine the column function

$$|\tilde{f}(x)\rangle = \sum_{k=1}^M u_k(x)[c_k \ d_k]^T, \tag{A8}$$

are obtained from the following set of $2M$ linear equations:

$$\begin{bmatrix} \mathcal{C} & \mathcal{C}^d \\ \mathcal{D}^c & \mathcal{D} \end{bmatrix} \begin{bmatrix} c_1 \\ \vdots \\ c_M \\ d_1 \\ \vdots \\ d_M \end{bmatrix} = \begin{bmatrix} g(x_1) \\ \vdots \\ g(x_M) \\ 0 \\ \vdots \\ 0 \end{bmatrix}. \tag{A9}$$

Here, $\mathcal{C}, \mathcal{C}^d, \mathcal{D}^c, \mathcal{D}$ are $M \times M$ matrices that read as

$$\mathcal{C}_{ij} = u'_j(x_i) - ir_1 u_j(x_i); \quad \mathcal{C}^d_{ij} = r_2 u_j(x_i), \tag{A10a}$$

$$\mathcal{D}_{ij} = u'_j(x_i) - \left(ir_1 + \frac{1}{x_i}\right)u_j(x_i); \quad \mathcal{D}^c_{ij} = -r_2 u_j(x_i). \tag{A10b}$$

2. 2D case

In the 2D case, the relevant quantities are given by

$$|\tilde{g}(x)\rangle = [g(x) \ 0 \ 0]^T,$$

$$|\tilde{J}(x)\rangle = e^{ir_1 x}[J_0(r_2 x)^2 \ J_0(r_2 x)J_1(r_2 x) \ J_1(r_2 x)^2]^T,$$

$$\hat{A}(x) = \begin{bmatrix} ir_1 & -2r_2 & 0 \\ r_2 & ir_1 - \frac{1}{x} & -r_2 \\ 0 & 2r_2 & ir_1 - \frac{2}{x} \end{bmatrix}. \tag{A11}$$

The column $|\tilde{f}(x)\rangle = \sum_{k=1}^M u_k(x)[c_k \ d_k \ e_k]^T$ is determined by c_k, d_k, and e_k, which are obtained as a solution of the following system of $3M$ linear equations:

$$\begin{bmatrix} \mathcal{C} & \mathcal{C}^d & \mathcal{C}^e \\ \mathcal{D}^c & \mathcal{D} & \mathcal{D}^e \\ \mathcal{E}^c & \mathcal{E}^d & \mathcal{E} \end{bmatrix} \begin{bmatrix} c_1 \\ \vdots \\ c_M \\ d_1 \\ \vdots \\ e_1 \\ \vdots \end{bmatrix} = \begin{bmatrix} g(x_1) \\ \vdots \\ g(x_M) \\ 0 \\ \vdots \\ 0 \\ \vdots \end{bmatrix}. \tag{A12}$$

Here, $\mathcal{C}, \mathcal{C}^d \dots \mathcal{E}$ are $M \times M$ matrices. Elements of $\mathcal{C}_{ij}$ and $\mathcal{C}^d_{ij}$ are the same as in Eq. (A10), while $\mathcal{C}^e_{ij} = \mathcal{E}^c_{ij} = 0$. All the other elements are given by

$$\mathcal{D}_{ij} = u'_j(x_i) - \left(ir_1 + \frac{1}{x_i}\right)u_j(x_i),$$

$$\mathcal{E}_{ij} = u'_j(x_i) - \left(ir_1 + \frac{2}{x_i}\right)u_j(x_i),$$

$$\mathcal{D}^c_{ij} = -2r_2 u_j(x_i); \quad \mathcal{D}^e_{ij} = 2r_2 u_j(x_i); \quad \mathcal{E}^d_{ij} = -r_2 u_j(x_i). \tag{A13}$$

3. 3D case

The procedure that was presented so far is actually quite easily generalized to the 3D case as well. Here, the quantities of interest are easily derived and read as

$$|\tilde{g}(x)\rangle = [g(x) \ 0 \ 0 \ 0]^T,$$

$$|\tilde{J}(x)\rangle = e^{ir_1 x}[J_0(r_2 x)^3 \ J_0(r_2 x)^2 J_1(r_2 x)$$

$$J_0(r_2 x)J_1(r_2 x)^2 \ J_1(r_2 x)^3]^T,$$

$$\hat{A}(x) = \begin{bmatrix} ir_1 & -3r_2 & 0 & 0 \\ r_2 & ir_1 - \frac{1}{x} & -2r_2 & 0 \\ 0 & 2r_2 & ir_1 - \frac{2}{x} & -r_2 \\ 0 & 0 & 3r_2 & ir_1 - \frac{3}{x} \end{bmatrix},$$

$$\tilde{f}(x) = \sum_{k=1}^M u_k(x)[c_k \ d_k \ e_k \ f_k]^T, \tag{A14}$$

where the coefficients c_k, d_k, e_k, and f_k satisfy

$$
\begin{bmatrix}
\mathcal{C} & \mathcal{C}^d & \mathcal{C}^e & \mathcal{C}^f \\
\mathcal{D}^c & \mathcal{D} & \mathcal{D}^e & \mathcal{D}^f \\
\mathcal{E}^c & \mathcal{E}^d & \mathcal{E} & \mathcal{E}^f \\
\mathcal{F}^c & \mathcal{F}^d & \mathcal{F}^e & \mathcal{F}
\end{bmatrix}
\begin{bmatrix}
c_1 \\ \vdots \\ c_M \\ d_1 \\ \vdots \\ e_1 \\ \vdots \\ f_1 \\ \vdots
\end{bmatrix}
=
\begin{bmatrix}
g(x_1) \\ \vdots \\ g(x_M) \\ 0 \\ \vdots \\ 0 \\ \vdots \\ 0 \\ \vdots
\end{bmatrix}. \tag{A15}
$$

Here $\mathcal{C}_{ij}$, $\mathcal{C}_{ij}^d$, $\mathcal{C}_{ij}^e$, $\mathcal{D}_{ij}$, $\mathcal{D}_{ij}^e$, $\mathcal{E}_{ij}^c$, and $\mathcal{E}_{ij}$ are the same as in Eqs. (A10) and (A13), while $\mathcal{C}_{ij}^f = \mathcal{F}_{ij}^c = \mathcal{D}_{ij}^f = \mathcal{F}_{ij}^d = 0$. All other elements are given by

$$
\mathcal{E}_{ij}^d = -2r_2 u_j(x_i); \quad \mathcal{E}_{ij}^f = 3r_2 u_j(x_i),
$$
$$
\mathcal{D}_{ij}^c = -3r_2 u_j(x_i); \quad \mathcal{F}_{ij}^e = -r_2 u_j(x_i),
$$
$$
\mathcal{F}_{ij} = u_j'(x_i) - \left(ir_1 + \frac{3}{x_i} \right) u_j(x_i). \tag{A16}
$$

Thus, our numerical scheme has been completely specified. We note that Eqs. (A10), (A13), and (A16) explicitly demonstrate that our numerical scheme is singular at $x = 0$. This does not pose any problems, as the subintegral function in our initial expression Eq. (A1) is not highly oscillatory around $x = 0$. Therefore, the trapezoid scheme can be applied there.

APPENDIX B: 2D SPECTRAL FUNCTIONS

We now examine the CE spectral functions in two dimensions and compare them to the results from DMFT and SCMA. We investigate the Hamiltonian from Eq. (1) on a square lattice and set $\hbar$, k_B and lattice constant to 1.

In the 2D case, the cumulant function is calculated from Eq. (16) by setting $n = 2$, and by exploiting the numerical integration scheme from Appendix A. The procedure for the implementation of the DMFT and SCMA is the same as explained in Sec. II B, with the only difference being that Eq. (22) no longer represents the solution for the local Green's function from Eqs. (20b) and (21). The local Green's function for the square lattice is obtained as follows. Let us introduce $B(\omega) \equiv (\omega - \Sigma(\omega))/(2t_0)$ and rewrite Eq. (21) as

$$
G(\omega) = -\int_{-\infty}^{\infty} dx \hat{\rho}(x) \int_{-\infty}^{\infty} d\varepsilon \frac{e^{ix\varepsilon}}{\varepsilon - 2t_0 B(\omega)}. \tag{B1}
$$

The integral over ε can be solved using the residue theorem. It is thus important to note that the subintegral function has only a single pole at $\varepsilon_{\text{pole}} = 2t_0 B(\omega)$ that is situated at the upper half-plane, i.e., $\text{Im}B(\omega) > 0$ (since $\text{Im}\Sigma(\omega) < 0$). Hence

$$
G(\omega) = -2\pi i \int_{-\infty}^{\infty} dx \tilde{\rho}(x) e^{2ixt_0 B(\omega)} \theta(x). \tag{B2}
$$

Here $\tilde{\rho}(x)$ is given by Eq. (15) for $n = 2$. Substituting this into Eq. (B2) and solving the integral gives

$$
G(\omega) = \frac{K\left(\frac{2}{B(\omega)} \right)}{B(\omega)\pi t_0}, \tag{B3}
$$

where $K(k) \equiv \int_0^{\pi/2} d\theta / \sqrt{1 - k^2 \sin^2 \theta}$ is the complete elliptic integral of the first kind.

Results are presented in Fig. 12. We note that in Figs. 12(a)–12(d) [Figs. 12(i)–12(l)] the phonon frequency $\omega_0 = 0.2$ ($\omega_0 = 1$) is smaller (larger) than both of the temperatures $T_1 = 0.3$ and $T_2 = 0.7$ that we are considering. Therefore, we focus on Figs. 12(e)–12(h) where $T_1 < \omega_0 < T_2$, while other regimes can be analyzed analogously. We see that most of the spectral weight is concentrated in a smaller range of frequencies than in the 1D case; see Figs. 4 and 12(e)–12(h). This is a consequence of the fact that the hopping parameter is always set to unity, while the 2D bandwidth is twice as large in comparison with the bandwidth in the 1D system. Spectral functions from Figs. 12(e)–12(g) exhibit qualitatively similar behavior as results for the 1D system in Figs. 4(a)–4(d). Here, all methods are in agreement and predict that the quasiparticle peak dominates, while there is only a single tiny satellite structure that is more pronounced at higher temperatures. However, it seems that the satellites are more pronounced in the 1D spectral functions. A much more complicated multipeak structure is predicted by the DMFT in Fig. 10(h), where a large discrepancy can be observed in comparison to the CE and SCMA results. A better agreement is observed for higher temperatures.

It is interesting to note that while the DMFT frequently gave sharper peaks than other methods in 1D (see Fig. 4), here the roles are reversed. This is a consequence of the strong Van Hove singularity at the bottom of the band of a 1D system, which is highly relevant in our case when the concentration of electrons is very low, while the singularity in the 2D system is weaker and shifted to the center of the band.

APPENDIX C: A DETAILED STUDY OF THE SPECTRAL FUNCTION FOR $t_0 = \omega_0 = g = 1$ AND $k = \pi$

In Sec. III, we concluded that the CE successfully captures the main features of the spectral functions both at the bottom of the band ($k \approx 0$) and at top of the band ($k \approx \pm\pi$) if the electron-phonon coupling is not too strong. Less promising results were reported in Ref. [50], where CE was examined on a finite lattice with $N = 6$ sites in the regime $t_0 = \omega_0 = g = 1$ and $k = \pi$, using the finite-temperature Lanczos method (FTLM) [44] as a benchmark. They found that the CE, in addition to the fact that it does not correctly reproduce a quasiparticle peak, predicts that the most prominent feature of the spectrum consists of only a single broad peak, whereas two distinct peaks are present in the FTLM solution. Here we show that this discrepancy between the CE and FTLM is significantly reduced in the thermodynamic limit.

Reference [50] emphasized that previous conclusions are valid only for low-temperature solutions, while CE becomes accurate for $T \gtrsim \omega_0$. This was confirmed by the FTLM, whose spectral functions in this case look like a single broad
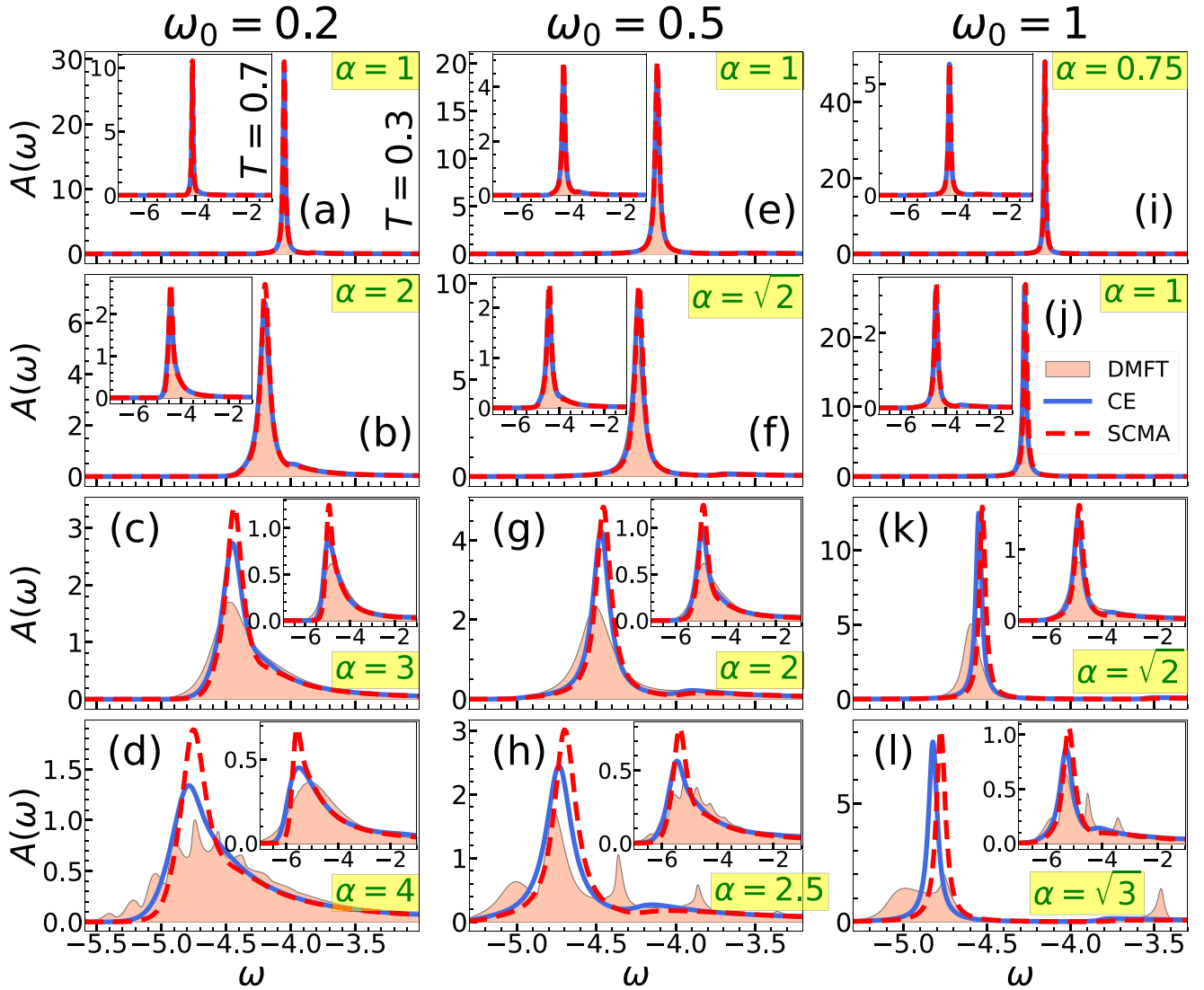
FIG. 12. (a)–(h) Comparison of the CE, DMFT, and SCMA spectral functions in 2D for $k = 0$ and $t_0 = 1$. The main panels show the results for $T_1 = 0.3$, while $T_2 = 0.7$ results are shown in the insets.

peak; see Fig. 1(c) from Ref. [50]. However, Fig. S9 in the Supplemental Material of Ref. [52] demonstrates that the spectral function in the thermodynamic limit for $t_0 = \omega_0 = g = 1$, $k = \pi$ consists of a broad single-peak structure even at $T = 0$. This conclusion was reached by carefully examining the finite-size effects using the numerically exact hierarchical equations of motion method (HEOM). It was established that the system with $N = 10$ lattice sites is representative of the thermodynamic limit, although much smaller systems are required for the $k = 0$ results. Furthermore, the same figure shows that two distinct peaks emerge for $N = 6$ and $k = \pi$, in accordance with the FTLM results. Hence, CE will provide much better results in the thermodynamic limit than previously expected. We note that for $t_0 = \omega_0 = g = 1$ and finite temperatures, one might expect that the required lattice size, representative of the thermodynamic limit, does not exceed $N = 10$, as the electron experiences much more scattering compared to the $T = 0$ case. This will be cross-checked independently (using the DMFT) in the rest of this Appendix for finite T, which satisfies the $T < \omega_0$ condi-

tion. In that case, we analyze the overall performance of the CE.

In Fig. 13(a), we show the FTLM data, (originally from Ref. [44]) used in Ref. [50], and compare them to the DMFT applied on a system of finite lattice size. We exploit the fact that the corresponding spectral functions (although certainly not as accurate in comparison with the exact solution) provide a rough estimate of how large N should be to faithfully represent the thermodynamic limit; see Sec. IV from the Supplemental Material of Ref. [52] for more details. In accordance with the FTLM results, we see that the DMFT spectral function for $N = 6$ also predicts distinct peaks around $\omega \approx 1.5$ and $\omega \approx 2.5$, although there is an additional peak around $\omega \approx 2$. Nevertheless, these results change drastically with increasing N and practically converge for $N = 10$. This is the same N as predicted by HEOM at $T = 0$. Therefore, the presented FTLM results are not representative of the thermodynamic limit. Additionally, Fig. 13(a) also shows that FTLM results for $T = 0.6$ and $T = 0.8$ are quite similar. Hence, our further analysis will be conducted for $T = 0.7$ case.
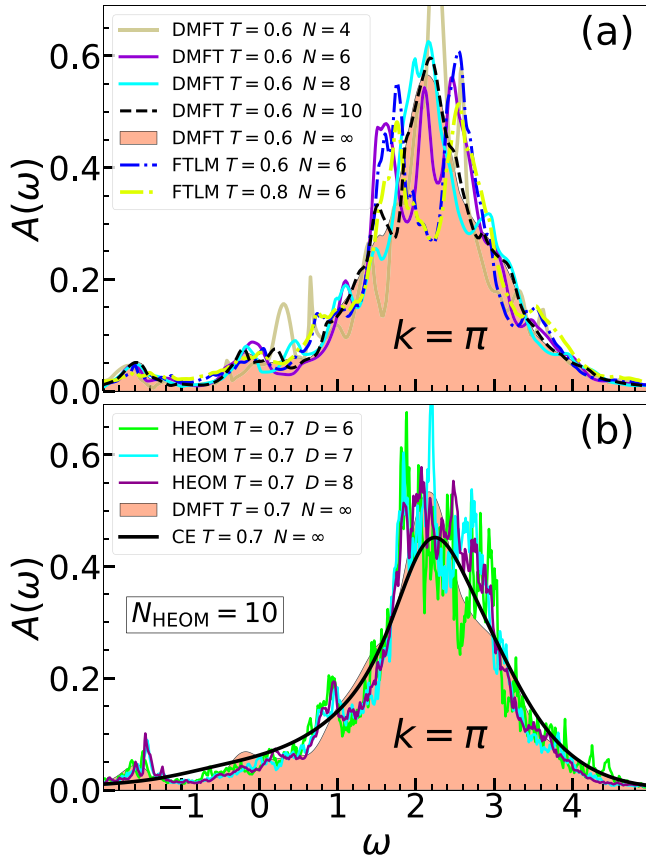
FIG. 13. CE, DMFT, FTLM, and HEOM spectral functions for $t_0 = \omega_0 = g = 1$. (a) Analysis of the finite-size effects. (b) Inspecting the convergence of HEOM data with respect to hierarchy depth D.

In Fig. 13(b), we present HEOM results for $N = 10$ and compare them to CE and DMFT. We note that HEOM has one additional parameter, the so-called hierarchy depth D. For details, we refer the reader to Ref. [47], but we only briefly mention that the numerically exact results are formally obtained in the limit $D \to \infty$. In practice, we always check whether the results converge with respect to D, which cannot be increased indefinitely, as finite computer memory presents a limiting factor. We see that the HEOM results have practically converged for $N = 10$ and $D = 8$. Here, the HEOM solution does not possess the two-peak structure predicted by the FTLM on a smaller lattice size ($N = 6$). It actually gives only a single, broad peak around $\omega \approx 2$, which is correctly reproduced by both the CE and the DMFT. Although the CE misses the quasiparticle peak around $\omega \approx -1.5$, we conclude that CE gives much more accurate results for the thermodynamic limit than for a finite system.

APPENDIX D: MOBILITY RESULTS FROM THE ONE-SHOT MIGDAL APPROXIMATION

In Sec. V, we presented and analyzed the mobility predictions from the CE, DMFT, and SCMA methods. Here, we supplement that study with the data from the one-shot MA (i.e., SCMA without self-consistency). The results are shown in Fig. 14. Since the mobility results have already been
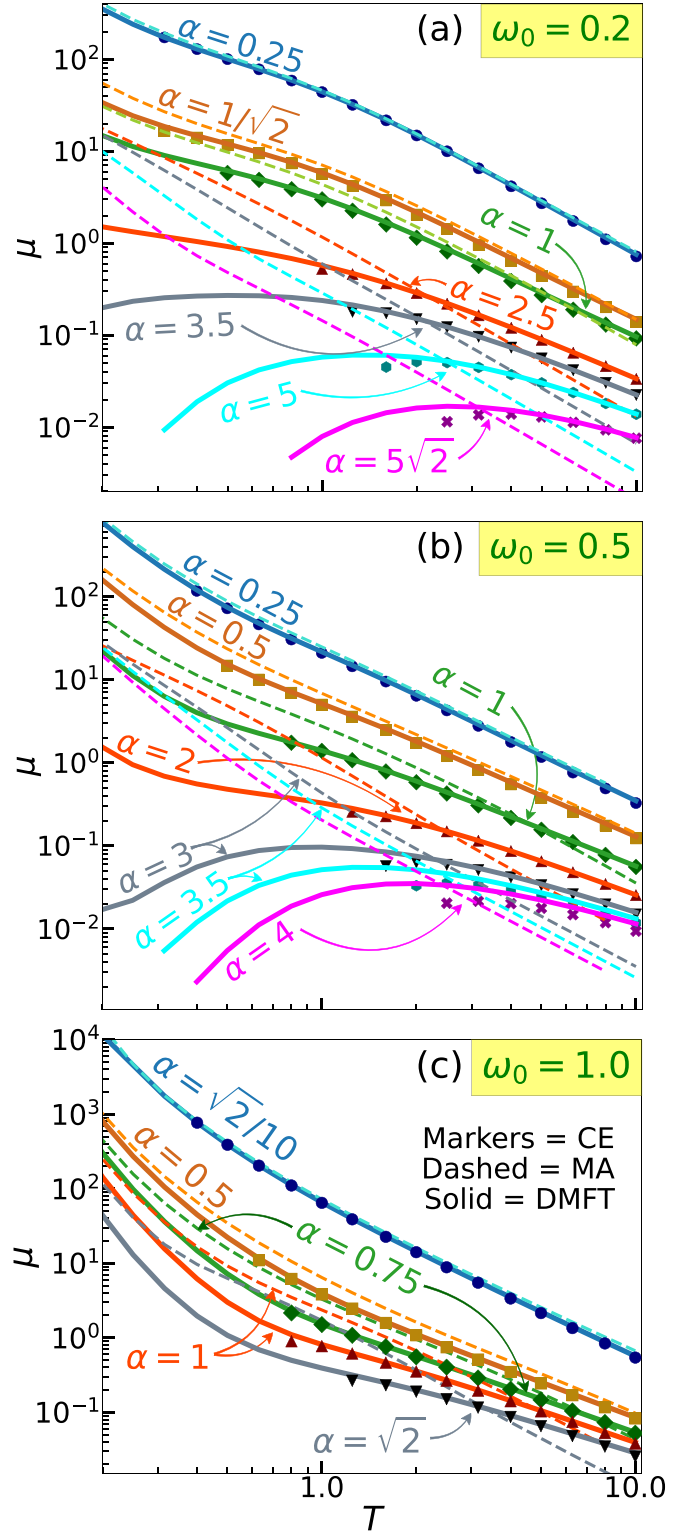
FIG. 14. Temperature dependence of the mobility within CE, DMFT, and MA. Here $t_0 = 1$.

thoroughly analyzed in Sec. V, we will here give only brief comments about the performance of the MA. Figure 14(a) shows that MA is practically useless for $\alpha \gtrsim 2.5$. Here, the results are not even qualitatively correct, regardless of the temperature. Even for $\alpha = 1$, the results are still not satisfactory:

the predictions for $T < 4$ ($T > 9$) overestimate (underestimate) the DMFT benchmark. MA proves to be reliable only for very weak interactions $\alpha \lesssim 1/\sqrt{2}$. Here, the results are better for higher temperatures. This is expected as the MA takes into account only the lowest-order Feynman diagram, while the relevance of higher-order diagrams decreases as the temperature is increased. Similar analysis can be repeated for other phonon frequencies in Figs. 14(b) and 14(c).

[1] G. Mahan, *Many-Particle Physics* (Kluwer Academic, New York, 2000).

[2] R. Kubo, Generalized cumulant expansion method, J. Phys. Soc. Jpn. **17**, 1100 (1962).

[3] B. I. Lundqvist, Characteristic structure in core electron spectra of metals due to the electron-plasmon coupling, Phys. Kondens. Mater. **9**, 236 (1969).

[4] D. C. Langreth, Singularities in the x-ray spectra of metals, Phys. Rev. B **1**, 471 (1970).

[5] L. Hedin, Effects of recoil on shake-up spectra in metals, Phys. Scr. **21**, 477 (1980).

[6] L. Hedin, On correlation effects in electron spectroscopies and the *GW* approximation, J. Phys.: Condens. Matter **11**, R489 (1999).

[7] F. Aryasetiawan, L. Hedin, and K. Karlsson, Multiple Plasmon Satellites in Na and Al Spectral Functions from *Ab Initio* Cumulant Expansion, Phys. Rev. Lett. **77**, 2268 (1996).

[8] B. Holm and F. Aryasetiawan, Self-consistent cumulant expansion for the electron gas, Phys. Rev. B **56**, 12825 (1997).

[9] G. D. Mahan, Phonon-broadened optical spectra: Urbach's rule, Phys. Rev. **145**, 602 (1966).

[10] D. Dunn, ElectronPhonon Interactions in an insulator, Can. J. Phys. **53**, 321 (1975).

[11] O. Gunnarsson, V. Meden, and K. Schönhammer, Corrections to Migdal's theorem for spectral functions: A cumulant treatment of the time-dependent Green's function, Phys. Rev. B **50**, 10462 (1994).

[12] C. Verdi, F. Caruso, and F. Giustino, Origin of the crossover from polarons to Fermi liquids in transition metal oxides, Nat. Commun. **8**, 15769 (2017).

[13] G. Antonius, Y.-H. Chan, and S. G. Louie, Polaron spectral properties in doped ZnO and SrTiO$_3$ from first principles, Phys. Rev. Res. **2**, 043296 (2020).

[14] S. Moser, L. Moreschini, J. Jaćimović, O. S. Barišić, H. Berger, A. Magrez, Y. J. Chang, K. S. Kim, A. Bostwick, E. Rotenberg, L. Forró, and M. Grioni, Tunable Polaronic Conduction in Anatase TiO$_2$, Phys. Rev. Lett. **110**, 196403 (2013).

[15] F. Giustino, Electron-phonon interactions from first principles, Rev. Mod. Phys. **89**, 015003 (2017).

[16] J.-J. Zhou and M. Bernardi, Predicting charge transport in the presence of polarons: The beyond-quasiparticle regime in SrTiO$_3$, Phys. Rev. Res. **1**, 033138 (2019).

[17] B. K. Chang, J.-J. Zhou, N.-E. Lee, and M. Bernardi, Intermediate polaronic charge transport in organic crystals from a many-body first-principles approach, npj Comput. Mater. **8**, 63 (2022).

[18] S. M. Story, J. J. Kas, F. D. Vila, M. J. Verstraete, and J. J. Rehr, Cumulant expansion for phonon contributions to the electron spectral function, Phys. Rev. B **90**, 195135 (2014).

[19] J. J. Kas, J. J. Rehr, and L. Reining, Cumulant expansion of the retarded one-electron Green function, Phys. Rev. B **90**, 085112 (2014).

[20] J. Lischner, D. Vigil-Fowler, and S. G. Louie, Satellite structures in the spectral functions of the two-dimensional electron gas in semiconductor quantum wells: A *GW* plus cumulant study, Phys. Rev. B **89**, 125430 (2014).

[21] F. Caruso and F. Giustino, Spectral fingerprints of electron-plasmon coupling, Phys. Rev. B **92**, 045123 (2015).

[22] J. S. Zhou, J. Kas, L. Sponza, I. Reshetnyak, M. Guzzo, C. Giorgetti, M. Gatti, F. Sottile, J. Rehr, and L. Reining, Dynamical effects in electron spectroscopy, J. Chem. Phys. **143**, 184109 (2015).

[23] B. Gumhalter, V. Kovač, F. Caruso, H. Lambert, and F. Giustino, On the combined use of *GW* approximation and cumulant expansion in the calculations of quasiparticle spectra: The paradigm of Si valence bands, Phys. Rev. B **94**, 035103 (2016).

[24] D. Vigil-Fowler, S. G. Louie, and J. Lischner, Dispersion and line shape of plasmon satellites in one, two, and three dimensions, Phys. Rev. B **93**, 235446 (2016).

[25] J. S. Zhou, M. Gatti, J. J. Kas, J. J. Rehr, and L. Reining, Cumulant Green's function calculations of plasmon satellites in bulk sodium: Influence of screening and the crystal environment, Phys. Rev. B **97**, 035137 (2018).

[26] J. Ma and J. Cao, Förster resonance energy transfer, absorption and emission spectra in multichromophoric systems. I. Full cumulant expansions and system-bath entanglement, J. Chem. Phys. **142**, 094106 (2015).

[27] L. Cupellini, F. Lipparini, and J. Cao, Absorption and circular dichroism spectra of molecular aggregates with the full cumulant expansion, J. Phys. Chem. B **124**, 8610 (2020).

[28] J. A. Nöthling, T. Mančal, and T. Krüger, Accuracy of approximate methods for the calculation of absorption-type linear spectra with a complex system–bath coupling, J. Chem. Phys. **157**, 095103 (2022).

[29] J. P. Nery, P. B. Allen, G. Antonius, L. Reining, A. Miglio, and X. Gonze, Quasiparticles and phonon satellites in spectral functions of semiconductors and insulators: Cumulants applied to the full first-principles theory and the Fröhlich polaron, Phys. Rev. B **97**, 115145 (2018).

[30] N. Kandolf, C. Verdi, and F. Giustino, Many-body Green's function approaches to the doped Fröhlich solid: Exact solutions and anomalous mass enhancement, Phys. Rev. B **105**, 085148 (2022).

[31] A. S. Mishchenko, N. V. Prokof'ev, A. Sakamoto, and B. V. Svistunov, Diagrammatic quantum Monte Carlo study of the Fröhlich polaron, Phys. Rev. B **62**, 6317 (2000).

[32] T. Holstein, Studies of polaron motion: Part I. The molecular-crystal model, Ann. Phys. **8**, 325 (1959).

[33] I. Lang and Y. A. Firsov, Kinetic theory of semiconductors with low mobility, Zh. Eksp. Teor. Fiz. **43**, 1843 (1962) [Sov. Phys. JETP **16**, 1301 (1963)].

[34] A. S. Alexandrov, *Polarons in Advanced Materials,* Springer Series in Materials Science, Vol. 103 (Springer, Dordrecht, 2007).

[35] E. Jeckelmann and S. R. White, Density-matrix renormalization-group study of the polaron problem in the Holstein model, Phys. Rev. B **57**, 6376 (1998).

[36] P. E. Kornilovitch, Continuous-Time Quantum Monte Carlo Algorithm for the Lattice Polaron, Phys. Rev. Lett. **81**, 5382 (1998).

[37] A. H. Romero, D. W. Brown, and K. Lindenberg, Converging toward a practical solution of the Holstein molecular crystal model, J. Chem. Phys. **109**, 6540 (1998).

[38] S. Fratini and S. Ciuchi, Dynamical Mean-Field Theory of Transport of Small Polarons, Phys. Rev. Lett. **91**, 256403 (2003).

[39] S. Fratini and S. Ciuchi, Optical properties of small polarons from dynamical mean-field theory, Phys. Rev. B **74**, 075101 (2006).

[40] C. Zhang, E. Jeckelmann, and S. R. White, Dynamical properties of the one-dimensional Holstein model, Phys. Rev. B **60**, 14092 (1999).

[41] G. L. Goodvin, M. Berciu, and G. A. Sawatzky, Green's function of the Holstein polaron, Phys. Rev. B **74**, 245104 (2006).

[42] M. Berciu, Green's Function of a Dressed Particle, Phys. Rev. Lett. **97**, 036402 (2006).

[43] S. Ciuchi, E. Cappelluti, and S. Fratini, Optical properties of lattice/magnetic small polarons from DMFT, J. Phys. Chem. Solids **69**, 2164 (2008).

[44] J. Bonča, S. A. Trugman, and M. Berciu, Spectral function of the Holstein polaron at finite temperature, Phys. Rev. B **100**, 094307 (2019).

[45] N. Prodanović and N. Vukmirović, Charge carrier mobility in systems with local electron-phonon interaction, Phys. Rev. B **99**, 104304 (2019).

[46] D. Jansen, J. Bonča, and F. Heidrich-Meisner, Finite-temperature density-matrix renormalization group method for electron-phonon systems: Thermodynamics and Holstein-polaron spectral functions, Phys. Rev. B **102**, 165155 (2020).

[47] V. Janković and N. Vukmirović, Spectral and thermodynamic properties of the Holstein polaron: Hierarchical equations of motion approach, Phys. Rev. B **105**, 054311 (2022).

[48] J. Bonča and S. A. Trugman, Electron removal spectral function of a polaron coupled to dispersive optical phonons, Phys. Rev. B **106**, 174303 (2022).

[49] A. S. Mishchenko, N. Nagaosa, and N. Prokof'ev, Diagrammatic Monte Carlo Method for Many-Polaron Problems, Phys. Rev. Lett. **113**, 166402 (2014).

[50] P. J. Robinson, I. S. Dunn, and D. R. Reichman, Cumulant methods for electron-phonon problems. I. Perturbative expansions, Phys. Rev. B **105**, 224304 (2022).

[51] P. J. Robinson, I. S. Dunn, and D. R. Reichman, Cumulant methods for electron-phonon problems. II. The self-consistent cumulant expansion, Phys. Rev. B **105**, 224305 (2022).

[52] P. Mitrić, V. Janković, N. Vukmirović, and D. Tanasković, Spectral Functions of the Holstein Polaron: Exact and Aapproximate Solutions, Phys. Rev. Lett. **129**, 096401 (2022).

[53] S. Ciuchi, F. de Pasquale, S. Fratini, and D. Feinberg, Dynamical mean-field theory of the small polaron, Phys. Rev. B **56**, 4494 (1997).

[54] See Supplemental Material at http://link.aps.org/supplemental/10.1103/PhysRevB.107.125165 for additional figures and derivations.

[55] D. Levin, Fast integration of rapidly oscillatory functions, J. Comput. Appl. Math. **67**, 95 (1996).

[56] A. Migdal, Interaction between electrons and lattice vibrations in a normal metal, Zh. Eksp. Teor. Fiz. **34**, 1438 (1958) [Sov. Phys. JETP **7**, 996 (1958)].

[57] A. Georges, G. Kotliar, W. Krauth, and M. J. Rozenberg, Dynamical mean-field theory of strongly correlated fermion systems and the limit of infinite dimensions, Rev. Mod. Phys. **68**, 13 (1996).

[58] P. E. Kornilovitch, Photoemission spectroscopy and sum rules in dilute electron-phonon systems, Europhys. Lett. **59**, 735 (2002).

[59] A. Khurana, Electrical Conductivity in the Infinite-Dimensional Hubbard Model, Phys. Rev. Lett. **64**, 1990 (1990).

[60] S. Fratini, F. de Pasquale, and S. Ciuchi, Optical absorption from a nondegenerate polaron gas, Phys. Rev. B **63**, 153101 (2001).

[61] W. H. Press, S. A. Teukolsky, W. T. Vetterling, and B. P. Flannery, *Numerical Recipes: The Art of Scientific Computing*, 3rd ed. (Cambridge University Press, Cambridge, 2007).

[62] S. Fratini, D. Mayou, and S. Ciuchi, The transient localization scenario for charge transport in crystalline organic materials, Adv. Funct. Mater. **26**, 2292 (2016).

[63] J. Bonča and S. A. Trugman, Dynamic properties of a polaron coupled to dispersive optical phonons, Phys. Rev. B **103**, 054304 (2021).

[64] G. D. Mahan, Mobility of polarons, Phys. Rev. **142**, 366 (1966).

Supplemental Material: Cumulant expansion in the Holstein model: Spectral functions and mobility

Petar Mitrić, Veljko Janković, Nenad Vukmirović, and Darko Tanasković

Institute of Physics Belgrade, University of Belgrade, Pregrevica 118, 11080 Belgrade, Serbia

Here we supplement the main text by giving an alternative derivation of the cumulant function in Sec. I, additional spectral functions and heat maps in Sec. II, and a comparison of the 1D ground state energy using DMFT, CE, SCMA, and MA in Sec. III.

I. ALTERNATIVE DERIVATION OF THE CUMULANT FUNCTION IN THE CE METHOD

In Sec. XI of the Supplemental Material in Ref. [S1], we showed that the Green's function, if there is only a single electron in the band, can be written as

$$G_{\mathbf{k}}(t) = -i\theta(t)\langle c_{\mathbf{k}}(t)c_{\mathbf{k}}^{\dagger}\rangle_{T,0}, \tag{S1}$$

where:

$$c_{\mathbf{k}}(t) = e^{iHt}c_{\mathbf{k}}e^{-iHt}, \tag{S2a}$$

$$H = H_{\text{el}} + H_{\text{ph}} + H_{\text{el}-\text{ph}}, \tag{S2b}$$

$$H_{\text{el}} = -t_0 \sum_{\langle ij\rangle}\left(c_i^{\dagger}c_j + \text{H.c.}\right) = \sum_{\mathbf{k}}\varepsilon_{\mathbf{k}}c_{\mathbf{k}}^{\dagger}c_{\mathbf{k}}, \tag{S2c}$$

$$H_{\text{ph}} = \omega_0 \sum_i a_i^{\dagger}a_i = \omega_0 \sum_{\mathbf{k}}a_{\mathbf{k}}^{\dagger}a_{\mathbf{k}}, \tag{S2d}$$

$$\begin{aligned}H_{\text{el}-\text{ph}} &= -g\sum_i c_i^{\dagger}c_i\left(a_i^{\dagger}+a_i\right)\\ &= -\frac{g}{\sqrt{N}}\sum_{\mathbf{k},\mathbf{q}}c_{\mathbf{k}+\mathbf{q}}^{\dagger}c_{\mathbf{k}}\left(a_{\mathbf{q}}+a_{-\mathbf{q}}^{\dagger}\right).\end{aligned} \tag{S2e}$$

Here, N is the number of sites (we take $N \to \infty$ in order to get the thermodynamic limit), while $\langle\ldots\rangle_{T,0}$ denotes the thermal average over the states with no electrons

and arbitrary number of phonons

$$\langle x\rangle_{T,0} = \frac{\sum_{\{n_p\}}\langle 0,\tilde{n}_p|e^{-H_{\text{ph}}/T}x|0,\tilde{n}_p\rangle}{\sum_{\{n_p\}}\langle 0,\tilde{n}_p|e^{-H_{\text{ph}}/T}|0,\tilde{n}_p\rangle}. \tag{S3}$$

For the rest of this section, an arbitrary state with n_p phonons and no electrons (since such state is not unique) will be denoted by $|0,\tilde{n}_p\rangle$, while $\sum_{\{n_p\}}$ represents the sum over all possible phonon configurations. We also introduce $|\mathbf{k},\tilde{n}_p\rangle \equiv c_{\mathbf{k}}^{\dagger}|0,\tilde{n}_p\rangle$ and $Z_{\text{ph}} = \sum_{\{n_p\}}\langle 0,\tilde{n}_p|e^{-H_{\text{ph}}/T}|0,\tilde{n}_p\rangle$.

Using the fact that $|0,\tilde{n}_p\rangle$ is an eigenstate of both the full and the phononic Hamiltonian $H|0,\tilde{n}_p\rangle = H_{\text{ph}}|0,\tilde{n}_p\rangle = n_p\omega_0|0,\tilde{n}_p\rangle$, we see how Eq. (S1) can be written in a more explicit form

$$G_{\mathbf{k}}(t) = \frac{-i\theta(t)}{Z_{\text{ph}}}\sum_{\{n_p\}}e^{i\omega_0 n_p t}e^{-n_p\omega_0/T}\langle 0,\tilde{n}_p|c_{\mathbf{k}}e^{-iHt}c_{\mathbf{k}}^{\dagger}|0,\tilde{n}_p\rangle. \tag{S4}$$

The term e^{-iHt} can be read off from

$$e^{iH_{\text{el}}t}e^{iH_{\text{ph}}t}e^{-iHt} = T_t\exp\left[-i\int_0^t dt_1 H_{\text{el}-\text{ph}}^{(I)}(t_1)\right], \tag{S5}$$

which represents two different, but equivalent, forms for the evolution operator in the Dirac picture. Here, $H_{\text{el}-\text{ph}}^{(I)}$ is the electron-phonon interaction part of the Hamiltonian in the Dirac picture and T_t is the time-ordering operator. For the purely phononic part $e^{-iH_{\text{ph}}t}$ we use $\langle 0,\tilde{n}_p|e^{-iH_{\text{ph}}t} = e^{-i\omega_0 n_p t}\langle 0,\tilde{n}_p|$, while purely electronic part $e^{-iH_{\text{el}}t}$ is dealt with analogously $\langle 0,\tilde{n}_p|c_{\mathbf{k}}e^{-iH_{\text{el}}t} = e^{-i\varepsilon_{\mathbf{k}}t}\langle 0,\tilde{n}_p|c_{\mathbf{k}}$. Hence, Eq. (S4) becomes

$$G_{\mathbf{k}}(t) = -\frac{i\theta(t)}{Z_{\text{ph}}}e^{-i\varepsilon_{\mathbf{k}}t}\sum_{\{n_p\}}e^{-n_p\omega_0/T}\left\langle 0,\tilde{n}_p\left|c_{\mathbf{k}}T_t\exp\left[-i\int_0^t dt_1 H_{\text{el}-\text{ph}}^{(I)}(t_1)\right]c_{\mathbf{k}}^{\dagger}\right|0,\tilde{n}_p\right\rangle \tag{S6a}$$

$$\equiv -i\theta(t)e^{-i\varepsilon_{\mathbf{k}}t}\left\langle T_t e^{-i\int_0^t dt_1 H_{\text{el}-\text{ph}}^{(I)}(t_1)}\right\rangle_{T,\mathbf{k}}. \tag{S6b}$$

The expressions of the form (S6b) have been extensively studied in the past. As shown in Eq. (6.10) of Kubo's cu-

mulant paper [S2], the expectation value with the time-ordering can be written as

$$\left\langle T_t e^{-i\int_0^t dt_1 H_{\text{el-ph}}^{(I)}(t_1)}\right\rangle_{T,\mathbf{k}} = \exp\left\langle T_t e^{-i\int_0^t dt_1 H_{\text{el-ph}}^{(I)}(t_1)} - 1\right\rangle_{T,\mathbf{k},c} \equiv e^{C_\mathbf{k}(t)}, \tag{S7}$$

where we defined the cumulant function $C_\mathbf{k}(t)$. The notation $\langle\ldots\rangle_c$ denotes the so-called cumulant average. For our present purposes, we only need to know how the first two cumulant averages are defined:

$$\langle X_1\rangle_c = \langle X_1\rangle \tag{S8a}$$
$$\langle X_1 X_2\rangle_c = \langle X_1 X_2\rangle - \langle X_1\rangle\langle X_2\rangle. \tag{S8b}$$

In general, the cumulant average is defined using the ordinary average, by formally expanding the following expression in the Taylor series with respect to ξ_i and equating, order by order, the terms on the left- and the right-hand side

$$\left\langle \exp\sum_j \xi_j X_j\right\rangle = \exp\left\langle\left(\exp\sum_j \xi_j X_j\right) - 1\right\rangle_c. \tag{S9}$$

The -1 term on the right-hand side is motivated by the fact that the expectation value of the unity operator is equal to 1. While our paper focuses on the cumulant of the second order, there is actually an analytic formula that relates the cumulant average of any order with the

ordinary average [S3].

Let us now go back to Eq. (S6b) and use Eq. (S7) to obtain

$$G_\mathbf{k}(t) = -i\theta(t)e^{-i\varepsilon_\mathbf{k} t}e^{C_\mathbf{k}(t)}, \tag{S10}$$

where

$$C_\mathbf{k}(t) = \sum_{j=1}^{\infty}\left\langle T_t \frac{(-i)^j}{j!}\int_0^t \prod_{m=1}^{j} dt_m H_{\text{el-ph}}^{(I)}(t_m)\right\rangle_{T,\mathbf{k},c}. \tag{S11}$$

So far, everything was exact. The approximation, that we now introduce, consists of keeping only the first two terms in the previous equation ($j=1$ and $j=2$ terms) while neglecting everything else. This is known as the second-order cumulant expansion. In the $j=1$ term, the cumulant average coincides with the ordinary average (see Eq. (S8a)), and hence vanishes due to Wick's theorem. As a consequence, the cumulant average can be simply replaced by the ordinary average in the case of $j=2$ term as well; see Eq. (S8b). Therefore, the second-order cumulant function reads as

$$C_\mathbf{k}(t) = -\frac{1}{2}\int_0^t dt_1 \int_0^t dt_2 \left\langle T_t c_\mathbf{k} H_{\text{el-ph}}^{(I)}(t_1) H_{\text{el-ph}}^{(I)}(t_2) c_\mathbf{k}^\dagger\right\rangle_{T,0}. \tag{S12}$$

For a straightforward application of Wick's theorem, it is customary to rewrite electron creation and annihilation operators in the Dirac picture. In order not to change the already existing time ordering in Eq. (S12), the annihilation operator is expressed in the final time

$c_\mathbf{k} = e^{i\varepsilon_\mathbf{k} t}c_\mathbf{k}^{(I)}(t)$, while the creation operator is expressed in the initial time $c_\mathbf{k}^\dagger = c_\mathbf{k}^{\dagger(I)}(0)$. If we also use the explicit form of $H_{\text{el-ph}}^{(I)}(t)$ from Eq. (S2e), the Eq. (S12) becomes

$$C_\mathbf{k}(t) = -\frac{g^2}{2N}e^{i\varepsilon_\mathbf{k} t}\int_0^t dt_1 \int_0^t dt_2 \left\langle T_t c_\mathbf{k}^{(I)}(t)\sum_{\mathbf{k_1},\mathbf{q_1}} c_{\mathbf{k_1}+\mathbf{q_1}}^{\dagger(I)}(t_1)c_{\mathbf{k_1}}^{(I)}(t_1)A_{\mathbf{q_1}}^{(I)}(t_1)\sum_{\mathbf{k_2},\mathbf{q_2}} c_{\mathbf{k_2}+\mathbf{q_2}}^{\dagger(I)}(t_2)c_{\mathbf{k_2}}^{(I)}(t_2)A_{\mathbf{q_2}}^{(I)}(t_2)c_\mathbf{k}^{\dagger(I)}(0)\right\rangle_{T,0}, \tag{S13}$$

where we introduced the shorthand notation for the phonon part $A_\mathbf{q} = a_\mathbf{q} + a_{-\mathbf{q}}^\dagger$. Eq. (S13) is now straightforwardly evaluated using Wick's theorem. Contraction between the phonon degrees of freedom gives [S4]

$$\left\langle T_t A_{\mathbf{q_1}}^{(I)}(t_1)A_{\mathbf{q_2}}^{(I)}(t_2)\right\rangle = \delta_{\mathbf{q_1},-\mathbf{q_2}}iD(t_1-t_2), \tag{S14}$$

where $iD(t_1-t_2) = (n_{ph}+1)e^{-i\omega_0|t_1-t_2|} + n_{ph}e^{i\omega_0|t_1-t_2|}$ is the phonon propagator, while $n_{ph} = 1/(e^{\omega_0/T}-1)$ is the Bose factor. Since we are working in the limit of vanishing electron density (single electron in a band), the contraction between the electron creation and annihilation operators does not have a hole part, and hence

reads as

$$\left\langle T_t c_{\mathbf{k}}^{(I)}(t_1) c_{\mathbf{q}}^{\dagger(I)}(t_2) \right\rangle = \delta_{\mathbf{k},\mathbf{q}} \, e^{-i\varepsilon_{\mathbf{k}}|t_1-t_2|}\theta(t_1-t_2). \quad \text{(S15)}$$

Taking all of this into account, Eq. (S13) simplifies

$$C_{\mathbf{k}}(t) = -\frac{g^2}{2N}\sum_{\mathbf{q}}\int_0^t dt_1 \int_0^t dt_2 e^{i(\varepsilon_{\mathbf{k}}-\varepsilon_{\mathbf{q}})|t_2-t_1|}iD(t_2-t_1).$$
(S16)

We can get rid of the absolute value by noticing that the contributions for $t_2 > t_1$ and for $t_2 < t_1$ are equal. It is thus sufficient to restrict ourselves to $t_2 > t_1$ and multiply everything by 2. Also, the expression can be further simplified if we use

$$e^{i(\varepsilon_{\mathbf{k}}-\varepsilon_{\mathbf{q}}\pm\omega_0)(t_2-t_1)} = \int_{-\infty}^{\infty} d\omega e^{-i\omega(t_2-t_1)}\delta(\omega+\varepsilon_{\mathbf{k}}-\varepsilon_{\mathbf{q}}\pm\omega_0).$$

Then, the whole $\mathbf{q}$ dependence is inside the Dirac delta function, which in combination with the summation over $\mathbf{q}$ gives

$$\sum_{\mathbf{q}}\delta(\omega + \varepsilon_{\mathbf{k}} - \varepsilon_{\mathbf{q}} \pm \omega_0) = N\rho(\omega + \varepsilon_{\mathbf{k}} \pm \omega_0), \quad \text{(S17)}$$

where ρ is the density of states. It is now straightforward to show that Eq. (S16) reduces to

$$C_{\mathbf{k}}(t) = g^2 \int_{-\infty}^{\infty} d\omega \frac{e^{-i\omega t} + i\omega t - 1}{\omega^2}$$
$$\times \left[(n_{ph}+1)\rho(\omega + \varepsilon_{\mathbf{k}} - \omega_0) + n_{ph}\rho(\omega + \varepsilon_{\mathbf{k}} + \omega_0)\right].$$
(S18)

This expression can be rewritten in terms of the Migdal self-energy (see Eq. (14) from the main text) as follows

$$C_{\mathbf{k}}(t) = \frac{1}{\pi}\int_{-\infty}^{\infty} d\omega \frac{|\text{Im}\Sigma^{\text{MA}}(\omega + \varepsilon_{\mathbf{k}})|}{\omega^2}(e^{-i\omega t} + i\omega t - 1).$$
(S19)

Hence, we gave an alternative derivation of the cumulant function $C_{\mathbf{k}}(t)$, where the self-energy in the Migdal approximation emerges more explicitly than in Eq. (7) of the main text.

We note that the cumulant expansion method that we have now presented is analogous to the linked cluster expansion for the thermodynamic potential F in statistical mechanics. This is a consequence of the same mathematical form of $C_{\mathbf{k}}(t) = \ln\left(G_{\mathbf{k}}(t)/G_{\mathbf{k},0}(t)\right)$ and $F = \ln(Z/Z_0)$, where Z and Z_0 are the partition function of the full and noninteracting theories.

II. SPECTRAL FUNCTIONS

In Sec. III of the main text, we presented spectral functions $A(\omega)$ and heat maps for $\omega_0 = 0.5$. Here, we present a large number of results for $\omega_0 = 1$, $\omega_0 = 0.2$, as well as some additional results for $\omega_0 = 0.5$ that are organized as follows:

FIG. S1. (a)–(e) Comparison of CE, DMFT, and SCMA spectral functions in the weak coupling regime, for a wide range of temperatures. Here $t_0 = \omega_0 = 1$ and $\alpha = 0.5$.
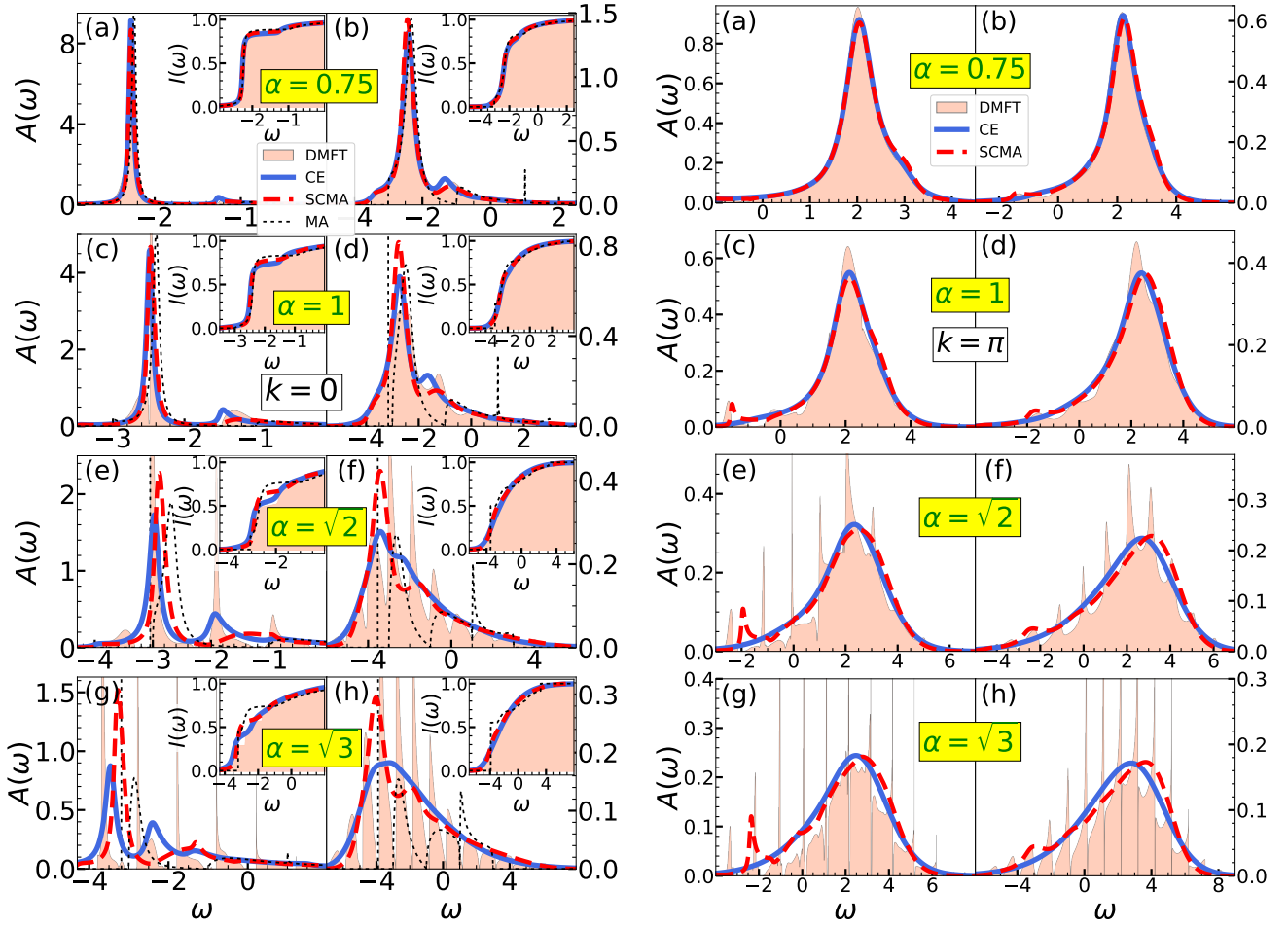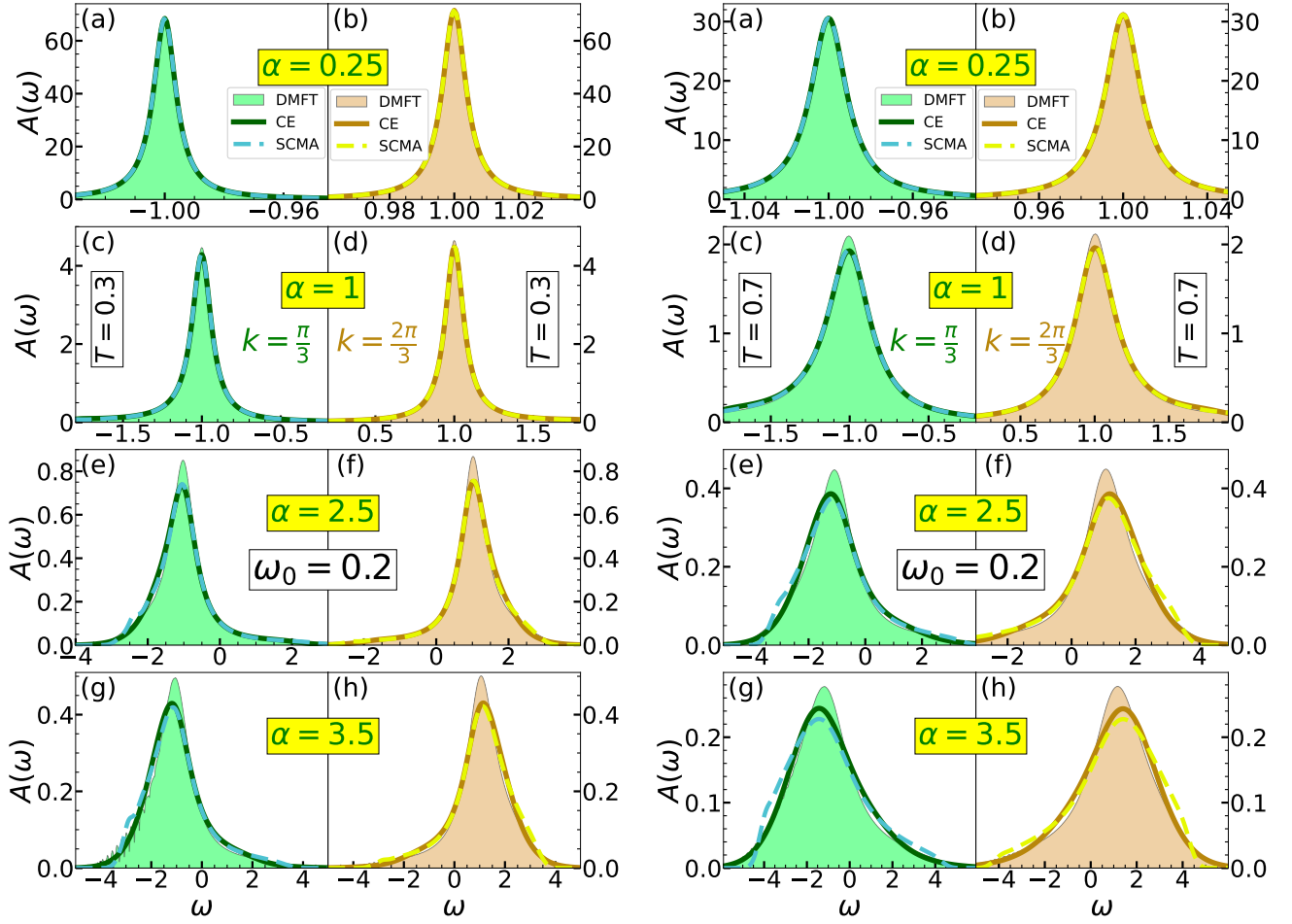
(i) (a)–(h) Spectral functions for $\omega_0 = 1$ and $k = 0$. In the left panels $T = 0.4$, while $T = 1$ in the right panels. Insets show the integrated spectral weights $I(\omega) = \int_{-\infty}^{\infty} A(\omega)d\omega$.

(ii) (a)–(h) Spectral functions for $\omega_0 = 1$ and $k = \pi$. In the left panels $T = 0.4$, while $T = 1$ in the right panels. Insets show the integrated spectral weights $I(\omega) = \int_{-\infty}^{\infty} A(\omega)d\omega$.
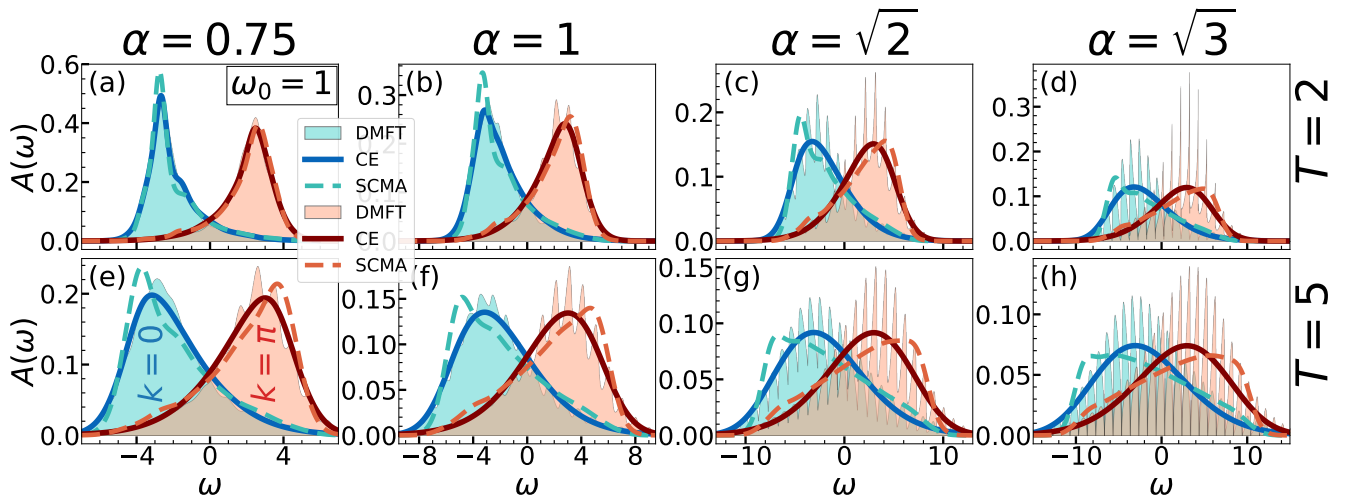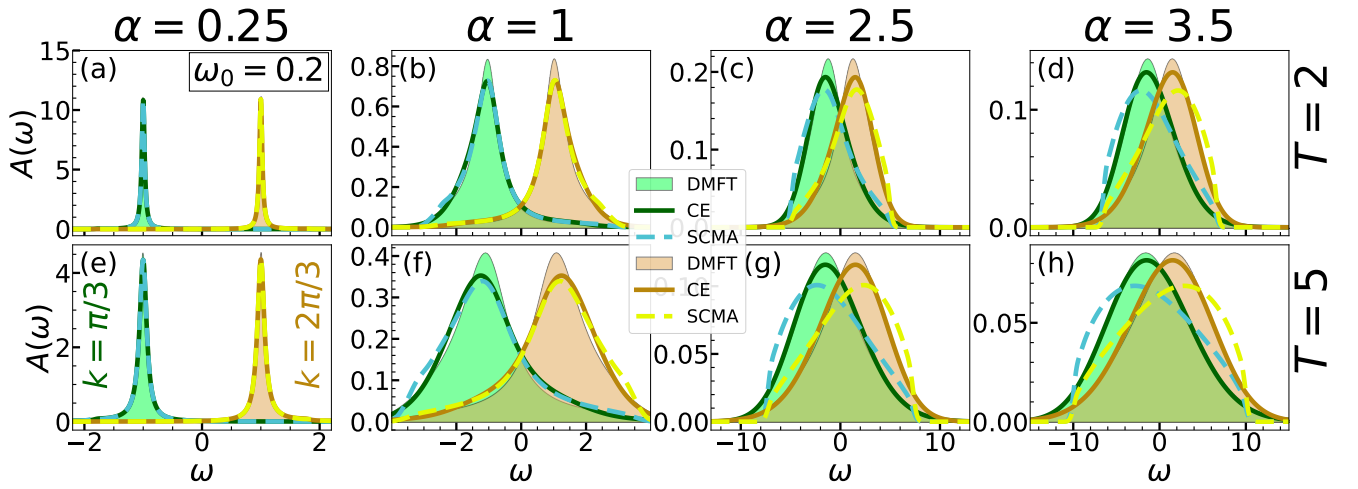
(iii) Spectral functions at higher temperatures for $\omega_0 = 1$ and $k = 0, \pi$.

FIG. S2. Comparison of the CE, DMFT, SCMA, and MA spectral functions in 1D for $t_0 = \omega_0 = 1$.
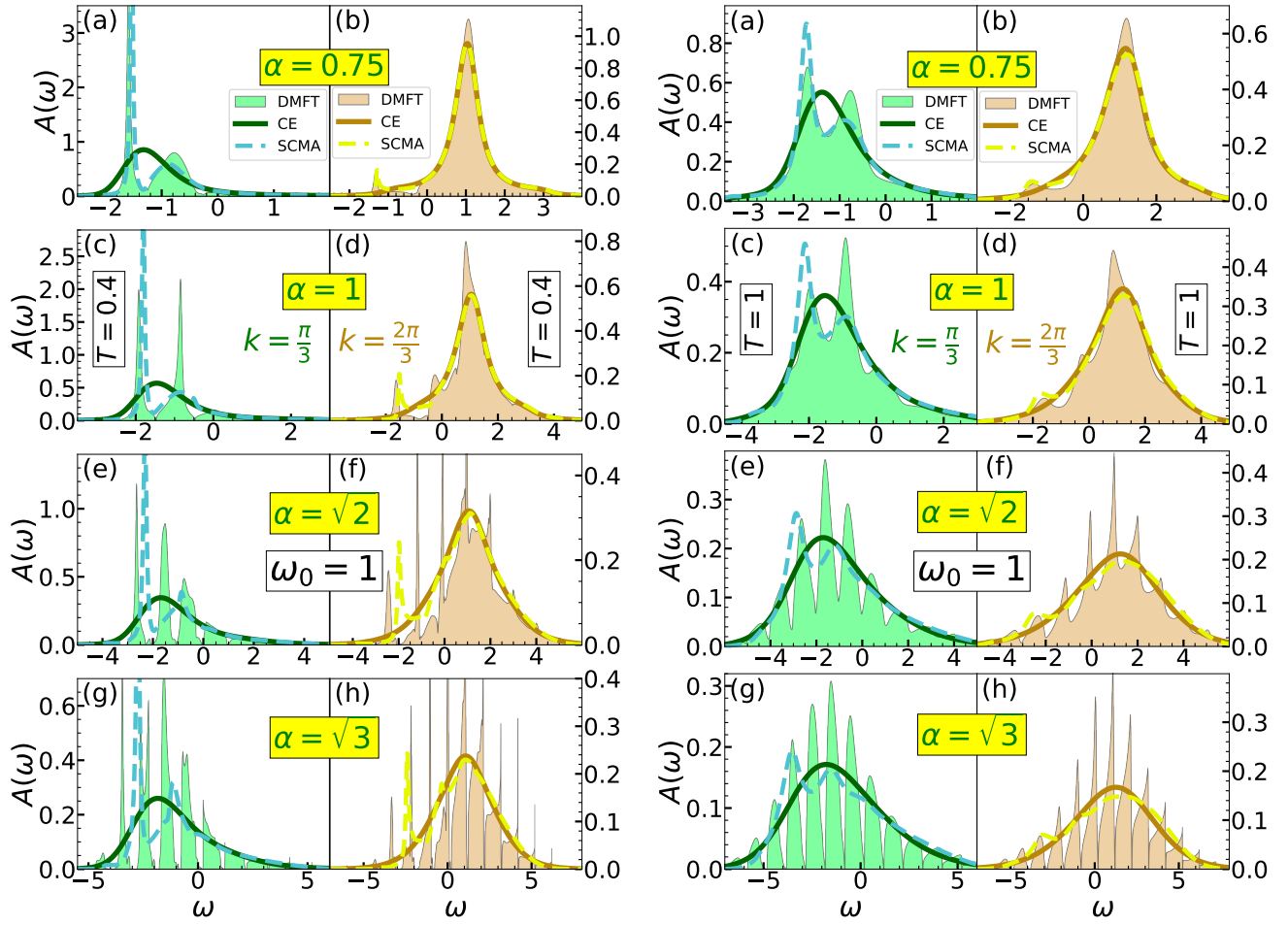
(i) (a)–(h) Spectral functions for $\omega_0 = 1$ and $T = 0.4$. In the left panels $k = \pi/3$, while $k = 2\pi/3$ in the right panels.

(ii) (a)–(h) Spectral functions for $\omega_0 = 1$ and $T = 1$. In the left panels $k = \pi/3$, while $k = 2\pi/3$ in the right panels.
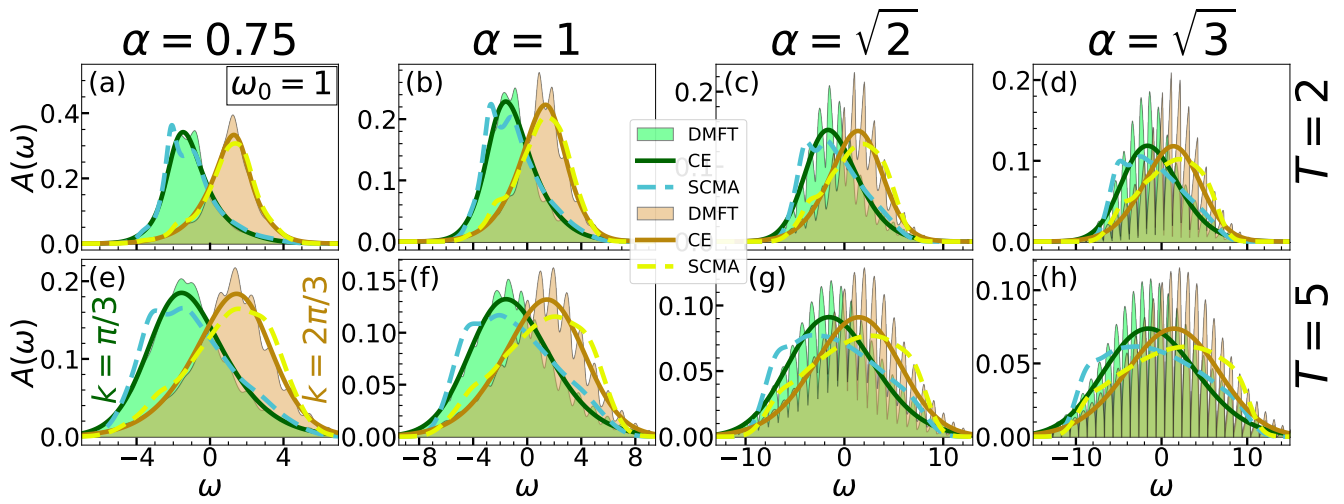
(iii) Spectral functions at higher temperatures for $\omega_0 = 1$ and $k = \pi/3, 2\pi/3$.

FIG. S3. Comparison of the CE, DMFT, and SCMA spectral functions in 1D for $t_0 = \omega_0 = 1$ and $k = \pi/3, 2\pi/3$.
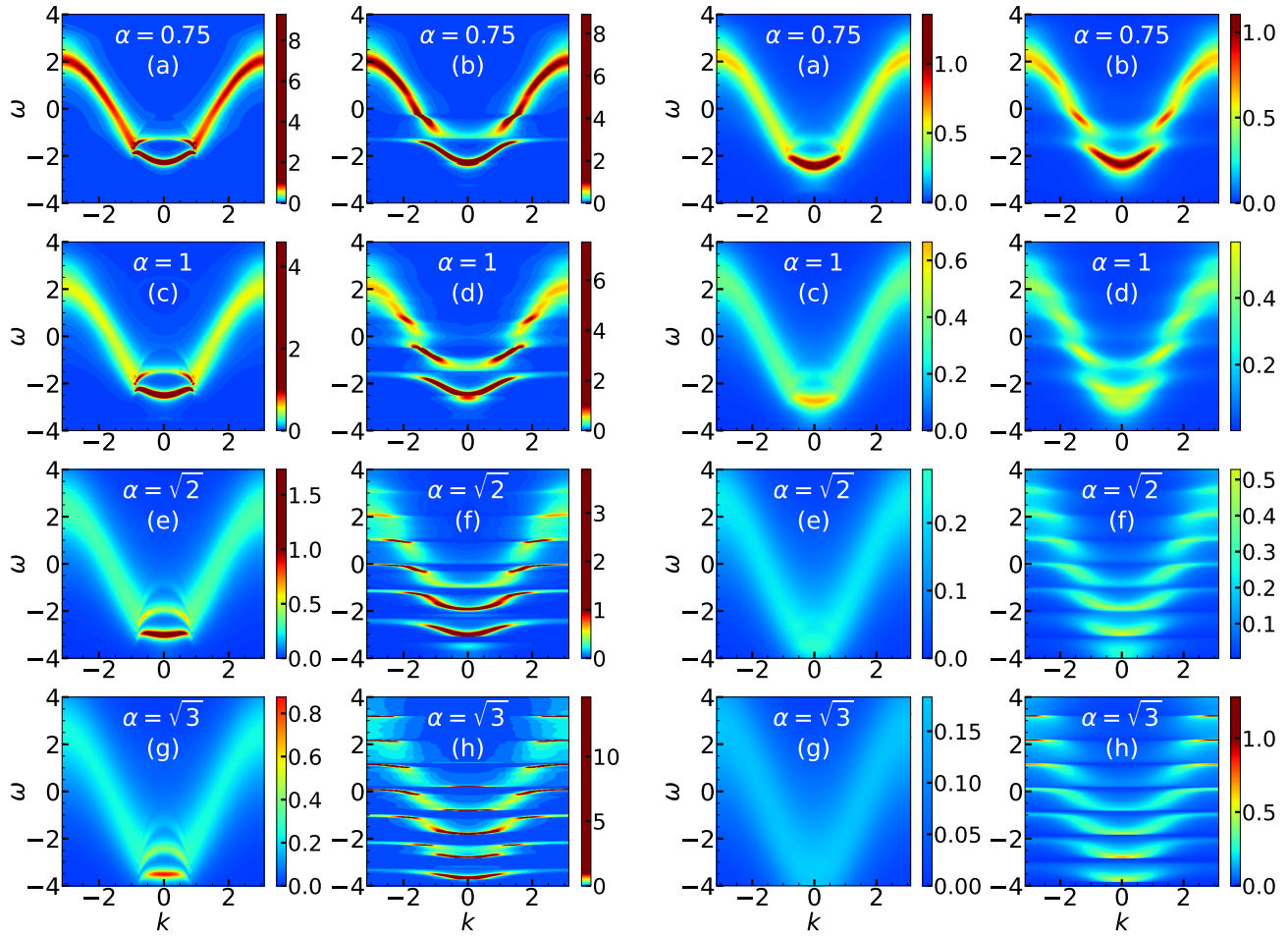
(i) (a)–(h) Heat maps for $T = 0.4$. In the left panels, we present CE results, while the DMFT benchmark is presented in the right panels. All plots use the same color coding.

(ii) (a)–(h) Heat maps for $T = 1$. In the left panels, we present CE results, while the DMFT benchmark is presented in the right panels. All plots use the same color coding.

FIG. S4. Comparison of the CE and DMFT heat maps for $t_0 = \omega_0 = 1$.
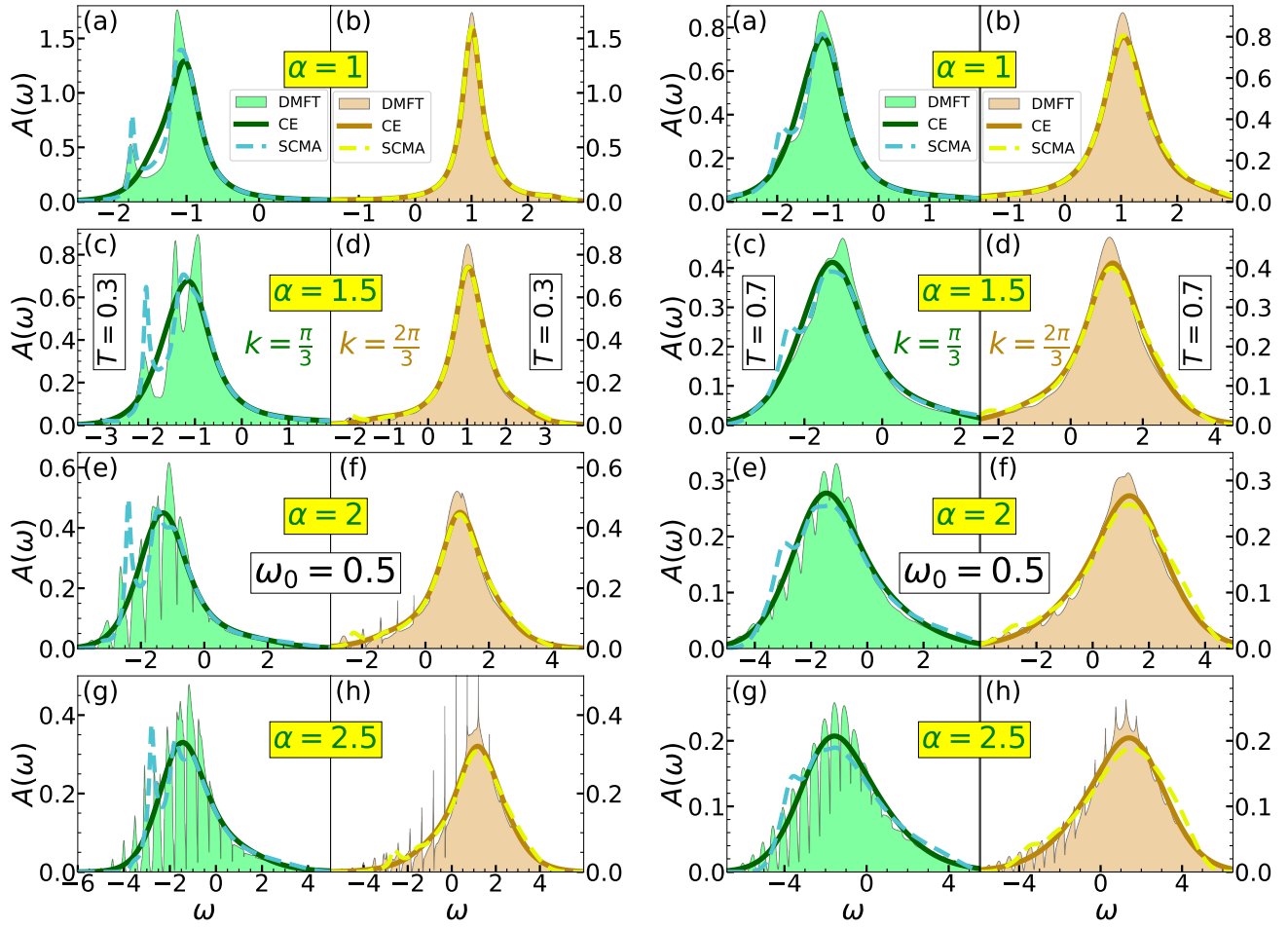
(i) (a)–(h) Spectral functions for $\omega_0 = 0.5$ and $T = 0.3$. In the left panels $k = \pi/3$, while $k = 2\pi/3$ in the right panels.

(ii) (a)–(h) Spectral functions for $\omega_0 = 0.5$ and $T = 0.7$. In the left panels $k = \pi/3$, while $k = 2\pi/3$ in the right panels.
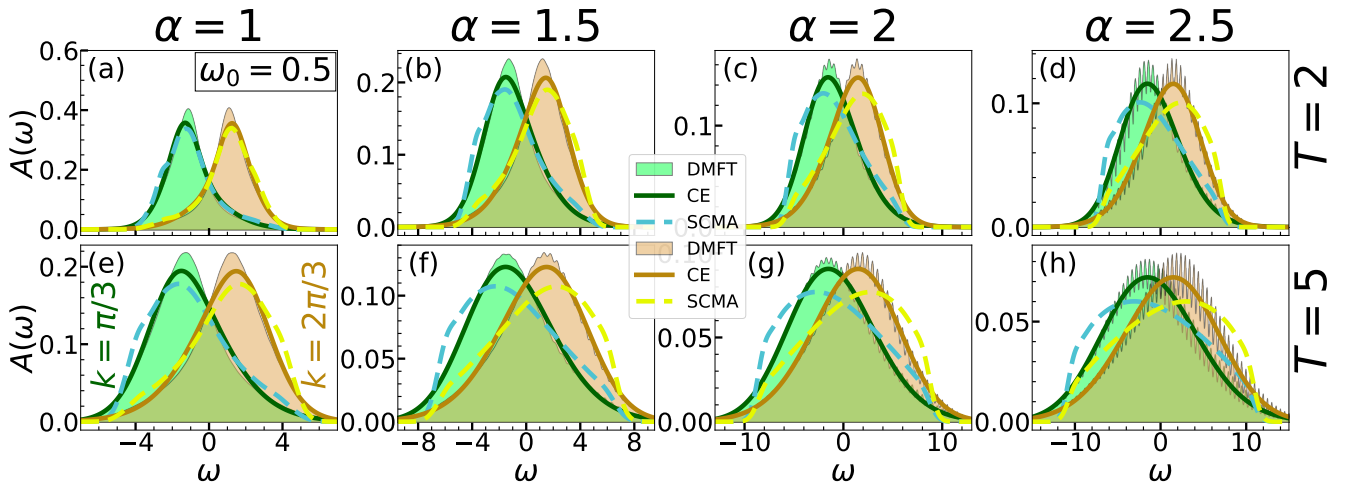
(iii) Spectral functions at higher temperatures for $\omega_0 = 0.5$ and $k = \pi/3, 2\pi/3$.

FIG. S5. Comparison of the CE, DMFT, and SCMA spectral functions in 1D for $t_0 = 1$, $\omega_0 = 0.5$ and $k = \pi/3, 2\pi/3$.

9
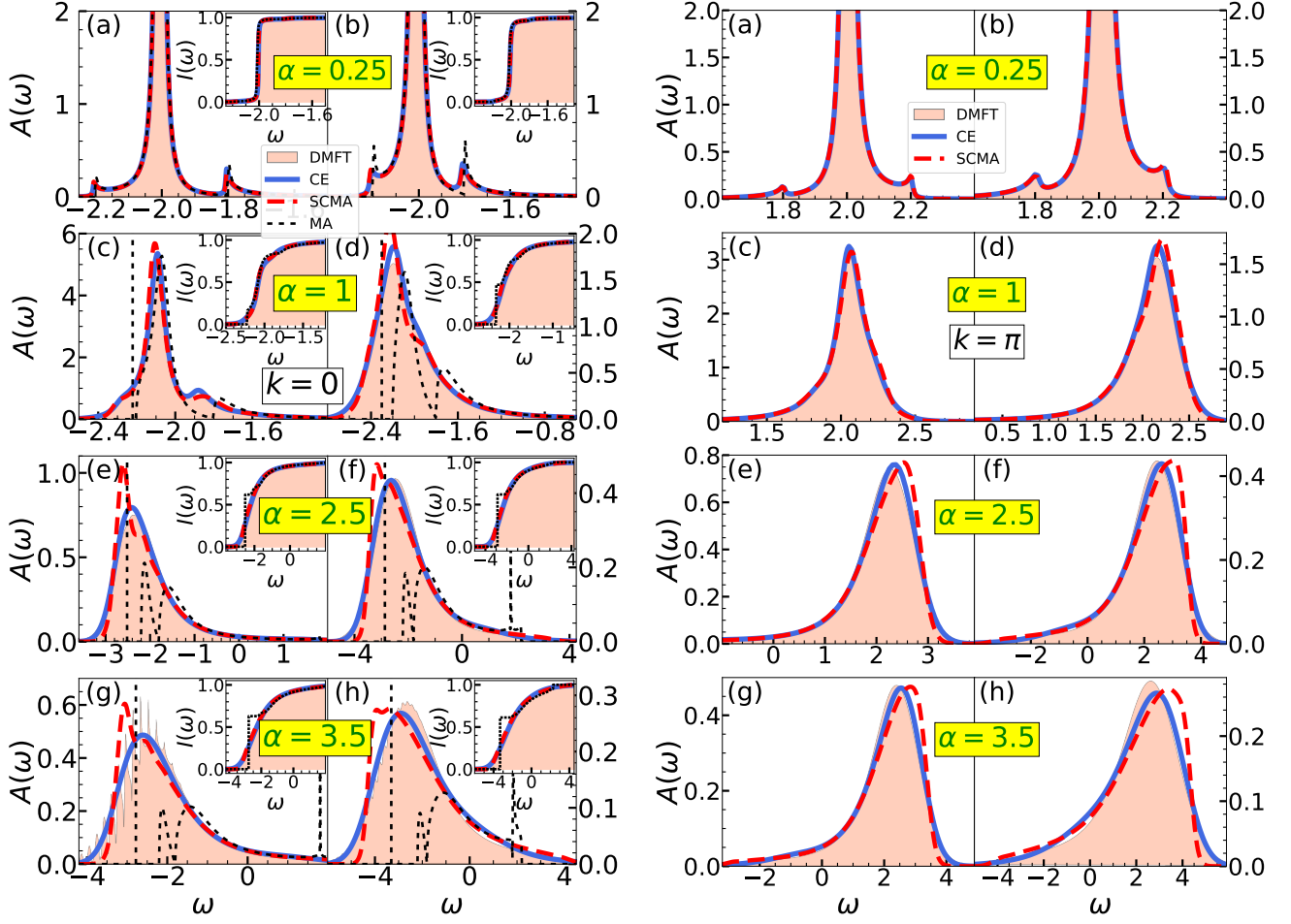
(i) (a)–(h) Spectral functions for $\omega_0 = 0.2$ and $k = 0$. In the left panels $T = 0.3$, while $T = 0.7$ in the right panels. Insets show the integrated spectral weight $I(\omega) = \int_{-\infty}^{\infty} A(\omega)d\omega$.

(ii) (a)–(h) Spectral functions for $\omega_0 = 0.2$ and $k = \pi$. In the left panels $T = 0.3$, while $T = 0.7$ in the right panels. Insets show the integrated spectral weight $I(\omega) = \int_{-\infty}^{\infty} A(\omega)d\omega$.
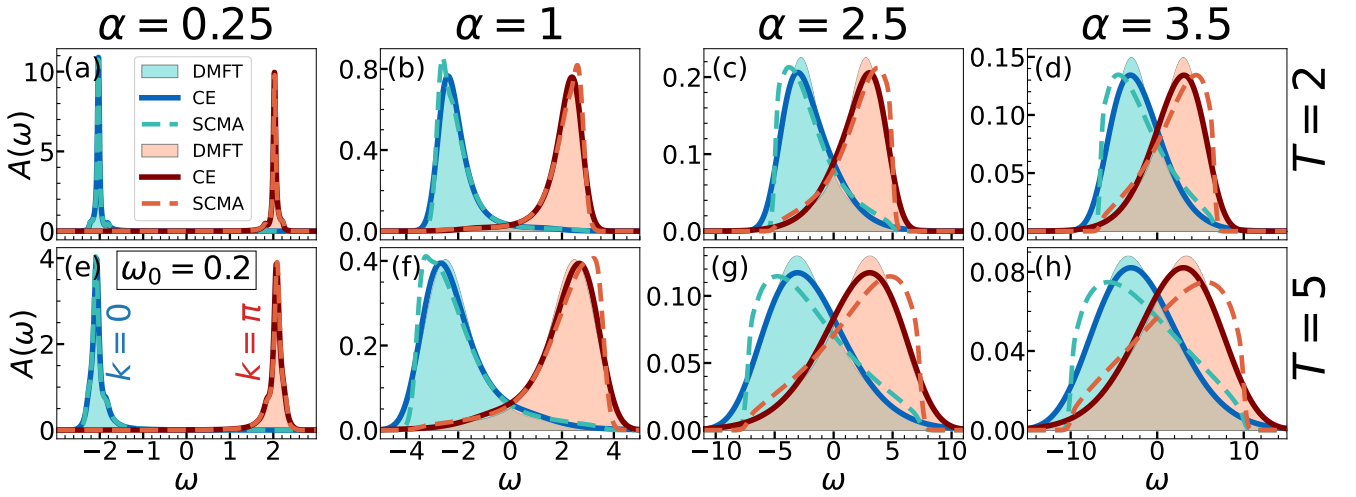
(iii) Spectral functions at higher temperatures for $\omega_0 = 0.2$ and $k = 0, \pi$.

FIG. S6. Comparison of the CE, DMFT, SCMA, and MA spectral functions in 1D for $t_0 = 1$, $\omega_0 = 0.2$, and $k = 0, \pi$.

(i) (a)–(h) Spectral functions for $\omega_0 = 0.2$ and $T = 0.3$. In the left panels $k = \pi/3$, while $k = 2\pi/3$ in the right panels.

(ii) (a)–(h) Spectral functions for $\omega_0 = 0.2$ and $T = 0.7$. In the left panels $k = \pi/3$, while $k = 2\pi/3$ in the right panels.

(iii) Spectral functions at higher temperatures for $\omega_0 = 0.2$ and $k = \pi/3, 2\pi/3$.

FIG. S7. Comparison of the CE, DMFT, and SCMA spectral functions in 1D for $t_0 = 1$, $\omega_0 = 0.2$ and $k = \pi/3, 2\pi/3$.

10
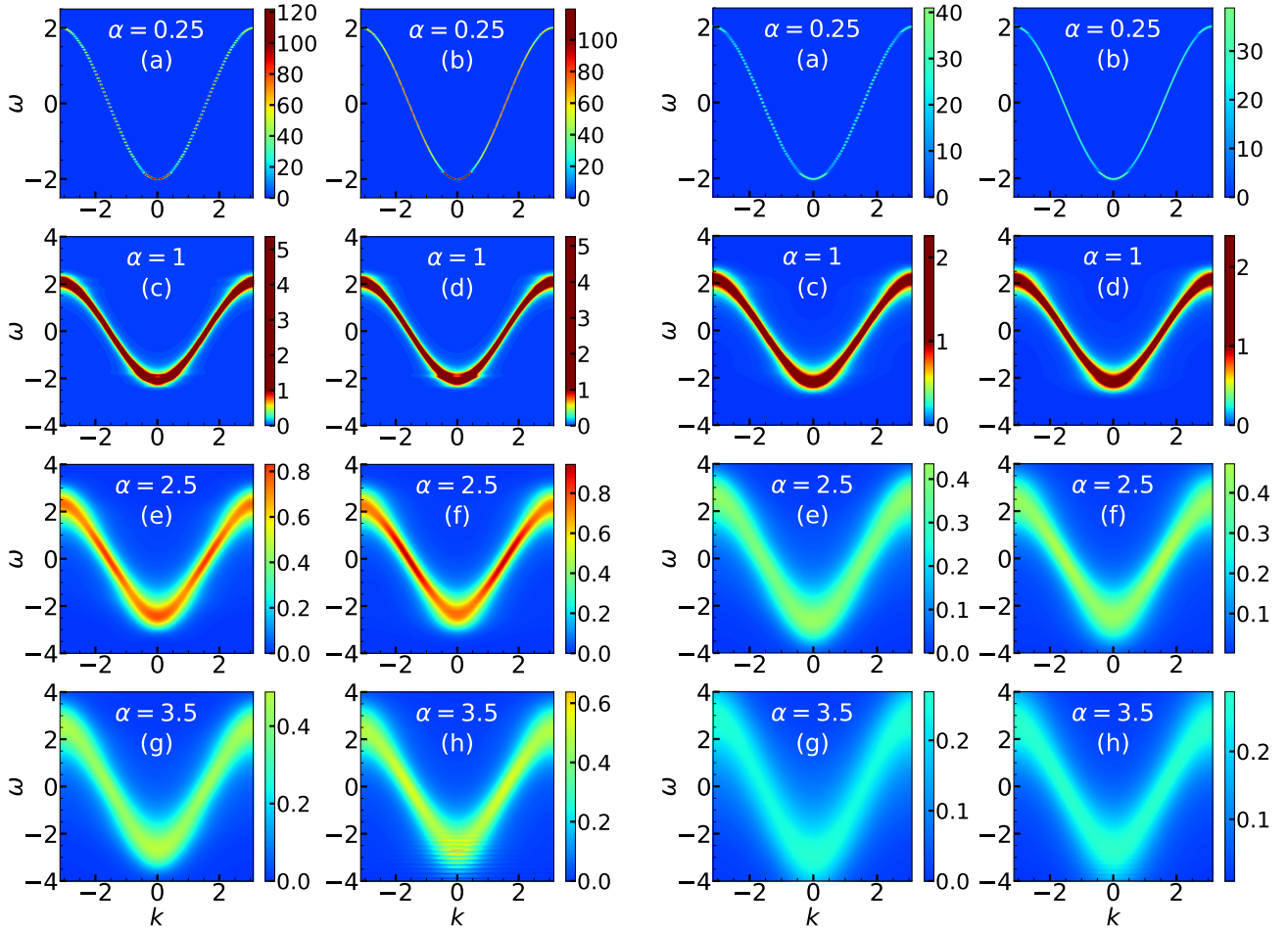
(i)   (a)–(h) Heat maps for $T = 0.3$. In the left panels, we present CE results, while the DMFT benchmark is presented in the right panels. Panels (c)–(h) use the same color coding, while panels (a) and (b) use different color coding.

(ii)   (a)–(h) Heat maps for $T = 0.7$. In the left panels, we present CE results, while the DMFT benchmark is presented in the right panels. Panels (c)–(h) use the same color coding, while panels (a) and (b) use different color coding.

FIG. S8. Comparison of the CE and DMFT heat maps for $t_0 = 1$ and $\omega_0 = 0.2$.

III.   QUASIPARTICLE PROPERTIES

In Sec. IV of the main text, we showed and analyzed the quasiparticle properties of CE, DMFT, and SCMA methods. Here we supplement that study by including the predictions of the Migdal approximation for the ground state energy in 1D. The results are shown in Fig. S9. We emphasize that the predictions of the DMFT benchmark are practically identical to the exact numerical results [S1]. These results readily demonstrate how much improvement to the simplest approximation (MA) is provided by including the self-consistency (SCMA) and by employing the cumulant expansion method (CE).
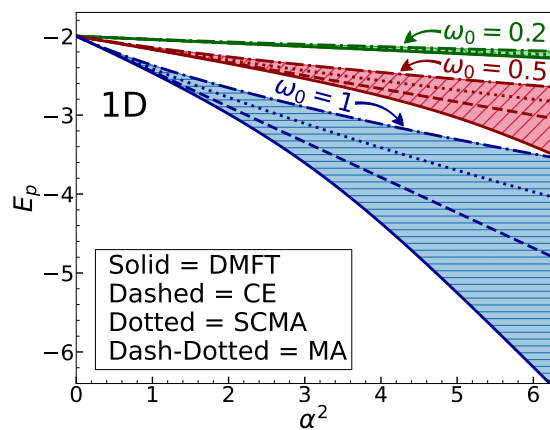
FIG. S9. Ground state energy within DMFT, CE, SCMA, and MA for the one-dimensional Holstein model with $t_0 = 1$.

[S1] P. Mitrić, V. Janković, N. Vukmirović, and D. Tanasković, Spectral Functions of the Holstein Polaron: Exact and Approximate Solutions, Phys. Rev. Lett. **129**, 096401 (2022).

[S2] R. Kubo, Generalized Cumulant Expansion Method, Journal of the Physical Society of Japan **17**, 1100 (1962).

[S3] E. Meeron, Series expansion of distribution functions in multicomponent fluid systems, The Journal of Chemical Physics **27**, 1238 (1957).

[S4] G. Mahan, *Many-Particle Physics* (Kluwer Academic, New York, 2000).

Optical conductivity and vibrational spectra of the narrow-gap semiconductor FeGa₃

C. Martin [1] V. A. Martinez,[2] M. Opačić [3] S. Djurdjić-Mijin [3] P. Mitrić [3] A. Umićević [4] A. Poudel [1] I. Sydoryk [1]
Weijun Ren [5,6] R. M. Martin [7] D. B. Tanner [2] N. Lazarević [3] C. Petrovic [5] and D. Tanasković [3]

[1]*School of Theoretical and Applied Sciences, Ramapo College of New Jersey, Mahwah, New Jersey 07430, USA*
[2]*Department of Physics, University of Florida, Gainesville, Florida 32611, USA*
[3]*Institute of Physics Belgrade, University of Belgrade, Pregrevica 118, 11080 Belgrade, Serbia*
[4]*Vinča Institute of Nuclear Sciences, National Institute of the Republic of Serbia, University of Belgrade,*
P.O. Box 522, 11001 Belgrade, Serbia
[5]*Condensed Matter Physics and Materials Science Department, Brookhaven National Laboratory, Upton, New York 11973, USA*
[6]*Shenyang National Laboratory for Materials Science, Institute of Metal Research, Chinese Academy of Sciences, Shenyang 110016, China*
[7]*Department of Physics and Astronomy, Montclair State University, Montclair, New Jersey 07043, USA*

Intermetallic narrow-gap semiconductors have been intensively explored due to their large thermoelectric power at low temperatures and a possible role of strong electronic correlations in their unusual thermodynamic and transport properties. Here we study the optical spectra and vibrational properties of FeGa₃ single crystal. The optical conductivity indicates that FeGa₃ has a direct band gap of ≈ 0.7 eV, consistent with density functional theory (DFT) calculations. Most importantly, we find a substantial spectral weight also below 0.4 eV, which is the energy of the indirect (charge) gap found in resistivity measurements and *ab initio* calculations. We find that the spectral weight below the gap decreases with increasing temperature, which indicates that it originates from the impurity states and not from the electronic correlations. Interestingly, we did not find any signatures of the impurity states in vibrational spectra. The infrared and Raman vibrational lines are narrow and weakly temperature dependent. The vibrational frequencies are in excellent agreement with our DFT calculations, implying a modest role of electronic correlations. Narrow Mössbauer spectral lines also indicate high crystallinity of the sample.

I. INTRODUCTION

Correlated narrow-gap semiconductors represent a class of materials known for their large thermopower at low temperatures and other anomalous transport and thermodynamic properties [1]. Three iron compounds among them, FeSi, FeSb₂, and FeGa₃, share some common features, but also show important differences. FeSi and FeSb₂ behave as insulators only at temperatures $T^* \lesssim 100$ K which corresponds to the energy much smaller than the band gap $E_g \approx 50$ meV [2–4]. A buildup of the in-gap spectral weight at temperatures $k_B T^* \ll E_g$, clearly seen in optical [5–8] and photoemission spectroscopy [9], is a signature of strong electronic correlations [10,11]. A crossover from a nonmagnetic insulator to a bad metal is accompanied by a large increase in the spin susceptibility which obtains Curie-Weiss form above room temperature [12,13]. This crossover leaves fingerprints also in the Raman vibrational spectra which become strongly temperature dependent. The width of vibrational peaks increases several times in the bad-metal region as compared to the low-temperature insulating state [14–16]. At temperatures near 10 K there is a large peak in the thermopower $|S|$ [17,18]. The exact role of the electronic correlations, in-gap states, anisotropy, and phonon drag in colossal thermopower found in FeSb₂ remains a subject of various studies and controversy [19–21].

FeGa₃ has a significantly larger band gap, $E_g \approx 0.4$ eV [22,23], than FeSi and FeSb₂ due to the stronger hybridization between $3d$ orbitals of Fe and $4p$ orbitals of Ga. The electronic structure calculations imply modest contribution of electronic correlations. Density functional theory (DFT) [24] and LDA+U [23] calculations give almost the same band structure, while dynamical mean field theory (DFT+DMFT) [25] gives only slightly reduced band gap. Nevertheless, the temperature dependence of dc resistivity is nontrivial: it strongly deviates from a simple activated transport at low temperatures, and features four distinct transport regimes which are associated with a presence of the in-gap states [22,23,25]. For $T \lesssim 5$ K ρ_{dc} has a power law temperature dependence consistent with the variable-range hopping transport driven by the localized in-gap states. In the interval $20 \lesssim T \lesssim 45$ K the charge transport is activated, but corresponds to a small gap of ≈ 40 meV between the in-gap states and the conduction band. Then, following a minimum in ρ_{dc}, there is a metalliclike transport up to ≈ 80 K which presumably corresponds to the regime where most of the in-gap electrons are already transferred to the conduction band. For $T > 300$ K the charge transport is activated, consistent with the wide gap $E_g \approx 0.4$ eV. The measurements show weak sample anisotropy and weak temperature dependence of magnetic susceptibility, whereas the DFT+DMFT calculations give small mass renormalization, as well as strong charge and spin

fluctuations [25]. A maximum in the Seebeck coefficient $|S|$ at $T \approx 15$ K is argued to be a consequence of the phonon-drag effect [23]. In this picture the in-gap states supply free charge carriers and the acoustic phonons cause an additional scattering of the electrons opposite to the direction of a temperature gradient, leading to the large thermoelectric power. Interestingly, to our knowledge, there has been so far only one infrared spectroscopy study of $FeGa_3$ in polycrystalline samples [26], restricted to room temperature and energies larger than 90 meV.

In this paper, we present infrared and Raman spectroscopy study of $FeGa_3$ single crystal in the temperature range between 4 and 300 K. The reflectance is measured in the energy interval between 30 and 24 000 cm^{-1}. The infrared and Raman active vibrational frequencies are in excellent agreement with our DFT calculations, indicating good crystallinity and a small influence of electronic correlations. Good crystallinity is corroborated also by measured Mössbauer spectra. The most prominent feature of the optical spectra is the existence of the in-gap states below the charge gap of approximately 0.4 eV. We observe a reduction of the in-gap spectral weight as the temperature increases to 300 K and conclude that this spectral weight originates from the impurities. Details of experimental and numerical methods are presented in Sec. II. The results are shown in Secs. III and IV contains our conclusions.

II. METHODS

Single crystals of $FeGa_3$ were grown as described previously [22]. For infrared measurements a small crystal was polished until a smooth surface of about 3 mm^2 area was obtained, then mounted on a helium-flow optical cryostat. The temperature dependence of reflectance was measured between 30 and 24 000 cm^{-1}, using a combination of two Fourier-transform infrared spectrometers: a Bruker 113v for far infrared (30–600 cm^{-1}) and a Bruker Vertex 70, with extended spectral range, from midinfrared to visible (100–24 000 cm^{-1}). Reflectance in visible and ultraviolet (12 000–50 000 cm^{-1}) was measured at room temperature only, using a Perkin-Elmer 650 UV/VIS grating spectrometer. As no temperature dependence was observed above about 12 000 cm^{-1}, all temperatures were merged with room temperature data in visible and ultraviolet parts of the spectrum. To capture correctly the width and line shape of lattice vibrations, the far-IR data were taken with a resolution of 0.5 cm^{-1}, while 2 cm^{-1} or larger values were used at higher frequencies. Both gold and aluminum mirrors were used for reference, and in order to correct for surface roughness the sample was also gold coated, using a commercial Ted Pella Cressington 108 sputtering machine. Because of the polishing involved, the precise orientation of the electric field (polarization) with respect to the crystallographic axes of the samples is not clearly defined, hence we cannot discuss potential anisotropic optical properties.

Raman scattering measurements were performed using a TriVista557 Raman system, equipped with a nitrogen-cooled CCD detector, in backscattering micro-Raman configuration. Grating configuration was 1800/1800/2400 grooves/mm, in order to achieve the best possible resolution. The 514.5-nm line of an Ar+/Kr+ gas laser was used as an excitation source and a microscope objective with factor 50 magnification was used for focusing the beam. All measurements were carried out with laser power less than 1.5 mW at the sample, in order to minimize local heating. Room temperature measurements were done in air, whereas for low temperature measurements the sample was placed in a KONTI CryoVac continuous flow cryostat, with a 0.5-mm-thick window. Spectra were corrected for the Bose factor.

The ^{57}Fe-Mössbauer spectrum of the $FeGa_3$ powdered sample was measured at room temperature in high ($\approx \pm 9$ mm/s) and low ($\approx \pm 2$ mm/s) Doppler velocity range. The spectra were collected in standard transmission geometry in constant acceleration mode using a ^{57}Co(Rh) source. The Doppler velocity scale was calibrated by using the Mössbauer spectrum of metallic α-Fe. The spectra were fitted by the RECOIL program [27]. The center shift value (CS) is quoted relative to the α-Fe (CS = 0).

First-principles DFT calculations of electronic structure and phonon frequencies were performed using the open-source QUANTUM-ESPRESSO package [28,29]. We employed the ultrasoft Vanderbilt-type pseudopotentials with Perdew-Burke-Ernzerhof exchange and correlation functional. For the Fe atom we considered $3s$, $3p$, $3d$, and $4s$ as valence electrons (in total 16), while the Ga valence electrons were taken to be the electrons from $3d$, $4s$, and $4p$ orbitals (in total 13). Thus, a minimum of 110 bands was needed to perform the calculations since we have four formula units per unit cell, but we nevertheless considered 128 bands, which is a very convenient number for parallelization purposes. The plane wave kinetic energy cutoff was set to 70 Ry, which proved to be sufficient for all our calculations. The ionic relaxation, self-consistent, and normal mode calculations were performed using the Monkhorst-Pack scheme, with the k mesh of $8 \times 8 \times 8$, which corresponds to 75 k points in the irreducible part of the Brillouin zone. On the other hand, the density of states (DOS) calculation requires a much larger number of k points in order to be accurate, and hence we performed the non-self-consistent calculation with a k mesh of $12 \times 12 \times 12$ in order to calculate the DOS. We used density functional perturbation theory (DFPT) [30] in order to calculate the vibrational frequencies.

III. RESULTS

We first present the band structure calculations. These results are known from the literature, but we nevertheless show them for completeness and in order to put into context the analysis of the experimental data that follow. Then we present optical, Raman, and Mössbauer spectra.

A. DFT band structure

The semiconductor $FeGa_3$ belongs to the $P4_2/mnm$ space group and it has a tetragonal P-type lattice with lattice parameters $a=6.2628(3)$ Å and $c=6.5546(5)$ Å [31]. In the DFT calculations we used the lattice parameters from the experiment and relaxed only the fractional coordinates of the atoms. These coordinates, shown in Table I, are only slightly adjusted from their measured values.

TABLE I. Nonequivalent atomic positions from the DFT calculation.

Atom	$P\bar{4}n2$	x	y	z
Fe	$4f$	0.34367	0.34367	0
Ga1	$4c$	0	0.5	0
Ga2	$8j$	0.15575	0.15575	0.26295

Figure 1 shows the dispersion relations and the density of states, calculated along the k path Z-R-A-Z-Γ-X-M-Γ in the Brillouin zone. Our results are very similar to previous work [23,32], showing that FeGa$_3$ is an indirect-gap semiconductor with the calculated band gap of 0.44 eV. The bands around the Fermi level are formed from the hybridized Fe $3d$ and Ga $4p$ orbitals.

B. Optical conductivity and infrared vibrational modes

The reflectance $R(\omega)$ measured at several temperatures between 25 and 300 K is shown in Fig. 2(a). Note that the spectra are shown on a logarithmic frequency scale so that we can distinguish both the low- and high-frequency features. The low-frequency reflectance is close to 1 which indicates a possible presence of the in-gap states that we will discuss in detail below. The far-infrared frequency region is shown on a linear scale in the inset. The peaks in $R(\omega)$ correspond to the infrared-active vibrational modes.

A better insight into the excitation spectrum can be obtained from the real part of the optical conductivity $\sigma_1(\omega)$. It corresponds to the imaginary part of the dielectric function, $\sigma_1(\omega) = \omega\epsilon_2(\omega)/4\pi$, describing the absorption of electromagnetic radiation [33,34]. Figure 2(b) shows $\sigma_1(\omega)$ obtained from the Kramers-Kronig transformation of $R(\omega)$. As this transformation involves integration of $R(\omega)$ from zero to infinity, we used extrapolation of our measurements. At high frequency ($\omega \to \infty$), the data were bridged with calculations of the dielectric function based on the x-ray photoabsorption, following the procedure described in Ref. [35]. For $\omega < 30\,\mathrm{cm}^{-1}$ we set $R(\omega) = R(30\,\mathrm{cm}^{-1})$, but we checked that $\sigma_1(\omega)$ is not sensitive to the precise form of $R(\omega)$ in the
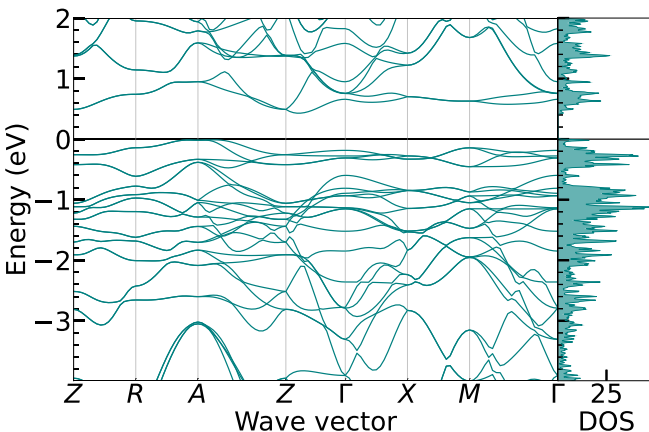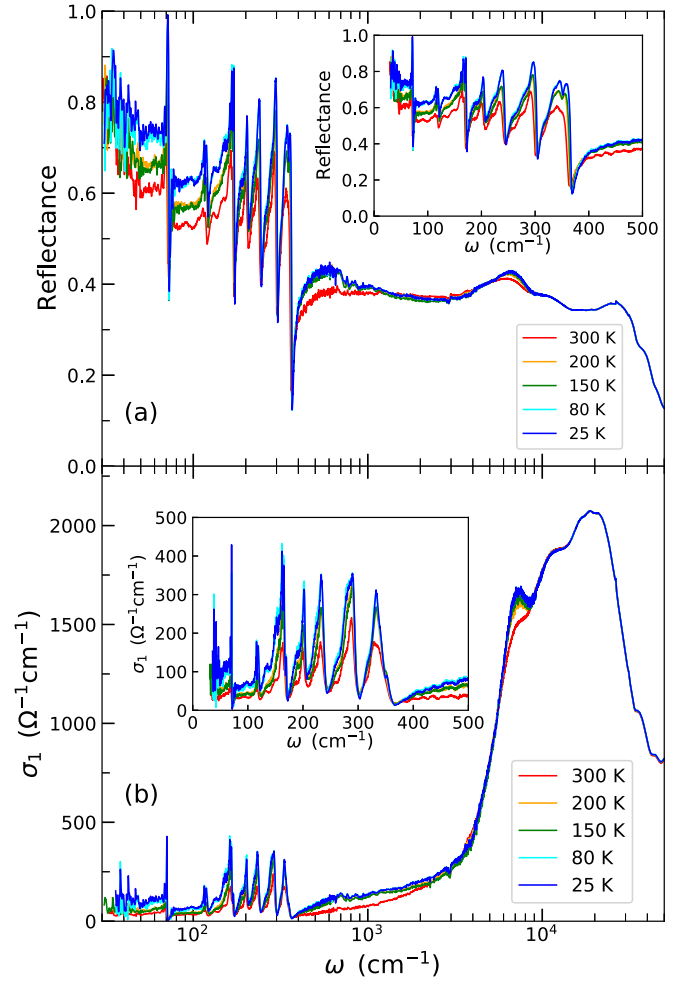

FIG. 1. DFT band structure of FeGa$_3$ and density of states in units states/(eV f.u.).

FIG. 2. Reflectance (a) and optical conductivity (b) as a function of frequency in the whole measured frequency range at several temperatures. The insets show the low-frequency data on a linear scale.

limit $\omega \to 0$. The same result is obtained using the Hagen-Rubens formula, $R(\omega) = 1 - A\sqrt{\omega}$, where A is a constant adjusted to fit the first several points from the measurements [33,34].

The optical conductivity at 25 and 300 K is shown in Fig. 3 on a linear energy (frequency) scale in units of eV. $\sigma_1(\omega)$ rapidly decreases for frequencies $\hbar\omega \lesssim 0.9\,\mathrm{eV}$ (7000 cm^{-1}). This is consistent with the DFT band structure shown in Fig. 1. It gives the smallest direct gap of 0.67 eV near the Z point in the Brillouin zone, but in many regions of the Brillouin zone the gap is between 0.7 and 0.9 eV. At $\hbar\omega = E_g \approx 0.4\,\mathrm{eV}$ the spectral weight is significantly reduced, yet it remains substantial also at $\hbar\omega < E_g$. We note that we did not attempt to calculate the optical spectra since a reliable calculation requires us to include the particle-hole interaction on a level of the Bethe-Salpeter equation, which is a very challenging task even for weakly interacting semiconductors [36,37]. A calculation of the optical spectra of FeGa$_3$ in the independent-particle approach poorly compares with our experiments [24]. On the other hand, our optical spectra for $\hbar\omega \gtrsim 0.5\,\mathrm{eV}$ are
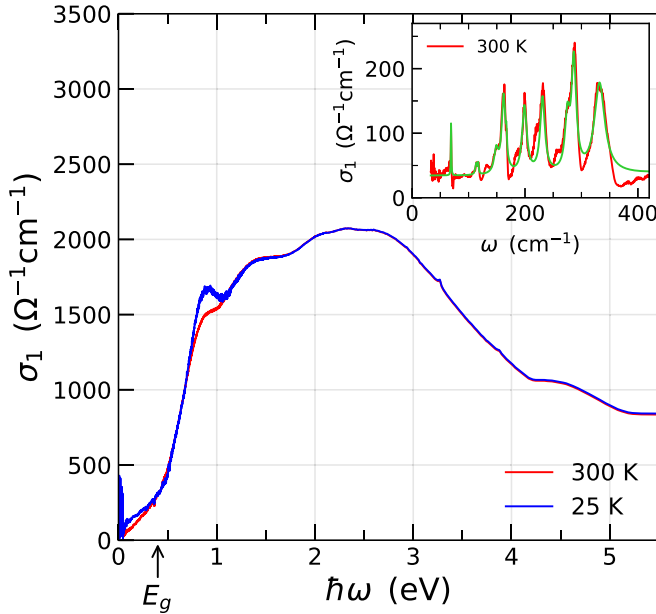
FIG. 3. Optical conductivity as a function of frequency at 25 and 300 K. The inset shows the infrared vibrational modes which are fitted by 11 Lorentzians. The green line corresponds to the cumulative fit.

TABLE II. Irreducible representation of infrared-active modes and their frequencies. The measured frequencies are obtained at 300 K. Numerical values are obtained within DFPT calculation.

Irred. rep.	Expt. (cm^{-1})	Calc. (cm^{-1})
$E_u^{1,2}$	69.00	76.08
A_{2u}^1	113.50	107.61
$E_u^{3,4}$	117.50	116.18
$E_u^{5,6}$	149.85	161.78
A_{2u}^2	162.2	162.28
$E_u^{7,8}$	166.99	168.69
$E_u^{9,10}$	199.50	201.71
$E_u^{11,12}$	231.50	229.45
$E_u^{13,14}$	275.00	281.2
A_{2u}^3	287.30	296.61
$E_u^{15,16}$	332.50	329.0

in rather good agreement with the spectra on polycrystalline samples of Ref. [26].

Evidence that the spectral weight below E_g has origins in the impurity states can be obtained from analysis of the temperature dependence of $\sigma_1(\omega)$. At finite temperatures, in a standard band gap semiconductor a small spectral weight would appear just below E_g due to the phonon assisted excitations. The same amount of the spectral weight would recover just above the band edge, where the absorption becomes slightly lower due to the finite hole (electron) concentration in the valence (conduction) band at finite temperatures [33]. On the other hand, in FeSi and FeSb$_2$ a spectral gap is closed at higher temperatures due to the strong correlation effects. In this case, transfers of the spectral weight occur over the energy range much larger than the band gap. However, in our case the spectral weight at $T = 300$ K is reduced both below and above E_g [see Figs. 2(b) and 3]. The reduction of the spectral weight below E_g should correspond to the depopulation of the impurity band, which leads to the reduction in the light absorption for subgap energies [25]. Hence, we conclude that the spectral weight below E_g is due to impurity states. We note that a small surplus of Fe atoms in comparison to the stoichiometric ratio is found in wavelength dispersive x-ray spectroscopy [23]. Our conclusion is in line with the statement that the transfer of the electrons from the impurity states to the conduction band is a likely cause of the anomalous $d\rho/dT > 0$ resistivity temperature dependence around 100 K [20,25].

We now turn our attention to the far-infrared part of the spectrum from 50 to 350 cm^{-1}, which contains infrared vibrational modes. From the inset of Fig. 2(b) it appears that most of the phonon peaks are rather broad. However, that is not the case since several peaks, in fact, consist of two vibrational modes with very close frequencies. The space group $P4_2/mnm$ has the corresponding point group $D_{4h}(4/mmm)$. Thus, all the normal modes are classified according to irreducible representations of $D_{4h}(4/mmm)$. The factor group analysis predicts 12 Raman and 11 infrared-active modes, along with ten silent and two acoustic modes:

$$\Gamma_{\text{Raman}} = 3A_{1g} + 4E_g + 2B_{1g} + 3B_{2g},$$
$$\Gamma_{\text{IR}} = 3A_{2u} + 8E_u,$$
$$\Gamma_{\text{silent}} = 2A_{2g} + 2A_{2u} + 4B_{1u} + 2B_{2u},$$
$$\Gamma_{\text{acoustic}} = A_{2u} + E_u. \quad (1)$$

The experimental data at 300 K are fitted with 11 Lorentz profile lines. Their cumulative contribution to the spectra is shown in green color in the inset of Fig. 3. A complete list of the corresponding phonon frequencies is shown in Table II. These frequencies were obtained at 300 K, but we see from the inset in Fig. 2(b) that the temperature dependence of the frequencies is weak. The changes are of the order of 1% in the temperature range between 25 and 300 K. The frequencies calculated within DFPT are in excellent agreement with measured frequencies. This implies that a crystallinity of the sample is very good, even though some surplus of Fe iron atoms is expected in comparison to the ideal composition [23]. In addition, excellent agreement between the calculated and measured frequencies indicates that the electronic correlations beyond the DFT are not strong, in line with the conclusions from DFT+U [23] and DFT+DMFT [25] calculations.

C. Raman spectra

There are 12 Raman-active modes in FeGa$_3$ [see Eq. (1)]. Wyckoff positions of the atoms, their contributions to the Γ-point phonons, and the corresponding tensors for Raman active modes are given in Table III. Since observability of the Raman-active modes in backscattering configuration of the experiment strongly depends on the orientation of the sample, we first performed orientation dependent measurements. This was done by rotating the sample in the steps of 10°. The orientation of the sample which provided the best observability

TABLE III. Contributions of each atom to the Γ-point phonons for the $P4_2/mnm$ space group and the corresponding tensors for Raman active modes.

Space group $P4_2/mnm$	
Atoms	Irreducible representations
Fe $(4f)$	$A_{1g} + A_{2g} + A_{2u} + B_{1g}$
	$+ B_{1u} + B_{2g} + E_g + 2E_u$
Ga $(4c)$	$A_{1u} + A_{2u} + B_{1u} + B_{2u} + 4E_u$
Ga $(8j)$	$2A_{1g} + A_{1u} + A_{2g} + A_{2u} + B_{1g}$
	$+ 2B_{1u} + 2B_{2g} + B_{2u} + 3E_g + 3E_u$

$$A_{1g} = \begin{pmatrix} a & 0 & 0 \\ 0 & a & 0 \\ 0 & 0 & b \end{pmatrix} \quad B_{1g} = \begin{pmatrix} c & 0 & 0 \\ 0 & -c & 0 \\ 0 & 0 & 0 \end{pmatrix} \quad B_{2g} = \begin{pmatrix} 0 & d & 0 \\ d & 0 & 0 \\ 0 & 0 & 0 \end{pmatrix}$$

$${}^1E_g = \begin{pmatrix} c & 0 & 0 \\ 0 & 0 & e \\ 0 & e & 0 \end{pmatrix} \quad {}^2E_g = \begin{pmatrix} 0 & 0 & -e \\ 0 & 0 & 0 \\ -e & 0 & 0 \end{pmatrix}$$

TABLE IV. Experimental Raman frequencies measured at 100 K and the corresponding values calculated within DFPT.

Irred. rep.	Expt. (cm^{-1})	Calc. (cm^{-1})
$E_g^{1,2}$		86.81
B_{1g}^1	127.99	125.52
$E_g^{3,4}$	138.96	139.06
A_{1g}^1	146.58	145.89
B_{2g}^1	161.67	161.51
$E_g^{5,6}$	179.01	165.09
A_{1g}^2		180.12
B_{2g}^2	238.27	239.62
$E_g^{7,8}$	264.40	258.94
B_{1g}^2	269.28	262.96
B_{2g}^3	321.43	318.53
A_{1g}^3	331.80	322.41

of Raman modes of various symmetries was used in further measurements.

Raman spectra of FeGa$_3$ single crystals, measured from the (011) plane of the sample, at temperature $T = 100$ K, for polarization angles within the range of 0° and 180° are presented in Fig. 4. We have identified 10 out of 12 Raman active modes. The assignation of modes was done in accordance with DFT calculations and polarization measurements. Peaks that exhibit the same polarization dependence were assigned with the same symmetry. Consequently, peaks at 146.58 and 331.80 cm^{-1} were assigned as A_{1g} and peaks at 127.99 and 269.98 cm^{-1} were assigned as B_{1g}. The phonon lines at 138.96, 179.01, and 264.40 cm^{-1} are assigned as E_g, whereas modes at 161.67, 238.27, and 321.43 cm^{-1} correspond to the B_{2g} symmetry modes. The full list of measured phonon

frequencies, along with their calculated values, is shown in Table IV.

There is a very good agreement between experimental and calculated phonon frequencies, with a discrepancy of less than 8%. A close match in experimental and theoretical results is not surprising knowing that the investigated material is semiconducting, with moderate electronic correlations. All of the observed phonon lines are sharp, with the full width at half maximum (FWHM) ≈ 2 cm^{-1}, and weakly temperature dependent. This indicates a good crystallinity of the sample and absence of a metal-insulator transition or magnetic ordering.
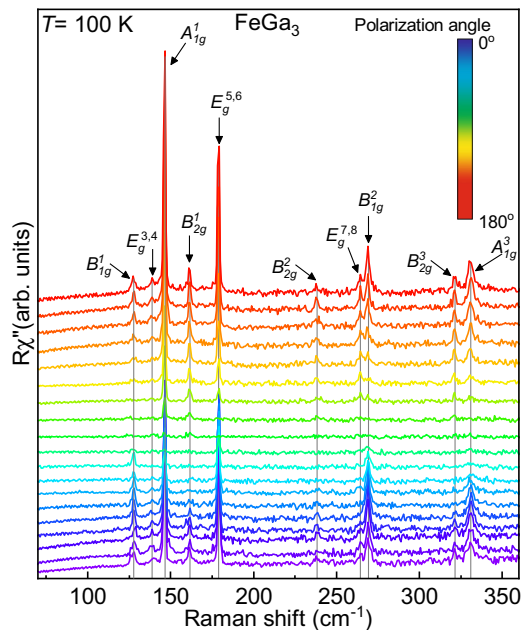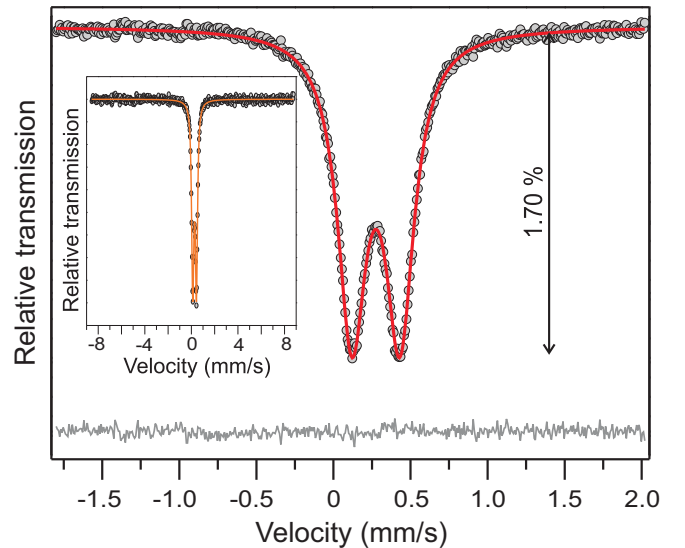

FIG. 4. Polarization-dependent Raman spectra of FeGa$_3$ single crystals. Measurements were performed with measuring step of 10° at temperature $T = 100$ K.

FIG. 5. Room temperature ^{57}Fe-Mössbauer spectra of the FeGa$_3$ sample recorded in the low-velocity range. Experimental data are presented by the solid circles and the fit is given by the red solid line. The difference (Calc. − Expt.) is shown by the dark gray line at the bottom of the figure. The vertical arrow denotes the relative position of the lowest experimental point with respect to the background (relative absorption of 1.70%). The absolute difference is less than 0.05%. The inset shows the room temperature spectrum of the FeGa$_3$ sample recorded within the high-velocity range. The orange line is just a guide for the eye.

D. Mössbauer spectra

The ^{57}Fe-Mössbauer spectroscopy was used to investigate quality and ordering of the prepared sample and to check for the presence of Fe-based impurity phases. The ^{57}Fe-Mössbauer spectra of the FeGa$_3$ are presented in Fig. 5. The spectrum recorded in the low-velocity range showed two absorption lines (doublet). In the spectrum recorded in the high-velocity range, beside the observed doublet, there is no indication of the magnetic hyperfine splitting. The thickness corrected FeGa$_3$ spectrum recorded in the low-velocity range was fitted with one Lorentzian-shaped doublet using the RECOIL program [27]. The obtained Mössbauer parameters for the measured doublet are center shift CS $= 0.28$ mm/s, quadrupole splitting $\Delta = 0.31$ mm/s, and FWHM of the Lorentzian lines is 0.22 mm/s. The obtained results closely match the hyperfine parameters for FeGa$_3$ from the literature [38–42]. A very small broadening of the resonance lines observed in the experiment is a strong indication that the sample is very well ordered and of high crystallinity.

IV. CONCLUSIONS

In summary, we have performed optical, Raman, and Mössbauer spectroscopy measurements of a narrow-gap semiconductor FeGa$_3$, along with DFT band structure and vibrational frequencies calculation. We find that the optical conductivity decreases for frequencies below $\hbar\omega \approx 0.9$ eV consistent with the direct band gap observed in DFT calculations. Our most important finding is the appearance of the optical spectral weight below the charge (indirect) gap $E_g \approx 0.4$ eV. At room temperature the spectral weight below E_g diminishes as compared to the one at $T = 25$ K. Therefore,

we conclude that this spectral weight originates from the impurities and not from the correlation effects. Interestingly, we do not find signatures of the impurities in the vibrational spectra. Both the infrared and Raman lines are very narrow, as well as the Mössbauer spectral lines, which implies a good crystallinity of the sample. The calculated vibrational frequencies are in a very good agreement with the measurements, which indicates that the electronic correlations in FeGa$_3$ are not strong, in line with previous studies.

[1] J. M. Tomczak, Thermoelectricity in correlated narrow-gap semiconductors, J. Phys.: Condens. Matter **30**, 183001 (2018).

[2] Z. Schlesinger, Z. Fisk, H.-T. Zhang, M. B. Maple, J. DiTusa, and G. Aeppli, Unconventional Charge Gap Formation in FeSi, Phys. Rev. Lett. **71**, 1748 (1993).

[3] C.-H. Park, Z.-X. Shen, A. G. Loeser, D. S. Dessau, D. G. Mandrus, A. Migliori, J. Sarrao, and Z. Fisk, Direct observation of a narrow band near the gap edge of FeSi, Phys. Rev. B **52**, R16981 (1995).

[4] C. Petrovic, J. W. Kim, S. L. Bud'ko, A. I. Goldman, P. C. Canfield, W. Choe, and G. J. Miller, Anisotropy and large magnetoresistance in the narrow-gap semiconductor FeSb$_2$, Phys. Rev. B **67**, 155205 (2003).

[5] A. Damascelli, K. Schulte, D. van der Marel, and A. A. Menovsky, Infrared spectroscopic study of phonons coupled to charge excitations in FeSi, Phys. Rev. B **55**, R4863 (1997).

[6] M. A. Chernikov, L. Degiorgi, E. Felder, S. Paschen, A. D. Bianchi, H. R. Ott, J. L. Sarrao, Z. Fisk, and D. Mandrus, Low-temperature transport, optical, magnetic and thermodynamic properties of Fe$_{1-x}$Co$_x$Si, Phys. Rev. B **56**, 1366 (1997).

[7] A. Perucchi, L. Degiorgi, R. Hu, C. Petrovic, and V. F. Mitrović, Optical investigation of the metal-insulator transition in FeSb$_2$, Eur. Phys. J. B **54**, 175 (2006).

[8] A. Herzog, M. Marutzky, J. Sichelschmidt, F. Steglich, S. Kimura, S. Johnsen, and B. B. Iversen, Strong electron

correlations in FeSb$_2$: An optical investigation and comparison with RuSb$_2$, Phys. Rev. B **82**, 245205 (2010).

[9] M. Arita, K. Shimada, Y. Takeda, M. Nakatake, H. Namatame, M. Taniguchi, H. Negishi, T. Oguchi, T. Saitoh, A. Fujimori, and T. Kanomata, Angle-resolved photoemission study of the strongly correlated semiconductor FeSi, Phys. Rev. B **77**, 205117 (2008).

[10] J. M. Tomczak, K. Haule, T. Miyake, A. Georges, and G. Kotliar, Thermopower of correlated semiconductors: Application to FeAs$_2$ and FeSb$_2$, Phys. Rev. B **82**, 085104 (2010).

[11] J. M. Tomczak, K. Haule, and G. Kotliar, Signatures of electronic correlations in iron silicide, Proc. Natl. Acad. Sci. USA **109**, 3243 (2012).

[12] V. Jaccarino, G. K. Wertheim, J. H. Wernick, L. R. Walker, and S. Arajs, Paramagnetic excited state of FeSi, Phys. Rev. **160**, 476 (1967).

[13] T. Koyama, Y. Fukui, Y. Muro, T. Nagao, H. Nakamura, and T. Kohara, Nuclear quadrupole resonance study of the electronic properties of the narrow-gap semiconductor FeSb$_2$, Phys. Rev. B **76**, 073203 (2007).

[14] A.-M. Racu, D. Menzel, J. Schoenes, and K. Doll, Crystallographic disorder and electron-phonon coupling in Fe$_{1-x}$Co$_x$Si single crystals: Raman spectroscopy study, Phys. Rev. B **76**, 115103 (2007).

[15] N. Lazarević, Z. V. Popović, R. Hu, and C. Petrovic, Evidence for electron-phonon interaction in $Fe_{1-x}M_xSb_2$ ($M =$ Co and Cr; $0 \leqslant x \leqslant 0.5$) single crystals, Phys. Rev. B **81**, 144302 (2010).

[16] N. Lazarević, M. M. Radonjić, D. Tanasković, R. Hu, C. Petrovic, and Z. V. Popović, Lattice dynamics of $FeSb_2$, J. Phys.: Condens. Matter **24**, 255402 (2012).

[17] B. C. Sales, E. C. Jones, B. C. Chakoumakos, J. A. Fernandez-Baca, H. E. Harmon, J. W. Sharp, and E. H. Volckmann, Magnetic, transport, and structural properties of $Fe_{1-x}Ir_xSi$, Phys. Rev. B **50**, 8207 (1994).

[18] P. Sun, N. Oeschler, S. Johnsen, B. B. Iversen, and F. Steglich, Huge thermoelectric power factor: $FeSb_2$ versus $FeAs_2$ and $RuSb_2$, Appl. Phys. Express **2**, 091102 (2009).

[19] C. C. Homes, Q. Du, C. Petrovic, W. H. Brito, S. Choi, and G. Kotliar, Unusual electronic and vibrational properties in the colossal thermopower material $FeSb_2$, Sci. Rep. **8**, 11692 (2018).

[20] M. Battiato, J. M. Tomczak, Z. Zhong, and K. Held, Unified Picture for the Colossal Thermopower Compound $FeSb_2$, Phys. Rev. Lett. **114**, 236603 (2015).

[21] Q. Du, L. Wu, H. Cao, C.-J. Kang, C. Nelson, G. L. Pascut, T. Besara, T. Siegrist, K. Haule, G. Kotliar, I. Zaliznyak, Y. Zhu, and C. Petrovic, Vacancy defect control of colossal thermopower in $FeSb_2$, npj Quantum Mater. **6**, 13 (2021).

[22] Y. Hadano, S. Narazu, M. A. Avila, T. Onimaru, and T. Takabatake, Thermoelectric and magnetic properties of a narrow-gap semiconductor $FeGa_3$, J. Phys. Soc. Jpn. **78**, 013702 (2009).

[23] M. Wagner-Reetz, D. Kasinathan, W. Schnelle, R. Cardoso-Gil, H. Rosner, Y. Grin, and P. Gille, Phonon-drag effect in $FeGa_3$, Phys. Rev. B **90**, 195206 (2014).

[24] Z. P. Yin and W. E. Pickett, Evidence for a spin singlet state in the intermetallic semiconductor $FeGa_3$, Phys. Rev. B **82**, 155202 (2010).

[25] M. B. Gamża, J. M. Tomczak, C. Brown, A. Puri, G. Kotliar, and M. C. Aronson, Electronic correlations in $FeGa_3$ and the effect of hole doping on its magnetic properties, Phys. Rev. B **89**, 195102 (2014).

[26] Y. V. Knyazev and Y. I. Kuz'min, The study of the structure of the electronic states of the $FeGa_3$ and $RuGa_3$ compounds by optical spectroscopy method, Phys. Solid State **59**, 2244 (2017).

[27] K. Lagarec and D. G. Rancourt, *RECOIL, Mössbauer spectral analysis software for Windows* (University of Ottawa, Ottawa, Canada, 1998).

[28] P. Giannozzi, S. Baroni, N. Bonini, M. Calandra, R. Car, C. Cavazzoni, D. Ceresoli, G. L. Chiarotti, M. Cococcioni, I. Dabo, A. D. Corso, S. de Gironcoli, S. Fabris, G. Fratesi, R. Gebauer, U. Gerstmann, C. Gougoussis, A. Kokalj, M. Lazzeri, L. Martin-Samos *et al.*, Quantum espresso: a modular and open-source software project for quantum simulations of materials, J. Phys.: Condens. Matter **21**, 395502 (2009).

[29] P. Giannozzi, O. Andreussi, T. Brumme, O. Bunau, M. B. Nardelli, M. Calandra, R. Car, C. Cavazzoni, D. Ceresoli, M. Cococcioni, N. Colonna, I. Carnimeo, A. D. Corso, S. de Gironcoli, P. Delugas, R. A. DiStasio, A. Ferretti, A. Floris, G. Fratesi, G. Fugallo *et al.*, Advanced capabilities for materials modelling with quantum espresso, J. Phys.: Condens. Matter **29**, 465901 (2017).

[30] S. Baroni, S. de Gironcoli, A. Dal Corso, and P. Giannozzi, Phonons and related crystal properties from density-functional perturbation theory, Rev. Mod. Phys. **73**, 515 (2001).

[31] U. Häussermann, M. Boström, P. Viklund, O. Rapp, and T. Björnängen, $FeGa_3$ and $RuGa_3$: Semiconducting Intermetallic Compounds, J. Solid State Chem. **165**, 94 (2002).

[32] Y. Imai and A. Watanabe, Electronic structures of semiconducting $FeGa_3$, $RuGa_3$, $OsGa_3$, and $RuIn_3$ with the $CoGa_3$- or the $FeGa_3$-type structure, Intermetallics **14**, 722 (2006).

[33] F. Wooten, *Optical Properties of Solids* (Academic Press, New York, 1972).

[34] D. B. Tanner, *Optical Effects in Solids* (Cambridge University Press, New York, 2019).

[35] D. B. Tanner, Use of x-ray scattering functions in Kramers-Kronig analysis of reflectance, Phys. Rev. B **91**, 035123 (2015).

[36] S. Albrecht, L. Reining, R. Del Sole, and G. Onida, *Ab Initio* Calculation of Excitonic Effects in the Optical Spectra of Semiconductors, Phys. Rev. Lett. **80**, 4510 (1998).

[37] M. Rohlfing and S. G. Louie, Electron-hole excitations and optical spectra from first principles, Phys. Rev. B **62**, 4927 (2000).

[38] G. L. Whittle, P. E. Clark, and R. Cywinski, Vacancies and site occupation in Co-Ga-Fe alloys (Mössbauer study), J. Phys. F **10**, 2093 (1980).

[39] I. Dézsi, I. Szücs, C. Fetzer, and W. Keune, The local interactions of Co and Fe in β-phase $Co_x Ga_{(1-x)}$, Acta Mater. **46**, 3299 (1998).

[40] N. Tsujii, H. Yamaoka, M. Matsunami, R. Eguchi, Y. Ishida, Y. Senba, H. Ohashi, S. Shin, T. Furubayashi, H. Abe, and H. Kitazawa, Observation of energy gap in $FeGa_3$, J. Phys. Soc. Jpn. **77**, 024705 (2008).

[41] G. R. Hearne, S. Bhattacharjee, B. P. Doyle, M. A. M. Ahmed, P. Musyimi, E. Carleschi, and B. Joseph, Pressure-induced disruption of the local environment of Fe-Fe dimers in $FeGa_3$ accompanied by metallization, Phys. Rev. B **98**, 020101(R) (2018).

[42] D. Mondal, C. Kamal, S. Banik, A. Bhakar, A. Kak, G. Das, R. V. R., A. Chakrabarti, and T. Ganguli, Structural and electronic properties of $Fe(Al_x Ga_{1-x})_3$ system, J. Appl. Phys. **120**, 165102 (2016).

Correction: A typographical error in the fourth affiliation was introduced during the production cycle and has been fixed.

BPU11 CONGRESS

28 August 2022 - 1 September 2022

Book of Abstracts

Editors: Antun Balaž, Goran Djordjević,
Jugoslav Karamarković, Nenad Lazarević

Co-organizers

- Serbian Academy of Sciences and Arts (SASA)

- Faculty of Sciences and Mathematics, University of Niš

- Faculty of Physics, University of Belgrade

- Vinča Institute of Nuclear Sciences, University of Belgrade, National Institute of the Republic of Serbia

- Faculty of Mathematics, University of Belgrade

- Mathematical Institute of Serbian Academy of Sciences and Arts, National Institute of the Republic of Serbia

- Faculty of Science, University of Kragujevac

- Faculty of Sciences, University of Novi Sad

- Faculty of Sciences and Mathematics, University of Pristina in Kosovska Mitrovica

- SEENET-MTP Centre

- European Physical Society (EPS)

- Institute of Physics Belgrade, National Institute of the Republic of Serbia

Partners and Sponsors

- International Centre for Theoretical Physics (ICTP), Trieste

- Central European Initiative (CEI), Trieste

- Ministry of Education, Science, and Technological Development, Republic of Serbia

- Conseil Européen pour la Recherche Nucléaire (CERN), Geneva

- Provincial Secretariat for Higher Education and Scientific Research, Autonomous Province of Vojvodina, Republic of Serbia

- The European Physical Journal (EPJ)

The coupling of Frenkel excitons (FEs) and intramolecular vibrations in an organic layer as a part of microcavity has been studied in the paper. Two cases are treated: a) uniaxial layer of point group 4 (optical axis is supposed perpendicular to the layer); b) monoclinic anthracene-like layer with monoclinic axis b perpendicular to the layer. The exciton-phonon coupling produces the vibronic wings with complex spectra which can contain bound exciton-phonon states and many-particle (unbound) bands. Consequently in those regions the absorption lines and the resonance members in dielectric tensor appear. We treat theoretically their effects on the polaritons in the microcavity and illustrate using numerical calculations the peculiarities of the polaritonic spectra in the vibronic wings of Frenkel excitons.

S06-CMPSP-111 / **Oral presentation**

Spectral functions of the Holstein polaron: exact and approximate solutions

Authors: Petar Mitrić[1]; Veljko Janković[1]; Nenad Vukmirović[1]; Darko Tanasković[1]

[1] *Institute of Physics Belgrade, University of Belgrade*

Presenter: P. Mitrić (mitricp@ipb.ac.rs)

It is generally accepted that the dynamical mean field theory (DMFT) gives a good solution of the Holstein model [1], but only in dimensions greater than two. Here we show that the DMFT, which becomes exact in the weak coupling and in the atomic limit, provides an excellent numerically cheap approximate solution for the spectral function of the Holstein model in the whole range of parameters even in one dimension. To establish this, we made a detailed comparison with the spectral functions that we obtained using newly developed momentum-space numerically exact hierarchical equations of motion method, which yields electronic correlation functions directly in real time [2]. We crosschecked these conclusions with our path integral quantum Monte Carlo and exact diagonalization results, as well as with the available numerically exact results from the literature [3].

References:
1. S. Ciuchi, F. de Pasquale, S. Fratini, and D. Feinberg, Phys. Rev. B **56**, 4494 (1997).
2. V. Janković and N. Vukmirović, Phys. Rev. B **105**, 054311 (2022).
3. D. Jansen, J. Bonča, and F. Heidrich-Meisner, Phys. Rev. B **102**, 165155 (2020).

SCMP

26 – 30 June 2023
Belgrade, Serbia

21. СИМПОЗИЈУМ ФИЗИКЕ КОНДЕНЗОВАНЕ МАТЕРИЈЕ

THE 21st SYMPOSIUM ON CONDENSED MATTER PHYSICS

BOOK OF ABSTRACTS

Conference Chairs

Vladimir Dobrosavljević, *Florida State University, USA*

Zorica Konstantinović, *Institute of Physics Belgrade*

Željko Šljivančanin, *Vinča Institute of Nuclear Sciences*

Organizing Committee

Jelena Pešić, *Institute of Physics Belgrade-* chair

Andrijana Šolajić, *Institute of Physics Belgrade*

Ivana Milošević, *Institute of Physics Belgrade*

Tijana Tomašević-Ilić, *Institute of Physics Belgrade*

Jelena Mitrić, *Institute of Physics Belgrade*

Bojana Višić, *Institute of Physics Belgrade*

Jovan Blagojević, *Institute of Physics Belgrade*

Marko Orozović, *Vinča Institute of Nuclear Sciences*

Mitra Stepić, *Vinča Institute of Nuclear Sciences*

Igor Popov, *Institute for Multidisciplinary Research, Belgrade*

Program Committee

Ivan Božović, *Brookhaven National Laboratory, USA*

Vladimir Dobrosavljević, *Florida State University, USA*

Milan Damnjanović, *Faculty of Physics, University of Belgrade, Serbia*

Vladimir Djoković, *Vinča Institute*, *University of Belgrade, Serbia*

Gyula Eres, *Oak Ridge National Laboratory, USA*

Laszló Forró, *University of Notre Dame, USA*

Radoš Gajić, *Institute of Physics Belgrade*

Igor Herbut, *Simon Fraser University, Canada*

Zoran Ikonić, *University of Leeds, UK*

Nenad Lazarević, *Institute of Physics Belgrade*

Ivanka Milošević, *Faculty of Physics, University of Belgrade, Serbia*

Milorad Milošević, *University of Antwerp, Belgium*

Milica Milovanović, *Institute of Physics Belgrade*

Stevan Nadj-Perge, *CALTECH, USA*

Branislav Nikolić, *University of Delaware, USA*

Cedomir Petrovic, *Brookhaven National Laboratory, USA*

Dragana Popović, *National High Magnetic Field Laboratory, USA*

Zoran V. Popović, *Institute of Physics Belgrade*

Zoran Radović, *Faculty of Physics, University of Belgrade, Serbia*

Miljko Satarić, *Faculty of Technical Sciences, University of Novi Sad, Serbia*

Marko Spasenović, *Institute of Chemistry, Technology and Metallurgy, Belgrade, Serbia*

Djordje Spasojević, *Faculty of Physics, University of Belgrade, Serbia*

Željko Šljivančanin, *Vinča Institute of Nuclear Sciences*

Bosiljka Tadić, *Jožef Štefan Institute, Slovenia*

Milan Tadić, *School of Electrical Engineering, University of Belgrade, Serbia*

Darko Tanasković, *Institute of Physics Belgrade*

Jasmina Tekić, *Vinča Institute of Nuclear Sciences*

21. СИМПОЗИЈУМ ФИЗИКЕ КОНДЕНЗОВАНЕ МАТЕРИЈЕ

THE 21st SYMPOSIUM ON CONDENSED MATTER PHYSICS

26 - 30 June 2023, Belgrade, Serbia

https://www.sfkm2023.ipb.ac.rs/

Institute of Physics Belgrade

Vinca Institute of Nuclear Sciences

University of Belgrade, Faculty of Physics

Serbian Academy of Sciences and Arts

Ministry of Science, Technological Development and Innovation

Cumulant Expansion in the Holstein model: Spectral Functions and Mobility

Petar Mitrić[a], Veljko Janković[a], Nenad Vukmirović[a] and Darko Tanasković[a]

[a]Institute of Physics Belgrade, University of Belgrade, Pregrevica 118, 11080 Belgrade, Serbia

Abstract. The cumulant expansion (CE) method presents an alternative to the usual Dyson equation approach for the calculation of spectral functions and quasiparticle properties of interacting quantum many-particle systems. We examine the range of validity of this method by implementing it in a system described by the simplest electron-phonon model Hamiltonian - the Holstein model [1]. For a benchmark, we use the dynamical mean-field theory (DMFT) [2] which gives, as we have recently shown [3], rather accurate spectral functions in the whole parameter space. The results are also compared to the one-shot and the self-consistent Migdal approximation. While CE is exact in both the weak-coupling and the atomic limit, we find that even in a regime of intermediate coupling in 1D, the CE resolves well both the quasiparticle and the first satellite peak of the spectral function. CE also gives promising results for high temperatures, but it is not exact in the limit $T \to \infty$, which is proved analytically by analyzing the spectral sum rules.

Charge mobility μ is also calculated, using the bubble approximation of the Kubo formalism. At high temperatures, we demonstrate that it assumes a power law, which is different in the limit of weak coupling $\mu \propto T^{-2}$, and in the case of somewhat stronger coupling $\mu \propto T^{-3/2}$.

REFERENCES

1. Mitrić, P., Janković, V., Vukmirović, N., and Tanasković D., *Phys. Rev. B* **107**, 125165 (2023).
2. Ciuchi, S., de Pasquale, F., Fratini, S., and Feinberg, D., *Phys. Rev. B* **56**, 4494 (1997).
3. Mitrić, P., Janković, V., Vukmirović, N., and Tanasković D., *Phys. Rev. Lett.* **129**, 096401 (2022).

INSTITUTE OF TECHNICAL SCIENCES OF SASA
MATERIALS RESEARCH SOCIETY OF SERBIA

Programme and the Book of Abstracts

TWENTIETH YOUNG RESEARCHERS' CONFERENCE MATERIALS SCIENCE AND ENGINEERING

Belgrade, November 30 – December 2, 2022

TWENTIETH YOUNG RESEARCHERS' CONFERENCE
MATERIALS SCIENCE AND ENGINEERING

November 30 – December 2, 2022, Belgrade, Serbia

Programme and the Book of Abstracts

Materials Research Society of Serbia
&
Institute of Technical Sciences of SASA

2022

Aim of the Conference

Main aim of the conference is to enable young researchers (post-graduate, master or doctoral student, or a PhD holder younger than 35) working in the field of materials science and engineering, to meet their colleagues and exchange experiences about their research.

Topics

Biomaterials
Environmental science
Materials for high-technology applications
Materials for new generation solar cells
Nanostructured materials
New synthesis and processing methods
Theoretical modelling of materials

Scientific and Organizing Committee

Committee President
Smilja Marković   Institute of Technical Sciences of SASA, Belgrade, Serbia

Vice-presidents
Dragana Jugović   Institute of Technical Sciences of SASA, Belgrade, Serbia
Magdalena Stevanović   Institute of Technical Sciences of SASA, Belgrade, Serbia
Đorđe Veljović   Faculty of Technology and Metallurgy, Belgrade, Serbia

Members
Tatiana Demina   Enikolopov Institute of Synthetic Polymeric Materials, Russian Academy of Sciences
Jasmina Dostanić   Institute of Chemistry, Technology and Metallurgy, Belgrade, Serbia
Xuesen Du   Chongqing University, Chongqing, China
Branka Hadžić   Institute of Physics, Belgrade, Serbia
Ivana Jevremović   Norwegian University of Science and Technology, Trondheim, Norway
Sonja Jovanović   Institute of Nuclear Sciences "Vinča", Belgrade, Serbia
Snežana Lazić   Universidad Autónoma de Madrid, Spain
Lidija Mančić   Institute of Technical Sciences of SASA, Belgrade, Serbia
Marija Milanović   Faculty of Technology, Novi Sad, Serbia
Miloš Milović   Institute of Technical Sciences of SASA, Belgrade, Serbia
Nebojša Mitrović   Faculty of Technical Sciences, Čačak, Serbia
Irena Nikolić   Faculty of Metallurgy and Technology, Podgorica, Montenegro
Marko Opačić   Institute of Physics, Belgrade, Serbia
Vuk Radmilović   Faculty of Technology and Metallurgy, Belgrade, Serbia
Tatjana D. Savić   Institute of Nuclear Sciences "Vinča", Belgrade, Serbia
Ana Stanković   Institute of Technical Sciences of SASA, Belgrade, Serbia
Srečo Škapin   Institute Jožef Stefan, Ljubljana, Slovenia
Boban Stojanović   Faculty of Sciences, Kragujevac, Serbia

Ivana Stojković-Simatović   Faculty of Physical Chemistry, Belgrade, Serbia
Konrad Terpiłowski   Department of Interfacial Phenomena, Institute of Chemical
   Sciences, Faculty of Chemistry, Maria Curie-Skłodowska
   University in Lublin, Poland
Vuk Uskoković   TardigradeNano, Irvine, CA, USA
Rastko Vasilić   Faculty of Physics, Belgrade, Serbia
Ljiljana Veselinović   Institute of Technical Sciences of SASA, Belgrade, Serbia
Siniša Vučenović   Faculty of Sciences, Department of Physics, Banja Luka, B&H
Marija Vukomanović   Institute Jožef Stefan, Ljubljana, Slovenia

Conference Secretary
Ivana Dinić   Institute of Technical Sciences of SASA, Belgrade, Serbia

Conference Technical Committee

Aleksandra Stojičić, Marina Vuković, Željko Mravik, Katarina Aleksić, Jelena Rmuš

Results of the Conference

Beside printed «Programme and the Book of Abstracts», which is disseminated to all conference participants, selected and awarded peer-reviewed papers will be published in journal "Tehnika – Novi Materijali". The best presented papers, suggested by Session Chairpersons and selected by Awards Committee, will be proclaimed at the Closing Ceremony. Part of the award is free-of-charge conference fee at YUCOMAT 2023.

Sponsors

Acknowledgement

9-7

Infrared and Raman study of narrow-gap semiconductor FeGa₃

C. Martin[1], V. A. Martinez[2], M. Opačić[3], S. Djurdjić-Mijin[3], P. Mitrić[3], A. Umićević[4], V. N. Ivanovski[4], A. Poudel[1], I. Sydoryk[1], Weijun Ren[5], R. M. Martin[6], D. B. Tanner[2], N. Lazarević[3], C. Petrovic[5], and D. Tanasković[3]

[1]Ramapo College of New Jersey, Mahvah, NJ 07430, USA, [2]Department of Physics, University of Florida, Gainesville, Florida 32611, USA, [3]Institute of Physics Belgrade, University of Belgrade, Pregrevica 118, 11080 Belgrade, Serbia, [4]Vinca Institute of Nuclear Sciences – National Institute of the Republic of Serbia, University of Belgrade, Belgrade, Serbia, [5]Brookhaven National Laboratory, NY 11973, USA, [6]Montclair State University, Montclair, NJ 07043, USA

Narrow-gap semiconductors have been intensively studied in the last few years due to their huge thermoelectric power at low temperatures and possible impact of strong electronic correlations on their physical properties. Here, we analyse infrared and Raman spectra of $FeGa_3$ single crystal. The optical conductivity obtained from reflectance measurements suggests an indirect energy gap of around 0.4 eV, although the existence of substantial spectral weight at low energies prevents its precise determination. The energies of Raman and infrared active modes obtained by our DFT calculations agree very well with the experimental results. Temperature dependence of Raman mode energies and linewidths is weak between 80 and 300 K, indicating the absence of any phase transition. Most of the vibrational modes are very narrow due to weak electron-phonon and/or spin-phonon interactions, and good crystallinity of the single crystal, which is also confirmed by the Mössbauer spectra.
.